Physik-Department E12 der Technischen Universität München

Development of a Radioactive ^{17}F Beam and its use in Nuclear Astrophysics Experiments

Boris Peter Mathias Sascha Harss

Vollständiger Abdruck der von der Fakultät für Physik der
Technischen Universität München zur Erlangung des akademischen Grades
eines

Doktors der Naturwissenschaften (Dr. rer. nat.)

genehmigten Dissertation.

Vorsitzender:		Univ.- Prof. Dr. Peter Ring
Prüfer der Dissertation:		
	1.	Univ.- Prof. Dr. Hans-Joachim Körner
	2.	Univ.- Prof. Dr. Eckehart Nolte

Die Dissertation wurde am 25. Juni 2001 bei der Technischen Universität München eingereicht und durch die Fakultät für Physik am 11. Juli 2001 angenommen.

CONTENTS

1 INTRODUCTION 1

2 NUCLEOSYNTHESIS AND NUCLEAR ASTROPHYSICS 3

2.1 Breakout form the HCNO Cycle 5

2.2 S-factor and Gamow Window 6

3 THE NUCLEAR PHYSICS OF $^{17}F(P,a)^{14}O$ 9

3.1 Direct Reaction Mechanism 10

3.2 Resonant Reaction Mechanism 11

3.2.1 Alpha Angular Distributions 13

3.2.2 R-Matrix Calculations 14

3.2.3 Determining the Resonance Width from Finite Target Thickness Data 16

4 BASIC CONSIDERATIONS FOR THE EXPERIMENT 19

4.1 The $^{14}O(\alpha,p)$ Reaction at $T_9 = 0.5 – 2$ 19

4.2 Time-Inverse Reaction 20

5 PRODUCTION OF A ^{17}F BEAM USING THE IN-FLIGHT TECHNIQUE 23

5.1 Basic Considerations of the In-Flight Production Technique 23

5.1.1 The Source Distribution S at the Target 24

5.1.2 Transport Considerations 27

5.1.3 Typical Requirements for Production Reactions and Production Targets 29

5.2 The Primary Gas Target 30

5.2.1 Cooling System 31

5.2.2 The Gas Handling- and Regulation System 32

5.2.3 Windows 33

5.2.4 Gas Cell Assembly and Support System 35

5.3 Production Setups at ATLAS 36

5.3.1 Initial Configuration 36

5.3.2 Improved Configuration 37

5.3.3 Tuning 38

5.4 Other Beams 39

6 EXPERIMENTS WITH ^{17}F BEAMS 41

6.1 Fusion-Fission Experiment 41

6.2 Ludwig II 43

6.3 Super Ludwig 44
6.3.1 The Bragg-Counter and PPAC 45
6.3.2 The TOF-RF Information. 47
6.3.3 The Si-Array 48
6.3.4 Energy versus Energy 49
6.4 Universal 3D-Montecarlo Package 50

7 DATA AND RESULTS 53

7.1 Data from the August 1998 Experiment 53
7.2 Data from the November 1999 Setup 55
7.3 Assignment of States in ^{18}Ne 59
7.4 Astrophysical Reaction Rates 65
7.5 What is left to do? 67

8 APPENDIX 69

8.1 Thanks 69
8.2 Documentation for the Monte Carlo Package 71
8.3 The Program GAMMAW 88

9 REFERENCES 89

Summary

The stellar production of nuclei heavier than oxygen takes place at high temperatures which occur in massive stars and violent explosive events. While the bulk of the nucleosynthesis of the heavy elements is believed to proceed through neutron capture reactions in the so-called s and r processes, there is strong evidence of proton-capture reactions contributing considerably for nuclei up to Tellurium. To understand, how the so-called rapid-proton capture process evolves from the CNO cycle, a quantitative knowledge of reactions like $^{14}O(\alpha,p)^{17}F$ is essential.

The $^{14}O(\alpha,p)^{17}F$ reaction is largely controlled by the properties of unbound states in the compound nucleus ^{18}Ne. While a direct measurement of the $^{14}O(\alpha,p)^{17}F$ reaction at the relevant energies appears difficult, the time-inverse $^{17}F(p,\alpha)^{14}O$ reaction (Q = 1.19 MeV) is experimentally better accessible. In inverse kinematics, i.e. using a ^{17}F beam bombarding a hydrogen target, reasonably high ^{17}F beam energies can be used to study astrophysically relevant resonances in ^{18}Ne. In a measurement of the $^{17}F(p,\alpha)^{14}O$ reaction, however, only the ground-state to ground-state contribution of the astrophysical $^{14}O(\alpha,p)^{17}F$ reaction rate can be determined. The influence of the transition to the excited state ($^{14}O(\alpha,p')^{17}F^{495}$) requires a measurement of elastic and inelastic proton scattering on ^{17}F.

Within this thesis, we have developed a technique to study the $^{14}O(\alpha,p)^{17}F$ and similar reactions, starting from the production of a radioactive beam using the in-flight technique to the design of a highly efficient detector system.

For the first time, a ^{17}F beam ($T_{1/2}$ = 65 s) was produced in the laboratory using the in-flight technique. The ^{17}F ions were generated via the $d(^{16}O,^{17}F)n$ reaction by bombarding a nitrogen-cooled deuterium gas cell with an intense ^{16}O beam. The secondary ^{17}F ions were separated from the primary ^{16}O beam with a bending magnet and the transport efficiency was maximized by refocusing the produced ^{17}F ions in angle and energy with a superconducting solenoid and a pair of superconducting RF-resonators. The setup provided ^{17}F beams with intensities up to $2\cdot10^6$ ^{17}F/s and an energy resolution of ~500 keV, corresponding to 28 keV in the ^{17}F + p center-of-mass frame.

We have designed and assembled a new detector setup for the simultaneous measurement of the $^{17}F(p,\alpha)^{14}O$, $^{17}F(p,p)^{17}F$ and $^{17}F(p,p')^{17}F^{495}$ reactions. It consisted of a highly segmented silicon detector array, detecting the light reaction products (p and α) and an annular Bragg-type ion chamber/PPAC combination for the detection of the heavy particles (^{17}F,^{14}O). The system provides a detection efficiency of typically 60% for the $^{17}F(p,\alpha)^{14}O$ reaction. The generated data were analyzed using a custom-developed 3D-Monte Carlo simulation package.

Using this setup, we were able to measure directly astrophysically relevant total and partial widths of particle unbound states in ^{18}Ne. The results show that, contrary to previous assumptions, the state at E_x = 7.35 MeV in ^{18}Ne plays only a minor role in the stellar production of ^{17}F at all temperatures. From the measured widths of G_p and $G_{p'}$ we conclude that the first and only excited state (495.3 keV, $1/2^+$) in ^{17}F does not play a significant role for the $^{14}O(\alpha,p)^{17}F$ reaction rate.

With the presented approach, we were able to demonstrate that measurements with radioactive beams produced in the in flight technique can provide valuable data for both nuclear physics and astrophysical questions.

1 Introduction

Since Hans Bethes groundbreaking work[1] in 1938, the fields of nuclear physics and astrophysics have been deeply intertwined: Nuclear Reactions were identified to be the source of energy of the stars, and the CNO cycle propose. In the past 60 years, complicated networks of nuclear reactions were identified as the underlying mechanism of nucleosynthesis, taking place in a variety of different classes of cosmological objects. Today, nuclear astrophysics provides a largely consistent picture of the processes taking place in stars of different masses in all stages of their existence[2]. Many nuclear physics measurements had to be carried out to provide the necessary input parameters. These measurements, while technically challenging, could be performed with existing equipment at nuclear physics laboratories using standard nuclear physics techniques.

About half of the chemical elements heavier than oxygen originate from explosive nucleosynthesis. The term stands for all violent processes that take place at the end of the life of a star. Here, half-lives of specific isotopes with respect to reactions are as short as milliseconds, thus these reactions proceed much faster than most beta-decays. As a consequence, participants of important reactions are known[3] to be isotopes outside the valley of beta stability. To investigate these processes in a laboratory, radioactive ion beams or radioactive targets are required. They are the key tool to a detailed understanding of the reaction networks in objects like novae, supernovae, Wolf-Rayet-stars, red giants or X-ray bursts. This is one of the major motivations for building new, universal radioactive beam facilities. They will provide a large variety of exotic ion beams for experimental stations that combine large detection efficiency and good background suppression.

While proposals are written and planning committees meet, the community of nuclear astrophysicists already performs experiments with the limited beams provided at a few existing first generation facilities. Another approach is to use novel setups at stable beam facilities to generate radioactive beams for use in a specific type of experiment. This thesis reports on the effort of a group at Argonne National Laboratory to develop light, proton-rich heavy ion beams at the ATLAS[4] linear accelerator. Our main focus was on the production of a ^{17}F beam, the development of a high-efficiency detection scheme and the study of the $^{14}O(\alpha,p)^{17}F$ reaction via the time-reversed process, $^{17}F(p,\alpha)^{14}O$.

2 Nucleosynthesis and Nuclear Astrophysics

Nucleosynthesis is the term used for the sum of all the processes that transform nuclei in the cosmos from one species to another. A thorough understanding of these processes is the key to the interpretation of the abundances of the isotopes in the universe. The main sites of nucleosynthesis are stars. Nuclear reactions occur mostly in their cores, but in some instances also on their surface and even in their close vicinity.

Depending on the initial nuclear abundances and mechanical properties like mass and angular momentum, a cosmic object stabilizes at a certain density, temperature and mode of energy generation. The energy generation itself depends on the cross-sections of nuclear reactions, the density of the reaction partners and their energy distribution, i.e. their temperature. In many instances, a stable state of nuclear burning results with minimal change over time. Stars in the main sequence are a typical example. However, the initial parameters of the system change over time, either because the burning process itself or because of external influences like mass-flow from or to another star in a binary system. As a result, a change in character of the object occurs. Either another semi-stable burning phase starts or a catastrophic event like a nova or supernova explosion is triggered.

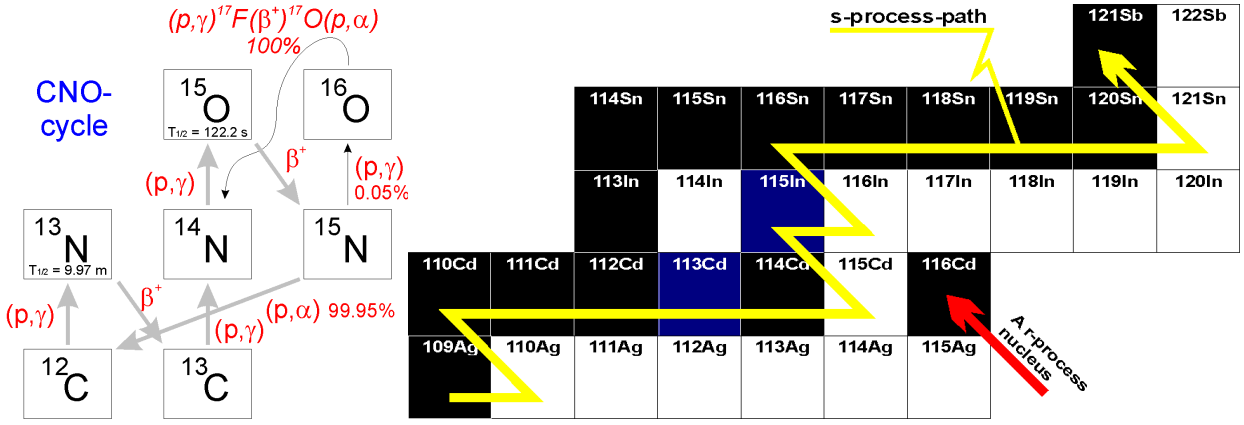

Fig. 2.1 The CNO-Cycles and the s-process both involve reactions on stable or very long lived reaction partners. The reaction rate is limiting the speed of the process.

The theoretical treatment of steady-state burning of stars is non-trivial because of the complex issues of fluid dynamics within the rotating plasma with its magnetic fields. However, the number of nuclear reactions of importance is limited and involves essentially only stable isotopes. All β-unstable reaction products decay back to a stable isotope before the next reaction step occurs. An example is the CNO-cycle (Fig. 2.1, left), the major source of energy in massive main sequence stars. In a catalytic process, it fuses four protons via three proton captures, two β^+-decays and one (p,α) reaction to a ^{4}He nucleus. Another example is the s-process (Fig. 2.1, right). At temperatures of no more than T_9* = 0.1, nucleosynthesis of heavy elements occurs only via this slow neutron capture mechanism. The s-process is expected to take place in AGB stars (Asymptotic Red Giants), in which neutrons from (α,n)-reactions are captured until a beta-unstable nucleus is reached. Then, a β^--decay takes place. Thus, in a slow accumulation of nucleons, the s-process walks up along stable nuclei on the neutron-rich side of the valley of stability.

* T_9 denotes temperature in units of 10^9 K. This notation is widely used in nuclear astrophysics.

The r-process is the rapid analogue to the s-process, which involves a dense neutron-bath as assumed for a certain phase of Type II supernova explosions. In an equilibrium between neutron capture, photo-disintegration and β^--decay, nuclei far from stability are produced. After the hot phase of the supernova-event is over, the very neutron-rich nuclei produced decay back towards the valley of stability. It is assumed to be responsible for the production of neutron-rich isotopes located on the right side of the s-process path (e.g. ^{116}Cd, see Fig. 2.1). It is known[5] since the 1950s, that combined s- and r-process calculations reproduce the observed distribution of isotopes fairly well, but fail to explain the large abundance of a certain isotopes (e.g. ^{58}Ni) on the left side of stability.

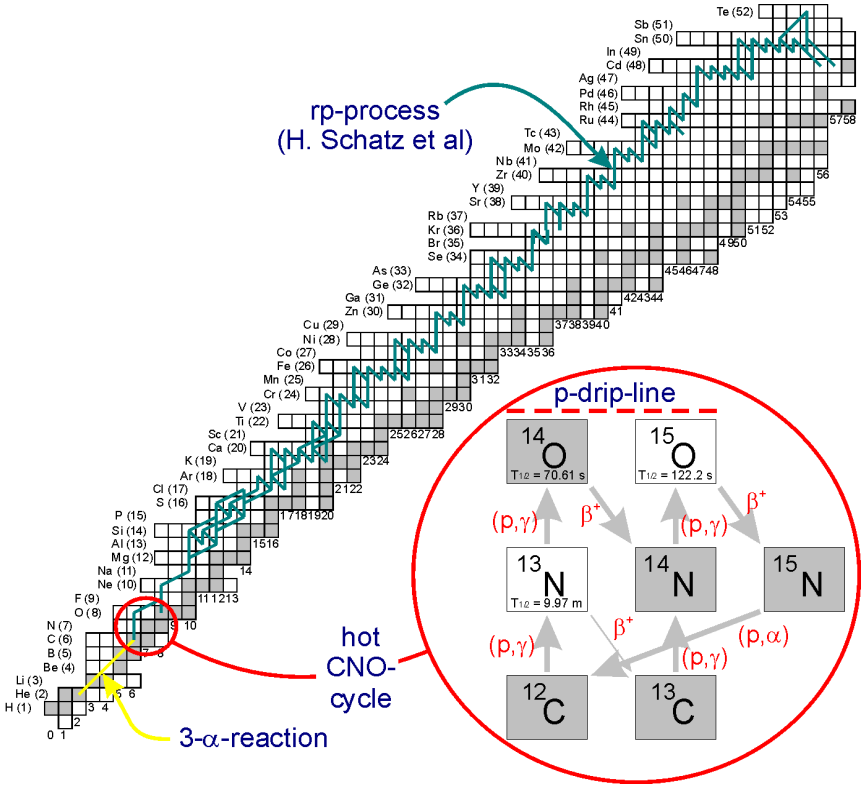

Fig. 2.2 The HCNO-Cycle and the rp-process consist of fast proton capture reactions until these reactions do not lead to a particle-stable product any more or the beta-decay is fast enough to compete with the proton capture. Here, a b-decay or a reaction with an a-particle has to be waited for. Without an alpha-induced reaction, there is no way out of the HCNO-cycle since a proton capture on ^{15}N leads to an (p,a)-reaction and ^{15,16}F are not bound.

In the case of very hot and dense systems, capture-reactions of charged particles may process nuclei on shorter time scales than their β-decay half-life. Especially (p,γ)-reactions, due to their relatively low Coulomb-barrier, can reach very fast reaction rates in such environments. The rapid proton capture (rp) process contributes to the nucleosynthesis by forming nuclei on the proton-rich side of the nuclide chart by a sequence of proton captures and β^+-decays along the *N*=*Z*-line. As shown in Fig. 2.2, nuclei are transformed quickly starting from the Ne-region into heavier isotopes while large amounts of energy are released[6]. The details of the pathway are temperature-dependent. Shown here is a high-temperature X-ray-burst scenario that leads up all the way into the Sn-region and strongly favors (α,p)-reactions over β^+-decays for lower-Z nuclei. Since, independent of the temperature, no more proton captures are possible at the proton drip-line, the process is largely controlled by the β-half-lives and the cross-sections of competing processes at these waiting-point nuclei.

While there are many detailed questions left, the existence and basic structure of the rp-process are well established. However, one of the unsettled questions is concerned with its onset, starting from a CNO-hydrogen burning system. At sufficiently large temperatures in the range of $0.2 < T_9 < 0.5$, the CNO-cycle described above changes its structure slightly, now being called hot CNO cycle (HCNO-cycle). The ^{13}N-β^+ decay ($T_{1/2}$ = 598s) is bypassed by the ^{13}N(p,γ)^{14}O reaction. Under such conditions, the limiting factor of the cycle is the β^+ decay of ^{14}O ($T_{1/2}$ = 70.6s) and ^{15}O ($T_{1/2}$ = 122.2s). The capture of another proton on the two oxygen isotopes is, independently of the temperature, impossible, since ^{15}F and ^{16}F are particle unbound. Therefore the hot CNO-cycle is also called β-limited CNO cycle. Like the standard CNO-cycle, it catalytically fuses four protons to one ^{4}He nucleus in one turn. With proton capture reactions alone, the carbon, nitrogen and oxygen nuclei cannot leave the circle. To feed the rp-process and bridge the gap between ^{14}O or ^{15}O to ^{19}Ne, at least one intermediate reaction involving an α-particle is required.

2.1 Breakout form the HCNO Cycle

Since the half-lives of nuclei involved in the rp-process are short ($T_{1/2,\beta+}$ < 1 s) compared to the half lives in the hot CNO cycle ($T_{1/2,\beta+}$ > 1min), its potential energy generation is far greater. Thus, the system quickly heats up even more as soon as the break-out into the rp-process is possible and additional channels open up, allowing additional mass flow from CNO-isotopes into the rp-process. For the initial breakout from the CNO-cycle, two reaction paths are likely to contribute. One leads through the ^{15}O(α,γ)^{19}Ne reaction directly to a nucleus that has, under stellar conditions, no reaction path back into the CNO-isotopes. Alternatively, the ^{14}O(α,p)^{17}F(p,γ)^{18}Ne(α,p)^{21}Na reactions provide a possible path to larger masses, that is expected to dominate at high temperatures.

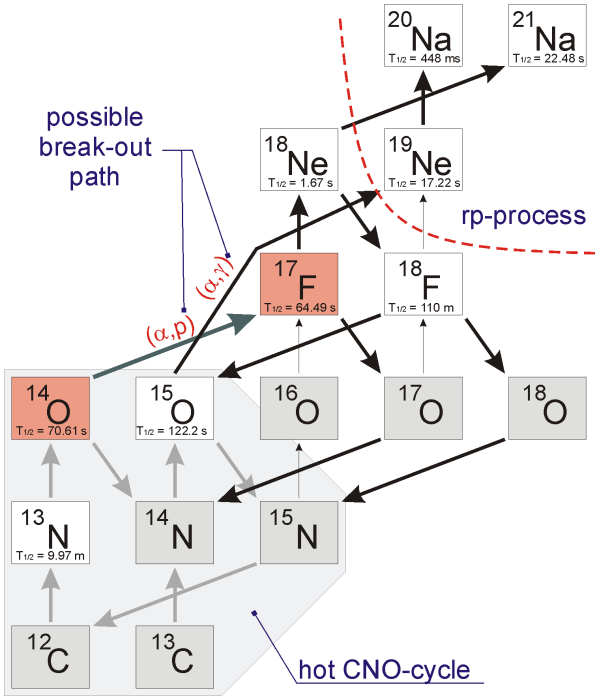

Fig. 2.3 Possible break-out paths from the hot CNO cycle into the rp-process. Once the dotted line is crossed, no astrophysical reaction leads back into to the (hot) CNO cycle.

In the break-out process, the $^{14}O(\alpha,p)^{17}F$ reaction potentially plays a role at different temperatures. At $T_9 > 0.4$, it might increase the energy production in the system by starting to bypass the ^{14}O β^+-decay with the $^{14}O(\alpha,p)^{17}F(p,\gamma)^{18}Ne(\beta^+)^{18}F(p,\alpha)^{15}O$ sequence. This increased energy production[7] by a factor of about 1.6 leads to a rise in temperature and might trigger the breakout via the $^{15}O(\alpha,\gamma)^{19}Ne$ reaction. At even higher temperatures, in the phase of a beginning thermonuclear runaway as expected in nova-explosions and X-ray bursts, the mass-flow will mostly proceed through the $^{14}O(\alpha,p)^{17}F(p,\gamma)^{18}Ne(\alpha,p)^{21}Na$ path, since the $^{15}O(\alpha,\gamma)$-reaction is suppressed by the relatively small α-width in the resonant channel. Part of the goal of this thesis is to put the knowledge about the $^{14}O(\alpha,p)^{17}F$ on firmer experimental grounds.

Besides novae and type I X-ray bursts, several other systems might be sites of the rp-process: Outer shells of supernova-explosions and accretion disks of massive black holes are among them. Also Thorne-Zytkow objects, massive stars with a neutron-star like degenerate core, are mentioned in the literature[8].

2.2 S-factor and Gamow Window

To calculate an actual astrophysical reaction rate $\dot{n}$, one needs to know the concentrations of the reaction participants, the cross-section of the reaction as a function of energy and the temperature of the system. Temperature herein is defined as long as the reaction participants, i.e. the ions, are in local thermal equilibrium, which can be assumed even in supernova-explosions. In general, for the charged reaction partners *l* and *m*, one writes

$$\dot{n}_{lm} = \frac{n_l n_m}{1+d_{lm}} \sqrt{\frac{8}{p m_{lm}}} \left(\frac{1}{kT}\right)^{\frac{3}{2}} \int_0^\infty E s_{lm}(E) e^{-\frac{E}{kT}} dE =: \frac{n_l n_m}{1+d_{lm}} \langle s_{lm} v \rangle \tag{2.1}$$

Herein, m_{lm} is the reduced mass of the ions *l* and *m*, d_{lm} is the Kronecker-symbol and $<s_{lm}v>$ is the rate-coefficient which has the dimension of [volume/time] and represents a reaction rate per particle pair. The *v* in $<sv>$ stands for velocity and stems from the initial integration over velocity in a Maxwell-Blotzmann distribution rather than over energy as in equation 2.1. For a given combination *lm*, $<s_{lm}v>$ is only a function of the temperature. Even in very hot stellar systems, temperatures do not exceed a few 10^9 K. This translates to *kT* of a few 100 keV at the most. The Coulomb energy E_C for the system ^{14}O and α, however, is located above 4 MeV. At energies below E_C, the $^{14}O(\alpha,p)^{17}F$ reaction has to proceed through tunneling. The probability to tunnel through the Barrier for the charged particle pair *lm* is described by the Gamow-factor in the cross-section.

$$s_{lm}(E) \propto e^{-G_{lm}} \; ; \; G_{kl} = \sqrt{\frac{E_{0,lm}}{E}}$$

$$\text{with } E_{0,lm} = 2m_{lm}\left(\frac{p\, Z_l Z_m e^2}{\hbar}\right)^2 \approx 1.958 \frac{m_l m_m}{m_l + m_m} (Z_l Z_m)^2 [MeV] \tag{2.2}$$

In the last approximation, the masses are in [*u*]. From here on, the indices *l* and *m* are dropped. The Gamow-factor dominates the magnitude of astrophysical cross-sections of charged particles. Therefore, the following definition of the astrophysical S-factor is widely used:

$$S(E) := s(E)\frac{E}{e^{-G}} \approx s(E)\frac{E}{e^{-\sqrt{\frac{796}{E}}}} \tag{2.3}$$

The last approximation refers to the $^{14}O + \alpha$ system. Having taken out the phase space factor and the penetrability, $S(E)$ contains the structural part of the nuclear cross-sections. It is expected to be only weakly dependent on energy for non-resonant processes. Writing $\langle sv \rangle$ using $S(E)$, one obtains

$$\langle sv \rangle = \sqrt{\frac{8}{pm}}\left(\frac{1}{kT}\right)^{\frac{3}{2}}\int_0^\infty S(E)e^{-\frac{E}{kT}-G}dE \tag{2.4}$$

The exponential function in equation 2.4 dominates the energy dependence of the integrand. It forms a temperature-controlled peak that determines the energy range, in which the S-factor of a reaction contributes to the reaction rate $\dot{n}$ in a stellar plasma. The peak is called Gamow-peak, and is shown in Fig. 2.4 for several temperatures. Its magnitude varies extremely with temperature. In the system $^{14}O + \alpha$, it increases by 35 orders of magnitude when the temperature is increased from $T_9 = 0.1$ to $T_9 = 1.5$.

To describe the slightly asymmetrical Gamow-peak, its maximum E_G and width at half maximum DE_G is used by approximating its shape with a Gaussian.

$$e^{-\frac{E}{kT}-G} \approx e^{-\left(\frac{E-E_G}{\Delta E_G/2}\right)^2}$$

$$E_G = \left(\sqrt{E_0}\frac{kT}{2}\right)^{\frac{2}{3}};\ \Delta E_G = 4\sqrt{\frac{kTE_G}{3}} \tag{2.5}$$

E_G is called Gamow-energy, and DE_G is the width of the Gamow-window, shown as a function of T_9 in Fig. 2.4, right part. In first order, only the $S(E)$-factor of a reaction within the Gamow-window contributes to an astrophysical reaction rate at a given temperature.

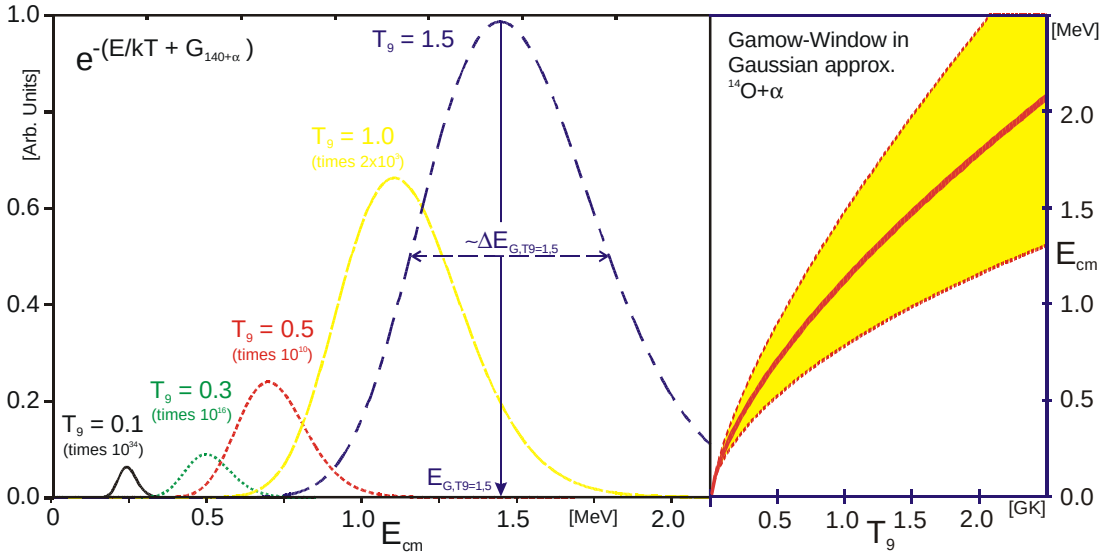

Fig. 2.4 **Gamow-Peaks for the $^{14}O + \alpha$ - system at different temperatures. Left: The exponential term in equation 2.4 for different temperatures. Right: The Gamow-energy E_G (solid line) and the width of the Gamow window, DE_G (filled area).**

3 The Nuclear Physics of $^{17}F(p,a)^{14}O$

The energetics of the $^{17}F(p,\alpha)^{14}O$- and $^{14}O(\alpha,p)^{17}F$ reactions are shown in Fig. 3.1. The heavy ions involved in the process are ^{17}F, ^{14}O and the compound nucleus ^{18}Ne. While excited states of ^{14}O cannot play a role since they are high above the energy range of interest, the excited state in ^{17}F at E_x=495.4 keV is a possible final state of the $^{14}O(\alpha,p)^{17}F$ process. The excited states in ^{18}Ne are candidates for resonances in a compound reaction.

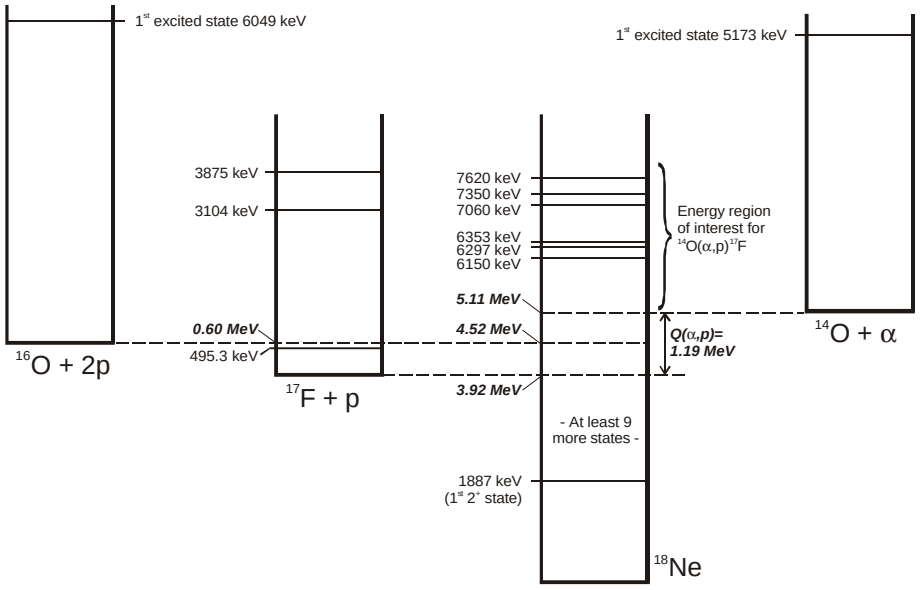

Fig. 3.1 The energetics of the $^{14}O(a,p)^{17}F$-reaction.

Both the $^{14}O(\alpha,p)^{17}F$-reaction, and also its time inverse counterpart can take place as a direct reaction or via the compound nucleus ^{18}Ne (Fig. 3.2). The cross-section of the direct mechanism shows a weak energy dependence, described by the overlap of an incoming and an outgoing wave-function and a penetrability function. The resonant contribution exhibits a strong energy dependence with the details depending on the structure of the compound states in ^{18}Ne. Since the single particle does "not know", from which reaction mechanism it originates, the two amplitudes have to be added. There is interference, independently for each value of J^p.

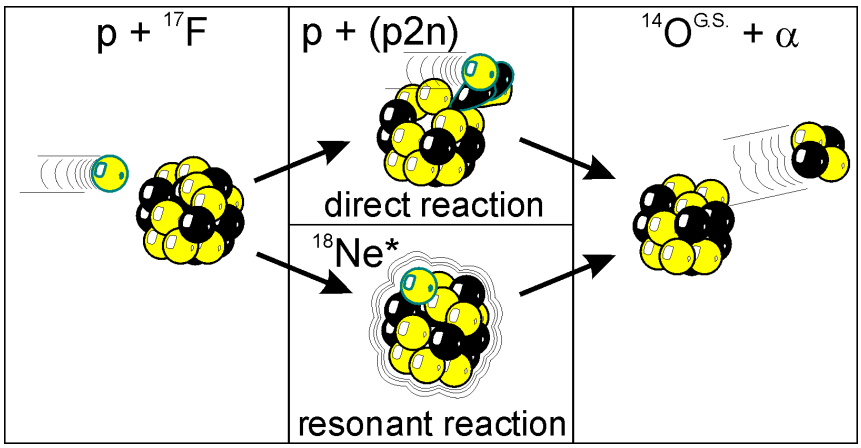

Fig. 3.2 For the $^{17}F(p,a)^{14}O$-reaction, there are two independent reaction mechanisms likely to contribute to the total cross-section.

3.1 Direct Reaction Mechanism

A simple estimate of the direct contribution from stripping to the $^{14}O(\alpha,p)^{17}F$ reaction or the inverse process can be achieved by using an optical model DBWA-code like DWUCK[9]. However, while reproducing the angular distributions fairly well, such calculations are known to underestimate the total cross-sections by huge factors[10].

An alternative way to describe the process is to assume a preformed α-particle in the target nucleus that is knocked out by the incoming proton. Here, the direct knock-on process can be seen as a direct capture, in which the excess energy is directly transferred to the preformed α-particle. The model has produced reasonable estimates for angular distributions and α-energy spectra for nuclei in all mass ranges, if the α-pre-formation factor in the target nucleus is known. Unfortunately, this is generally not the case and the measured numbers scatter quite substantially[11,12].

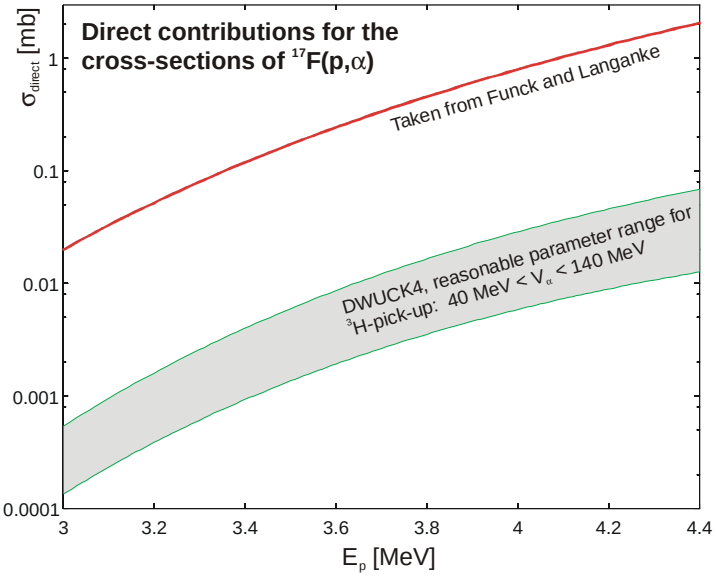

Fig. 3.3 Comparison of the direct contribution of the cross-sections for $^{17}F(p,a)$ from triton-pick-up (upper limit, DBWA) and an elaborate calculation[13] based on states of the nature $|^{17}F+p>$ and $|^{14}O+a>$.

To get a quantitative estimate, Funck and Langanke[13] used a microscopic calculation based on a set of antisymmetrized wave functions $|^{14}O+\alpha>$ and $|^{17}F+p>$ instead of a model involving the explicit formation of α-particles. This microscopic multi-channel model should ensure that the overlap of the entrance and exit channel is calculated in a consistent way and even resonances can be included, if their locations are adjusted to experimental values. Fig. 3.3 shows a comparison between a DWUCK-calculation for triton pick-up and the direct contribution predicted by Funck and Langanke. According to this work, the direct contribution to the cross-section s_{DR} in the range of interest are expected to fall between 0.001 and 1 mb for $^{14}O(\alpha,p)$, parameterized in the range of 1.5 MeV < E_{cm} < 3.5 MeV as

$$S(E) \approx 2.45 \cdot 10^5 \,[\mathrm{MeV \cdot b}];\;\; s_{DR} \approx \frac{2.45 \cdot 10^8}{E} e^{-\sqrt{\frac{768}{E}}} \,[\mathrm{mb}] \qquad (3.1)$$

However, it should be noted here that the dominant contribution to the astrophysical reaction rate is expected to arise not from the direct channel, but from the resonant contribution. An expression

for the direct contribution, that is based on its small energy dependence, can be derived from Eq. 2.4 by approximating[14] the exponential term by a Gaussian around E_G with the width DE_G. Integration yields:

$$\langle sv \rangle \approx \sqrt{\frac{2}{m}} \frac{\Delta E_G}{(kT)^{\frac{3}{2}}} S(E_G) e^{-\frac{3E_G}{kT}} \tag{3.2}$$

3.2 Resonant Reaction Mechanism

The resonant contribution to the cross-section is described by the formation and decay of a particle-unbound state in ^{18}Ne. The strength of the different possible decay- and formation channels is described by the partial width of the channel where all the partial widths add up to the total width G of the resonance. In case of the states in ^{18}Ne above $E_x = E_{sep,a} = 5.11$ MeV, the following channels are energetically open and can contribute to the total width: G_p, the width for a ground-state proton decay to ^{17}F, $G_{p'}$, the width for a proton emission to the 1st excited state of $^{17}F^{495}$, G_a, the width for alpha decay to the ^{14}O ground state and G_g, the width for de-excitation by a photon to the ground state of ^{18}Ne. In addition, there is a width G_{pp} for a two-proton decay directly to ^{16}O or possibly via the state at 3104 keV in ^{17}F in a two step process. A recent measurement[15] observed two proton emission from the 1^- resonance at $E_x = 6.15$ MeV in ^{18}Ne ($G_p \sim G = 50 \pm 5$ keV). The observed partial width G_{pp} was between 20 eV and 60 eV, very small compared to the total width of the resonance. Therefore, this width will be neglected from here on.

Due to the absolute strength of the electromagnetic interaction, typical values for G_g do not exceed a few eV. This is significantly smaller than the observed and expected total widths (some tens of keV) of the resonances in question. Therefore, this contribution to the total width of a resonance will be also neglected.

The resonant cross-section for a process from i to f depends on these widths which are of nuclear physics origin and on a statistical factor. It is given by the well-known[16] expression

$$s(E) = \frac{p}{k_i^2} \frac{2J_{res}+1}{(2J_1+1)(2J_2+1)} \frac{\Gamma_i(E)\Gamma_f(E)}{(E-E_{res})^2 + \left(\frac{\Gamma(E)}{2}\right)^2}$$

$$\text{with} \quad \Gamma = \sum_j \Gamma_j = \Gamma_p + \Gamma_{p'} + \Gamma_a \underbrace{+ \Gamma_g + \Gamma_{pp}}_{small} \tag{3.3}$$

Herein, k_i denotes the incoming wave number calculated for the incoming channel. J_{res} is the total angular momentum of the resonance, J_1 and J_2 are the spins of the incoming particles. It is important to note, that the Γ_j are fixed properties of the resonance, and do not depend on the actual reaction, i.e. weather the reaction is (p,α), (α,p) or (p,p'). Also, the energy dependence of the G_j can be neglected, if the change of the penetrability through the Coulomb barrier in the region of the resonance is small.

The total astrophysical reaction rate is given by Eq. 2.1. In astrophysical problems, the contribution of single resonances to the total yield is often of interest. For a single narrow resonance, the reaction rate can[17] be reduced to

$$\langle sv \rangle_{res} = e^{-\frac{E_{res}}{kT}} \left(\frac{2p}{mkT} \right)^{\frac{3}{2}} \hbar^2 wg_{if} \quad \text{with} \quad wg_{if} = \frac{2J_{res}+1}{(2J_1+1)(2J_2+1)} \frac{\Gamma_i \Gamma_f}{\Gamma_{tot}} \tag{3.4}$$

Therefore, in nuclear astrophysics, the resonance strength wg_{if} is regarded as the main property of a resonance with respect to the reaction $i \rightarrow f$.

Upper limits for the partial particle widths G_p, $G_{p'}$ and G_a can be estimated in a single-particle picture, the so-called Wigner-limit[18]. The following expression for a given angular momentum l, which deviates by a factor of 3/2 from to the original published version, is used:

$$\Gamma_{Wigner} = 3 \frac{\hbar^2}{mR^2} P_l \quad \text{with} \quad P_l = \frac{Rk}{G^2(Rk,l,h) + F^2(Rk,l,h)} \tag{3.5}$$

Therein, G and F are the regular and irregular Coulomb functions as defined in the N.B.S. Handbook[19], m the reduced mass, R the interaction radius, h the Sommerfeld parameter and k the center of mass wave number. Fig. 3.4 shows the single particle limits for G_p, $G_{p'}$ and G_a for the angular momentum transfers $Dl = 0 - 4$. They are calculated assuming that a single particle of given mass and energy is emitted from the potential of the nucleus through a given angular momentum- and Coulomb barrier.

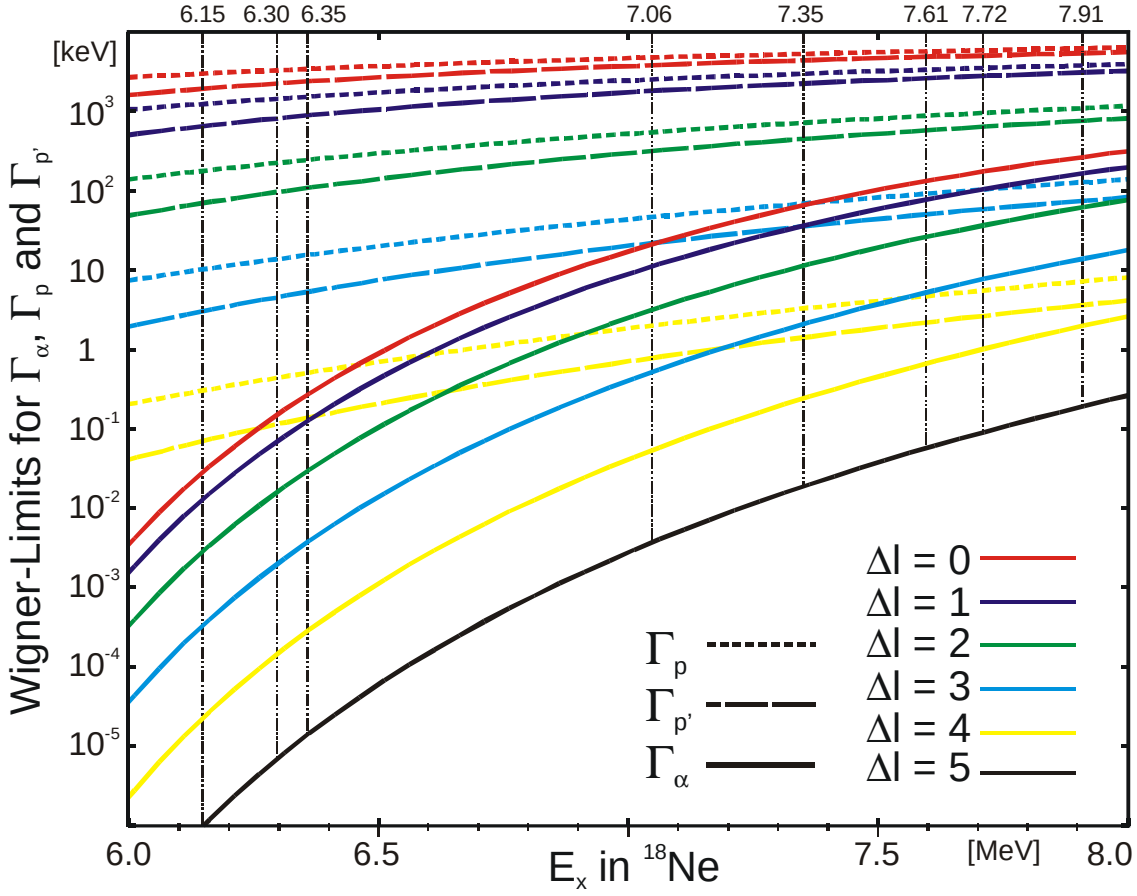

Fig. 3.4 The Wigner-Limits for G_p, $G_{p'}$ and G_a versus the excitation energy E_x in ^{18}Ne. It is important to note, that in this energy range, G_p and $G_{p'}$ are of the same magnitude for all angular momenta while G_a is one to five orders lower.

In appendix 8.3, a program to calculate a two-dimensional array $G_{\text{Wigner}}(E,l)$ is provided.

3.2.1 Alpha Angular Distributions

For resonant reactions, especially in the case of an isolated single resonance, the angular distribution of the reaction products can be calculated in a well-described way[20], if data about the contributing angular momenta is provided. In the case of no interfering waves form alternative reaction mechanisms, in the outgoing channel, the problem can be reduced to conservation of angular momentum and the requirement of orthonormalized final quantum states. The vector-algebra of this problem, however, is complicated since it involves the coupling of several angular momenta (spins and orbital) via generalized Clebsch-Gorden coefficients. Initially developed by G. Racah to describe transitions in complex atomic spectra, they were later adopted[21] to the problem of nuclear reactions in the form of the Z-coefficient.

The following expression, derived from the equations 5.13, 5.14 and 5.9 in Blatt and Biedenharn[20], describes the angular distribution for the case of a reaction through an isolated resonance with angular momentum J. For simplification, a single orbital angular momentum (L_{in}, L_{out}) and a single channel spin (CS_{in}, CS_{out}) for each of the incoming and outgoing particle pairs is assumed.

$$\frac{\mathrm{d}s(q)_{J,L_{in},CS_{in},L_{out},CS_{out}}}{\mathrm{d}\Omega} \propto \sum_{l}\left(Z(L_{in},J,L_{in},J,CS_{in},l)Z(L_{out},J,L_{out},J,CS_{out},l)\right)P_l(\cos q) \qquad 3.6$$

The channel spin CS is defined as the coupled spin of the corresponding particle pair and the function Z is the Racah-Z-coefficient. In many cases, the practical usefulness of this expression is reduced by many combinations of CS and the contributions from different allowed values of L for one J^p that interfere with each other.

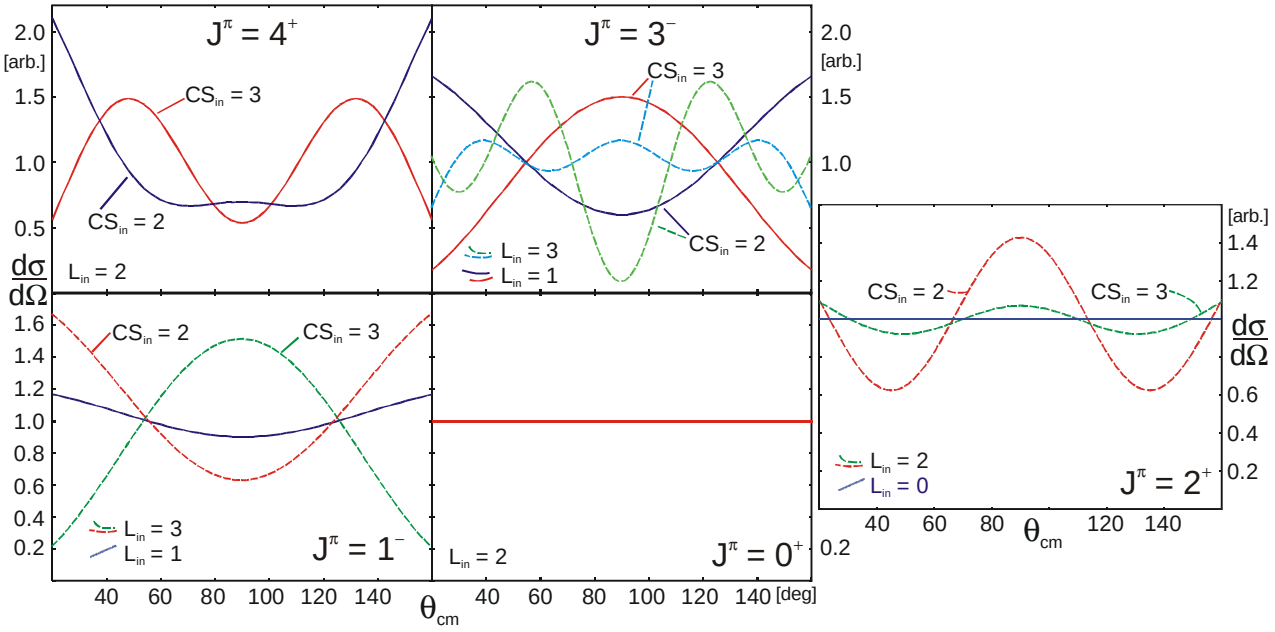

Fig. 3.5 Calculated a-particle angular distribution (single L_{in}, CS_{in}) resonances from 0^+ to 4^+ in the $^{17}F(p,a)^{14}O$ rection. In each case, the relevant values for L_{in} for the $^{17}F(p,a)$ studies were used. When allowed for the same L_{in}, the two channel spins (CS_{in}) of proton and ^{17}F (2 and 3) were calculated.

For the $^{17}F(p,\alpha)^{14}O$ reaction, the case is somewhat simpler, since CS_{out} for the pair $^{14}O + \alpha$ is 0, confining L_{out} to J. There are, however, two possible channel spins for CS_{in}, 2 and 3. From conservation of parity it follows that for one resonance either even or odd L_{in} are allowed, here odd

L_{in} for odd parity resonances. Choices for L_{in} are further restricted by the angular momentum barrier. Considering only L_{in} values for a Wigner limit $G_{p,Wigner} > 20$ keV, no more than two choices for L_{in} and for some J^p the two choices (2 and 3) for CS_{in} remain. The actual angular distribution is composed of the allowed cases for the J^p of a resonance. The mixing ratio is unknown, it depends on the shell model states forming the resonance. Especially for $J^p=1^-$, 2^+ and 3^-, different L_{in} are allowed, creating an interference term including Z-coefficients with two values for L_{in}, i.e. $Z(1,1,3,1,2,l)$ in the 1^--case.

Fig. 3.5 shows angular distributions for single L_{in}, natural parity resonances of $0 \le J \le 4$ in the $^{17}F(p,\alpha)^{14}O$ reaction. While $J = 0$ states show a flat angular distribution, resonances of other total angular momentum feature an inhomogeneous ds/dW, which depends on the realized l and CS value. In the special case of $J^p = 4^+$, a clear statement can be made. The comparison of the angles $q_{cm} = 40°$ and 80° should show a ratio of close to 2.0 independent of CS_{in}. For states of $J^p = 1^-$, 2^+ or 3^-, the situation is more complicated than shown in the picture. The interference term of the different L_{in} -values allows more asymmetric distributions than the single- L_{in} case, here due to an additional $P_2(\cos q)$ contribution.

3.2.2 R-Matrix Calculations

A very useful method for treating resonant reactions and scattering processes was introduced by Wigner and Eisenbud with their R-matrix theory[22], comprehensively described in a review article[23] by Lane and Thomas. It is a rigorous theory to describe reactions and scattering processes, based on a complete set of formal states confined in a volume and restricted by given energy independent boundary conditions on a surface. With a few assumptions, it quantitatively describes the cross-sections $s(E,q)$ of reaction- and scattering processes of charged and uncharged particles. These assumptions are: the process can be described in non-relativistic quantum mechanics and is a two-body process, i.e. there are two massive particles in both the entrance and the exit channel. Limitations originating from these assumptions can be partly lifted by special techniques.

For each state with a given angular momentum and parity, an angular distribution of the outgoing wave function can be deduced from the transferred angular momentum and the coupled spins of the incoming and outgoing particles (see section 3.2.1). The energy dependence of the amplitude is given by the states energy and its width. By the total angular momentum and the partial width, finally, the absolute amplitude is defined. By summing the contributions of all formal states, the scattering amplitude and thus $s(E,q)$ of a reaction or scattering process is described.

In principal, the R-matrix theory does not depend on any particular reaction mechanism. However, for practical purposes in nuclear theory, the model is used to describe resonant reactions that involve the formation of well-defined intermediate compound states. Therein, one thinks of pairs of particles that form the compound nucleus and thus the resonant states. These states are identified with the formal states of the basic theory. In the case of reactions with protons incident on ^{17}F, pairs would be (^{17}F and p), ($^{17}F^{495}$ and p') as well as (^{14}O and α). In the case of particles with spin, each possible coupled spin of a pair is treated separately, thus it represents its own channel. For each pair, each channel and each orbital angular momentum, a partial width is needed. The physics of the interaction is hidden in the set of level energies and widths. The angular momentum algebra is included in the formalism.

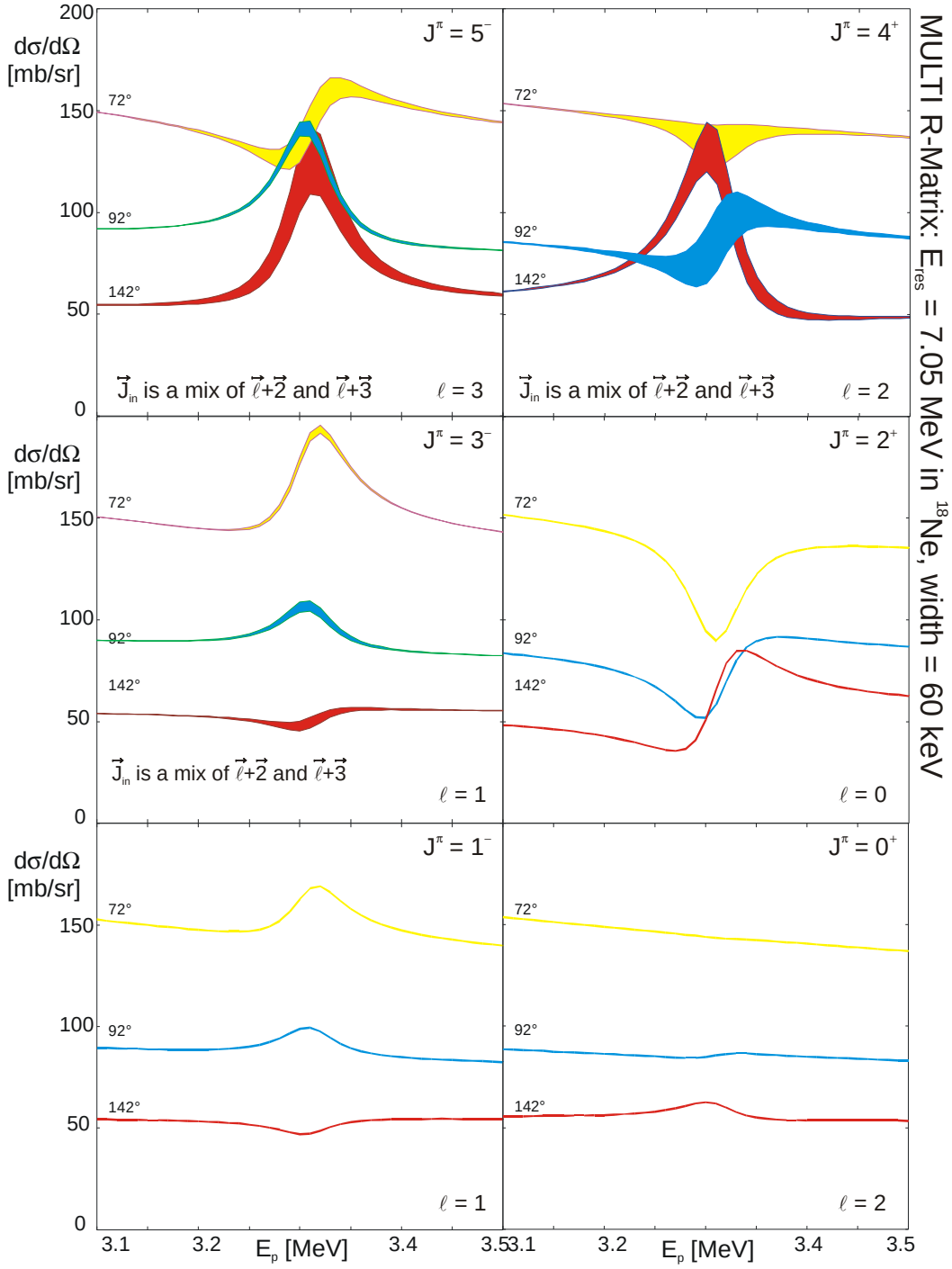

Fig. 3.6 **R-Matrix calculations (MULTI) for ^{17}F+p-scattering through an isolated resonance state at E_x=7.05 MeV in ^{18}Ne for three values of q_{cm}. All natural J^p-values up to $J^p = 5^-$ are shown. The calculation which includes the energy resolution of the experiment of 60 keV in the C.M.-system indicates that all shown alternatives can be distinguished.**

To apply R-matrix theory, one uses computer codes like MULTI[24] to perform actual calculations. These codes use a limited number of discrete states, channels and orbital angular momentum values. In all processes, this means neglecting far-away resonances and partial widths that are suppressed by large angular momentum barriers. However, the strong energy dependence of the Breit-Wigner formula leads to a dominance of nearby resonances. Also, at energies not far from

the Coulomb barrier, the neglect of large *l*-values is quite justified. Only when the level density increases to a degree where many resonances start to overlap, a R-matrix fit becomes increasingly difficult and ambiguous. In elastic scattering, the situation is more complicated. Here, nuclear scattering and Rutherford scattering interfere. While the scattering by the Coulomb potential and the resonant scattering can be calculated precisely, the nuclear potential scattering is treated rather approximate, i.e. in a hard sphere approximation.

In principal, the coherent electromagnetic- and strong potential scattering is a sensitive probe of the angular momentum of the resonances observed. The interference between the well-known Coulomb amplitude, the resonant amplitude and the not-so-well-known potential scattering amplitude gives rise to characteristic interference excitation functions. Fig. 3.6 shows a set of excitation functions for the lowest allowed *l*-values in the case of a single resonance in proton scattering of ^{17}F.

The weak point of calculation as the one shown in Fig. 3.6 is the simplified treatment of the potential scattering. While a hard sphere picture with a reasonably chosen radius will produce good results at backward angles, collisions close to the grazing angle might show significant deviations. Incorrect phases show an especially large effect due to the interference with a same-magnitude Coulomb amplitude. In the energy regime of the calculation in Fig. 3.6, this is the case at angles of approximately 90° in the center of mass system. In the case of ^{17}F(p,p)^{17}F, the cross-sections in this regime are over predicted by a factor of ~2.5 (see section 7, Fig. 7.11)

3.2.3 Determining the Resonance Width from Finite Target Thickness Data

Excitation functions measured in experiments are measured with a target of finite thickness and a beam of a certain energy spread. Therefore, the excitation functions always represent an average $s_{Av}(E_{beam})$ over the cross-sections $s(E)$ folded with the energy loss E_{loss} of the particles in the target and the energy distribution of the beam. Assuming the profile of the beam to be rectangular and the stopping power dE/dx of the beam particles to be constant throughout the target, the width of the beam can be added to the energy loss in the target to an effective energy loss E_{loss}. Then, the folding can be reduced to an integration, explicitly written in this form:

$$s_{Av}(E_{Beam}) = \frac{1}{E_{loss}} \int_{E_{Beam}-E_{loss}}^{E_{Beam}} s(E)dE \qquad (3.7)$$

Therein, E_{Beam} denotes the highest particle energy incident on the target. Since a rectangular energy distribution is only an approximation for the beam, it is not easy to determine this energy. For practical purposes, it is therefore more convenient to rewrite equation 3.7 in terms of the energy of a mid-energy beam particle in the middle of the target E_{Mid}:

$$s_{Av}(E_{Mid}) = \frac{1}{E_{loss}} \int_{E_{Mid}-\frac{E_{loss}}{2}}^{E_{Mid}+\frac{E_{loss}}{2}} s(E)dE \qquad (3.8)$$

We assume now a cross-section $s(E)$ which consists of a direct- and a single resonance contribution. The direct term $s_{BG}(E)$ changes only linearly with energy over the integration range. The resonant contribution is described by a Lorentz curve of the total area A [MeV fm^2]. Inserting these two terms into equation 3.8, the measured cross section s_{Av} can be written in the form

$$s_{Av}(E_{Mid}) = s_{BG}(E_{Mid}) + \frac{1}{E_{loss}} \int_{E_{Mid}-\frac{E_{loss}}{2}}^{E_{Mid}+\frac{E_{loss}}{2}} \frac{A}{2p} \frac{\Gamma}{(E-E_{res})^2 + \frac{\Gamma^2}{4}} dE \qquad (3.9)$$

The integral in this expression can be solved analytically. Doing this and writing s_{BG} as linear term, equation 3.9 turns into

$$s_{Av}(E_{Mid}) = s_0 + \frac{ds_{BG}}{dE_{Mid}} E_{Mid} + \frac{A}{E_{loss} p} \left(\arctan\left(\frac{E_{Mid} + \frac{E_{loss}}{2} - E_{res}}{\frac{G}{2}} \right) - \arctan\left(\frac{E_{Mid} - \frac{E_{loss}}{2} - E_{res}}{\frac{G}{2}} \right) \right) \qquad (3.10)$$

Using a least squares fit for the parameters s_0, ds_{BG}/dE_{Mid}, E_{loss}, A, G and E_{Res}, this analytical expression can be fitted to data. To limit the number of parameters, some can be taken from independent information, e.g. E_{loss} from the known energy loss in the target plus the beam energy width. For a background contribution $s_{BG}(E)$ that has a small d^2s/d^2E on the scale of E_{loss}, an independent additive fit function can be used instead of the linear term in equation 3.10. Fig. 3.7 shows the general behavior of the resonant part in equation 3.10. For the limit of no energy loss, it becomes the original Lorenz curve. The area under the curve is always given by the parameter A, independent of E_{loss}.

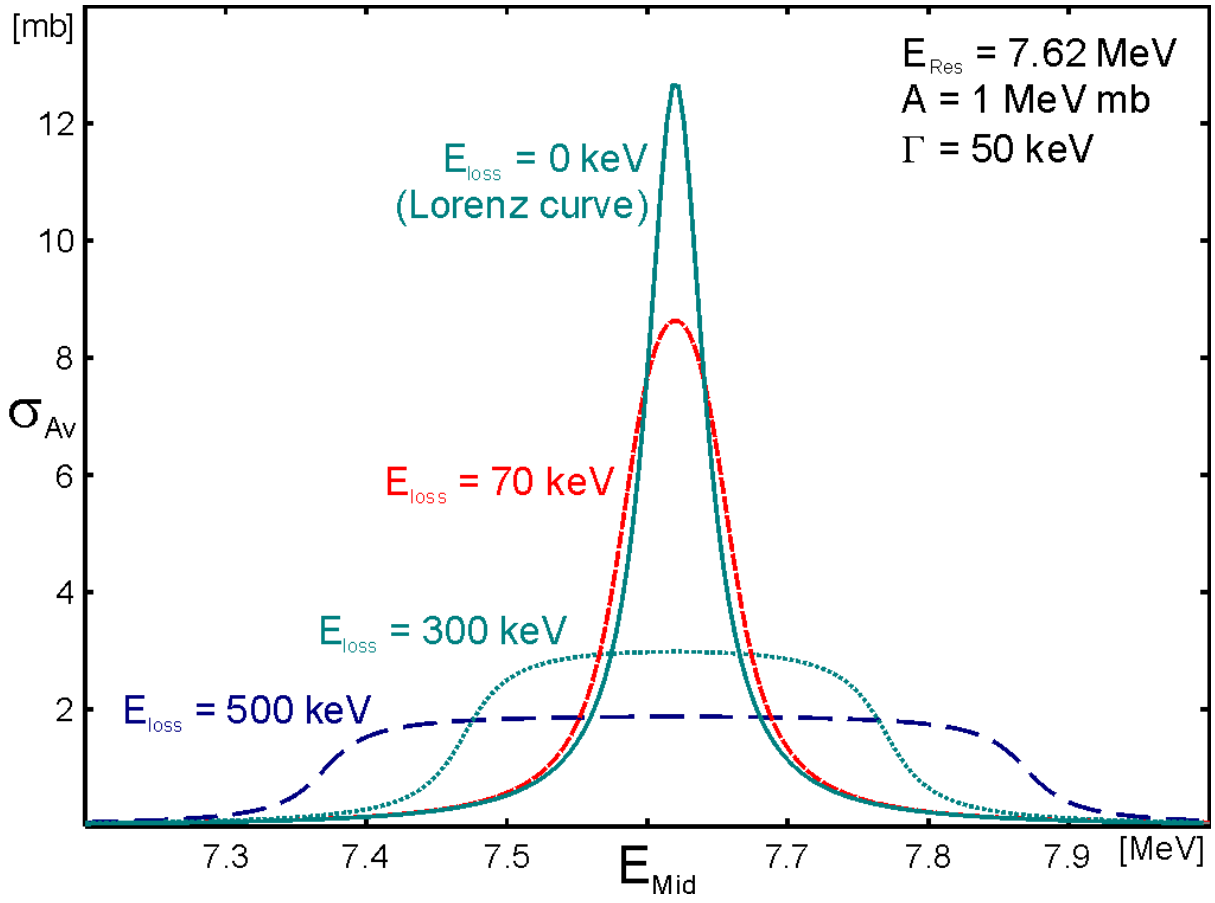

Fig. 3.7 **Expected cross-sections according to equation 3.10 for targets of different energy losses E_{loss}. Assumed is a resonance (G = 50 keV) at E_{Res} = 7.62 MeV with no background term. Note that a constant parameter A = 1 MeV mb produces, independent of E_{loss}, curves with this area.**

By comparison of equation 3.3 for the (p,α)-cross-section of a single resonance with the expression in the integral of equation 3.9, on can derive an expression for G_a as a function of G_p, G and the area A.

$$\Gamma_a = \frac{A}{2p^2} k^2_{(17F+p)} \frac{\Gamma}{\Gamma_p} \frac{(2J_{17F}+1)(2J_p+1)}{2J_{res}+1} \tag{3.11}$$

If the total width G is dominated by G_p, thus $G/G_p \sim 1$, expression 3.11 can be simplified by entering this and a non-relativistic approximation for $k_i(E)$. For the example of G_a from $^{17}F(p,\alpha)^{14}O$ and the energy in units of keV of excitation energy E_x in ^{18}Ne, one obtains

$$\Gamma_a \approx 2.75 \cdot 10^{-3} \frac{A}{2J_{res}+1} \left(E_{x,18Ne} - 3922\right)[\text{keV}] \tag{3.12}$$

Therein, A is given in units of [MeV mb]. In this approximation, G_a can be determined independently of the total width of the resonance. If one solves 3.12 for A and inserts the expression into 3.10, on finds that $s_{Av}(E_{Res}) = 2A/(E_{loss}\,\pi)$ becomes independent of G, i.e. a measurement of the cross-section on resonance determines G_a.

$$\Gamma_a \approx 1.38 \cdot 10^{-6} \frac{s_{Av}(E_{res}) E_{loss} p}{(2J_{res}+1)} \left(E_{x,18Ne} - 3922\right)[\text{keV}] \tag{3.13}$$

The energies are in keV and the cross sections in mb. Depending on which of the observables A or $s_{Av}(E_{res})$ is determined more accurately, equation 3.12 or 3.13 can be used to determine G_a. By stepping the beam energy over the resonance, every part of the beam energy distribution covers the full resonance in the target once. Therefore, equation 3.12 still holds, if the assumption of the energy distribution of the beam being rectangular is not valid. In this case, the measured excitation function might deviate from 3.10, but A is still the integral contribution of the resonant cross-section. Likewise, 3.13 still holds in approximation with any symmetric beam profile if the energy loss in the target is as big or larger than the energy width of the beam.

Finally, it should be pointed out that the values calculated for the astrophysical important parameter wg determined using equation 3.12 and 3.13 are still correct, if the total angular momentum J assumed for the resonance was wrong:

$$wg_{res,14O(a,p)} = (2J_{res}+1)\frac{\Gamma_a \Gamma_p}{\Gamma_{tot}} \approx (2J_{res}+1)\frac{\left(\frac{f(A,E_x)}{2J_{res}+1}\right)\Gamma_p}{\Gamma_p} = f(A,E_x) \tag{3.14}$$

Therein, $f(A,E_x)$ is the right side of equation 3.12 times $(2J_{res}+1)$. Instead, one could have written $f(s(E_{res}), E_x)$ where f would have denoted the right side of equation 3.13 times $(2J_{res}+1)$.

4 Basic Considerations for the Experiment

In this section, the scope of the experiments is given, and the basic considerations, that lead to the final concept are introduced.

4.1 The ^{14}O(α,p) Reaction at T_9 = 0.5 – 2

The main physics goal of the experiments described here is to quantify the cross-sections of the ^{14}O(α,p)^{17}F reaction in the upper energy range of astrophysical interest. At temperatures of $0.5 \leq T_9 \leq 2$, the location of the Gamow-window for ^{14}O+α translates into excitation energies of 6 to 8 MeV in ^{18}Ne. In Fig. 4.1, the Gamow-window is plotted into the level scheme of ^{18}Ne, along with an estimate for the peak cross-sections for the anticipated resonances. For the latter, it is assumed that the relative strength $G_i/G_{i,max}$ for protons and alpha-particles is the same and that G_{max} is given by the Wigner limit described in section 3.2. The calculation is done for resonances of $J^p = 1^-, 2^+, 3^-$ and 4^+ using the lowest allowed l-value for the proton channel. For the alpha channel, the orbital angular momentum is fixed to J of the resonance since both alpha-particle and ^{14}O have spin zero.

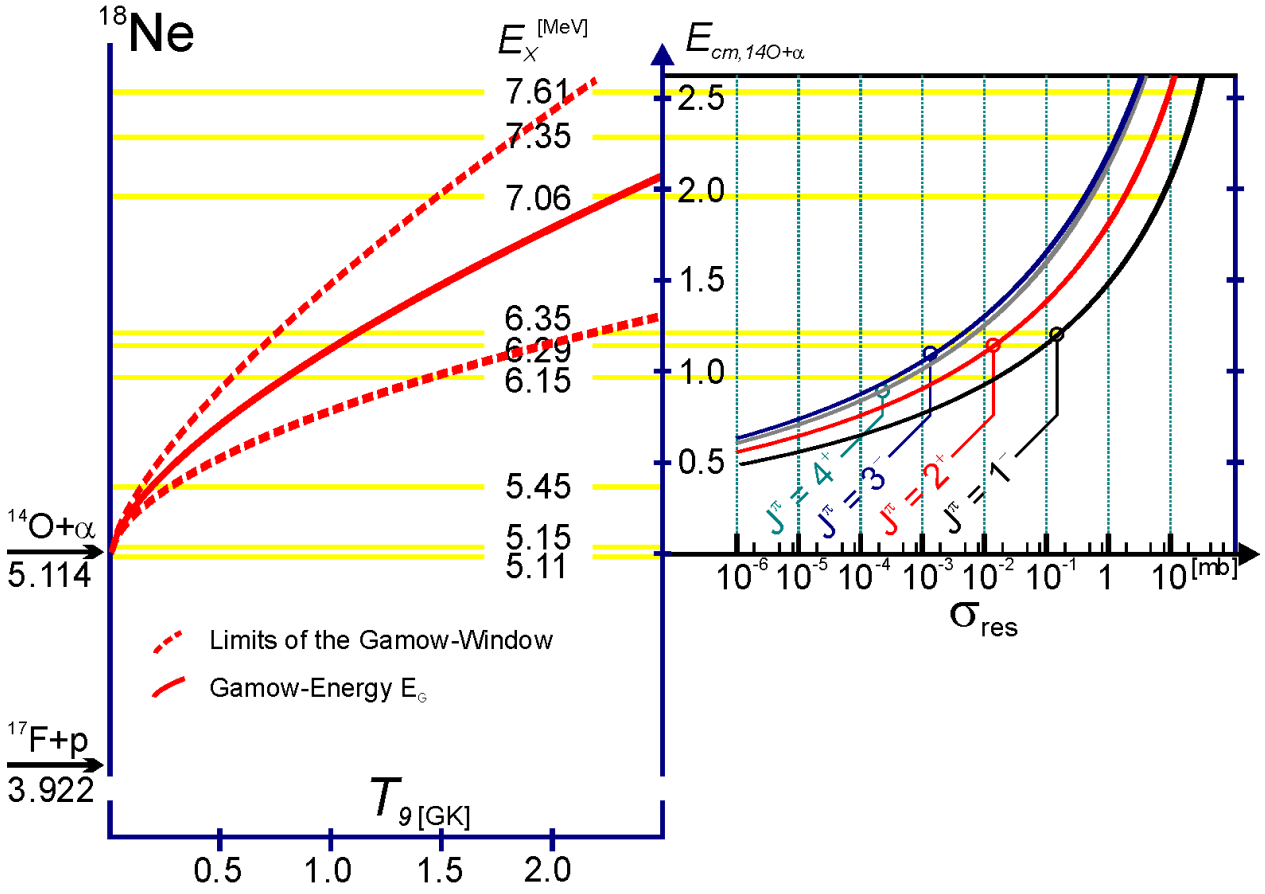

Fig. 4.1 **Left: Level-scheme of ^{18}Ne with the Gamow window. Right: Resonant peak-cross-sections for ^{14}O(α,p). G_α and G_p are asumed to be the Wigner limits for the lowest allowed orbital angular momentum matching the total angular momentum of natural parity resonances with J=1-4.**

A direct measurement of the $^{14}O(\alpha,p)$ reaction, however, is very difficult for experimental reasons. First of all, a beam or a target of ^{14}O ($T_{1/2}$=70.6 s) is required. The short half life makes a ^{14}O target virtually impossible. A ^{14}O beam seems possible, even so the very low energies of 10 MeV or less require a production technique other than the one used in our experiments. In addition, a ^{4}He target is required. This target has to be thin in terms of stopping power, since the produced ^{17}F ions need to leave the target in order to be detected. Possible choices are windowless gas targets or ^{4}He implanted in thin titanium- or aluminum foils. Both choices would not provide more than a few $\mu g/cm^2$ of ^{4}He. The gas target would pose enormous difficulties for its proximity to the detection setup that has to cover as much solid angle as possible.

With the available beam intensities and target thickness, only part of the goal could be achieved in any case. Assuming a 4 $\mu g/cm^2$ ^{4}He target, a strong 1^--resonance and a beam current of $5x10^5$ $^{14}O/s$, one would expect one $^{14}O(\alpha,p)^{17}F$ event every few hours in the E_x=6.3 MeV group of possible resonant states. This rate is very low if one strives to measure an excitation function. The group of states around 7.3 MeV seems more promising. Here the rates are expected to be up by two orders of magnitude. All in all, while not impossible, a direct measurement of the $^{14}O(\alpha,p)^{17}F$ cross-sections seems very difficult with the present capabilities.

4.2 Time-Inverse Reaction

Instead of directly measuring the excitation function of the $^{14}O(\alpha,p)^{17}F$ reaction, it is sufficient to determine the contributing particle widths G_p, $G_{p'}$ and G_a for resonant states in ^{18}Ne that dominate the process. Therefore, one could populate the resonances by any reaction and try to deduce the partial decay widths by detecting the decay products. Unfortunately, no stable combination of target and projectile exists that leads to ^{18}Ne as a compound nucleus. Alternatively, one can use a transfer process like the $^{12}C(^{12}C,^{18}Ne)^{6}He$ reaction, that was used by K. Hahn et al.[25] to determine the location of states in ^{18}Ne. To determine the partial width for protons and α-particles, however, it would be necessary to measure the full kinematics of all particles in the exit channel.

We decided to go another route and measure the time-inverse reaction $^{17}F(p,\alpha)^{14}O$ (Q = -1.19). While a ^{17}F ($T_{1/2}$ = 64.8s) target is as difficult to realize as a ^{14}O-target, a proton target is readily available in form of CH_2 foil. Also, a ^{17}F beam incident on hydrogen has the advantage of the fairly large laboratory velocity (extremely inverse kinematics) and, therefore, a great improvement in energy resolution of the beam in the center of mass system as well as reasonably high energy reaction products. Finally, all reaction products are emitted in the forward direction, allowing for a large detection efficiency.

If for a given resonance G_p is considerably larger than $G_{p'}$, then the $^{14}O(\alpha,p')^{17}F^{495}$ cross-section is small compared to the ground state transition $^{14}O(\alpha,p)^{17}F$. In this case, the cross-sections for the forward reaction can be directly calculated from the measured cross-sections of the time-inverse $^{17}F(p,\alpha)^{14}O$ process via the reciprocity law. Since the matrix elements for the forward- and the backward direction are the same, only the phase space factors differ for the two processes.

$$\frac{s_{(a,p)}}{s_{(p,a)}} = \frac{\frac{(2J_{17F}+1)(2J_p+1)}{k_a^2}}{\frac{(2J_{14O}+1)(2J_a+1)}{k_p^2}} = 12 \cdot \frac{k_p^2}{k_a^2} \approx 3.64 \frac{E_{cm(a,p)}}{\left(E_{cm(a,p)} - 1.19MeV\right)} \qquad (4.1)$$

Herein k_a and k_p stand for the center-of-mass wave number in the $^{14}O + \alpha$ and the $^{17}F + p$ - systems, respectively, and the J are the spins of the corresponding nuclei.

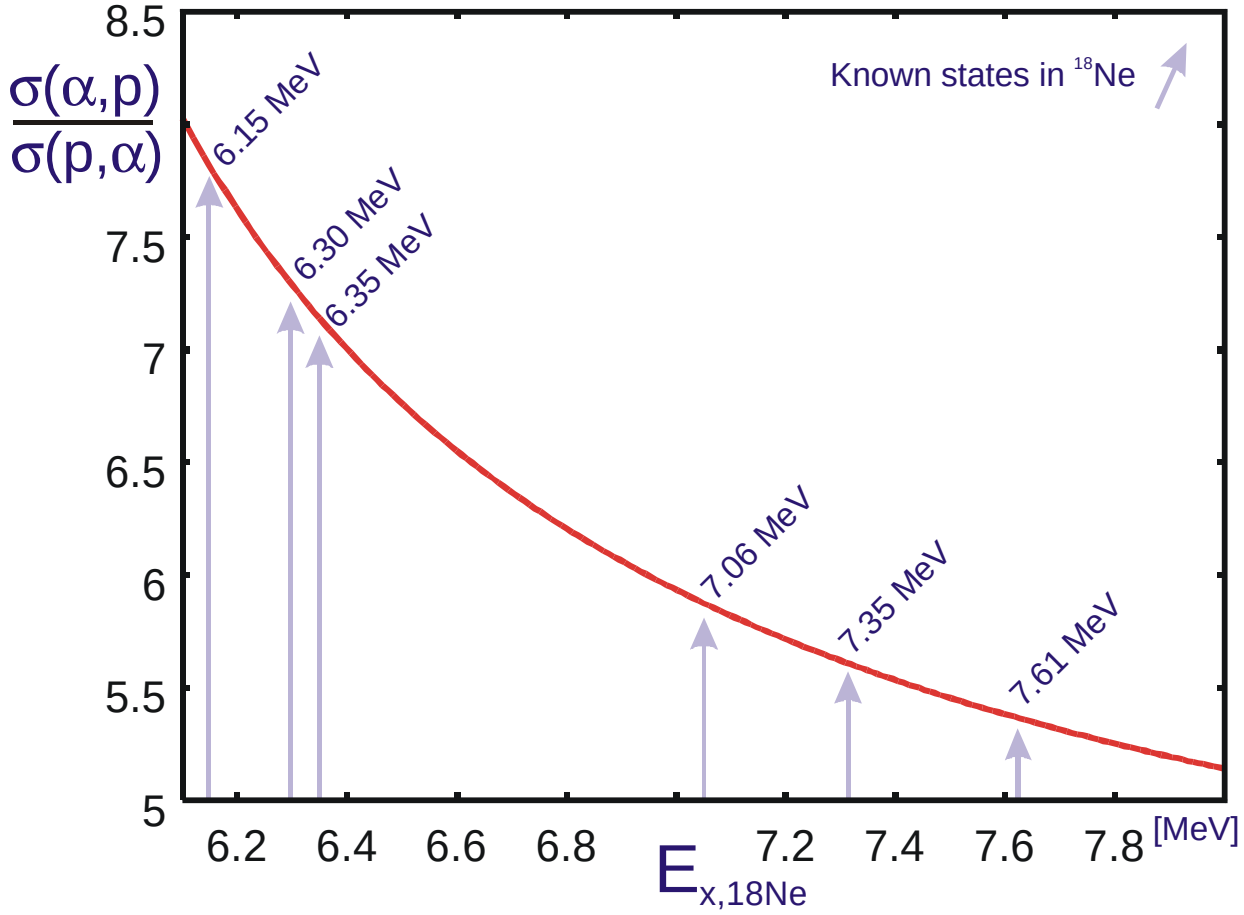

Fig. 4.2 For large ratios $G_p/G_{p'}$, the cross-section for the $^{14}O(a,p)^{17}F$ reaction is related to the cross-section of the time-inverse (p,a) reaction with a simple, energy dependent factor plotted in this graph. In the energy-range of interest, it varies between 5 and 8.

Fig. 4.2 shows the ratio $s(\alpha,p)/s(p,\alpha)$ over the energy range of interest and the locations of suggested resonances. While the indirect measurement reduces several problems, it does not remove the limitation on the possible energy range of our measurement due to low cross-sections mentioned in the last section. The unfavorable ratio of $s(\alpha,p)/s(p,\alpha)$ is about compensated by the larger target particle density of a CH_2 -hydrogen target compared to a ^{4}He-target. This makes it very difficult to measure the α-widths for low excitation energies in ^{18}Ne.

5 Production of a ^{17}F Beam using the In-Flight Technique

Most of the shorter-lived radioactive beams are produced presently either via the ISOL (Isotope-Separation-On-Line) technique[26,27,28] or the projectile-fragmentation method[28]. In the former, radioactive nuclei are produced in a thick target with a driver accelerator or a reactor and are subsequently accelerated with another machine. In the latter, a primary heavy-ion beam of several tens of MeV per nucleon is fragmented in a primary transmission target and the resulting fragments, following electromagnetic selection, are then directly used for experiments. The in-flight technique discussed in this thesis is similar to the fragmentation method. It provides isotopes close to stability without limitations due to lifetimes or chemical properties. In addition, it allows for an easy variation of the energy of the reaction products within a certain range and can be implemented in existing heavy ion-accelerators[29,30,31,32]. These advantages come at the price of restrictions on beam quality and on the isotopes that can be produced.

5.1 Basic Considerations of the In-Flight Production Technique

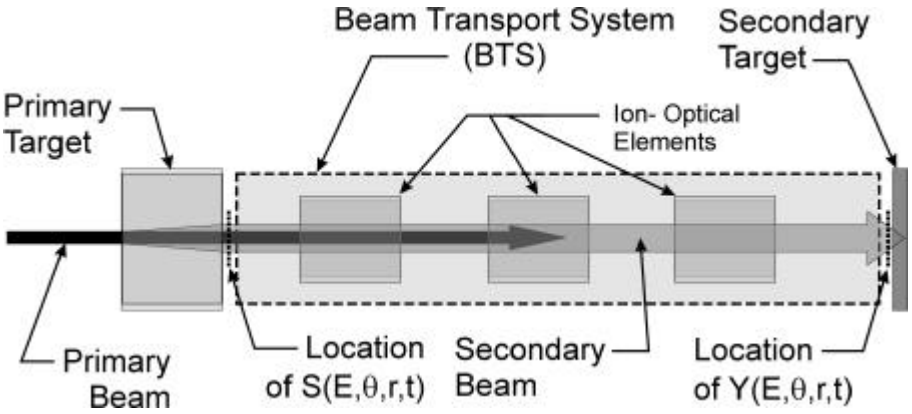

Fig. 5.1 Schematic of the in-flight production technique.

In the in-flight production technique (Fig. 5.1), nuclear reactions in a "primary" or "production" target are used to transform heavy ions from an intense primary beam into the desired radioactive, secondary beam. For a beam of heavy ions incident on a low-mass target, the velocities of the reaction products and of the incident ions are usually comparable. The challenge for the beam transport system (BTS) is to provide an efficient mechanism for suppressing the intense primary beam transmitted through the primary target while efficiently transporting the secondary beam.

In the following, the production of a secondary ^{17}F beam via the d(^{16}O,^{17}F)n reaction is used to discuss the in-flight-technique as we applied it to several cases (see Table 2 in section 5.4). The secondary ^{17}F particles are distributed in phase space with the characteristic parameters: Energy E, time t , angle q and position x,y with respect to the beam axis. Assuming radial symmetry, the particle position (x,y) in the plane perpendicular to the beam direction can be replaced by the radial distance r from the beam axis. Considering here only the transport of secondary ions in a single charge state, the yield function $Y(E,q,r,t)$ defines the distribution of $^{17}F^{9+}$ ions in phase space at the *secondary* target. $Y(E,q,r,t)$ depends on the distribution of these ions after the *primary* target, described by the function $S(E,q,r,t)$, and on a transport operator $T(E,q,r,t)$ that selects

and moves particles in phase space*, i.e. $Y = T\{S\}$. T represents a combination of a transport map and an acceptance function. To understand and predict Y, detailed knowledge of S and T, beyond characterization in terms of emittance, is required.

5.1.1 The Source Distribution S at the Target

For a given primary beam energy, the total number of product particles s_{tot} in S is determined by the reaction cross-section s, together with the areal particle density t_0 of the primary target, the primary beam current $I_{beam}(t)$ and the time span DT of observation. Here, the time span is assumed to be one periodic cycle, i.e. the pulse time of an RF-accelerator. To calculate s_{tot}, one has to integrate over the energy dependent cross section $s(E)$ as a function of the depth t in the target, $s(t)dt = s(E)dE\ dt/dE$ and account for the number of incoming particles $N_{incident}$.

$$s_{tot} = \int_0^{\Delta T} I_{beam}(t)dt \int_0^{t_0} s(E)dE \frac{dt}{dE} = N_{incident}\langle s\, t_0 \rangle \qquad (5.1)$$

The stopping power dE/dt in the target depends on all chemical components in the target layer in which reactions take place. Therefore, targets with a different chemical composition can result in different $<s\,t_0>$ for the same primary beam energy and the same density t_0. For slowly varying cross sections $s(E)$ in the energy range of interest, s_{tot} is given by the product of $Dtt_0 s(E_{mid})I_{beam}$, where E_{mid} is the energy at mid-target. Some total production cross sections for the d(^{16}O,^{17}F)n and p(^{17}O,^{17}F)n reactions are shown in Fig. 5.2.

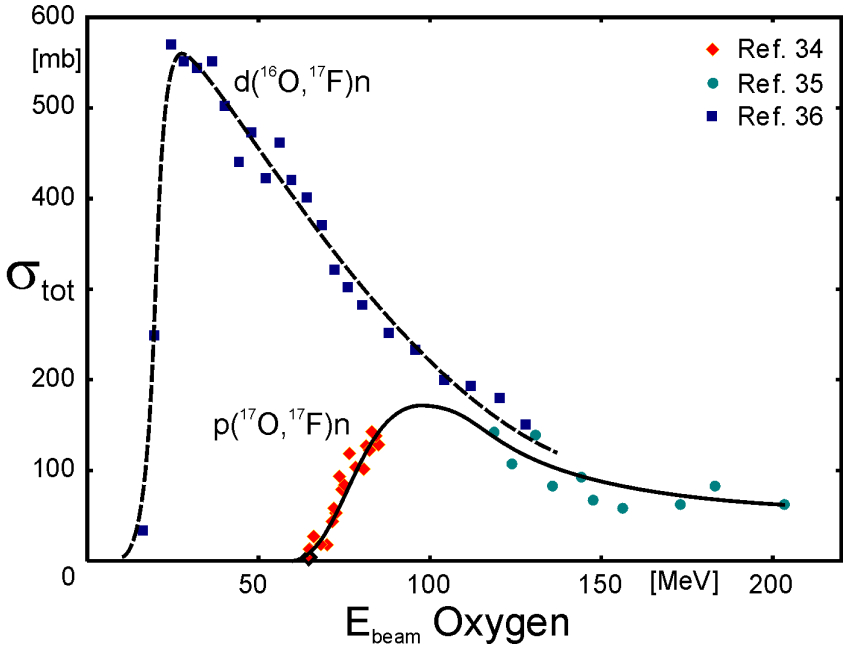

Fig. 5.2 Cross sections for the production of ^{17}F as a function of the energy using the p(^{17}O,^{17}F)n and d(^{16}O,^{17}F)n reactions. The data shown were taken from the literature[33,34,35]. The lines are drawn to guide the eye.

* Hereafter, for simplicity, $S(E,q,r,t)$, $T(E,q,r,t)$ and $Y(E,q,r,t)$ are simply labeled as S, T and Y, unless their dependence on certain parameters is specifically addressed. In this case, these parameters are given in parenthesis.

5.1.1.1 The Energy and Angle Dependence of $S(E,q)$

The energy and angle dependence of $S(E,q)$ is determined by the reaction kinematics, the differential reaction cross section $s(E,q)$, the energy and angular spread of the incident ^{17}O beam and the properties of the primary target. In general, no analytic expression for $S(E,q)$ can be given. An elegant technique to achieve an approximation is the use of a Monte Carlo simulation. The angle and energy spreads of the primary beam are usually small compared to the corresponding properties of the secondary beam and will therefore be neglected. Also, the fact that the $^{16}O(d,n)^{17}F$ reaction partially populates the first excited state in ^{17}F at E_x = 495 keV will be disregarded.

First, the effect of the reaction kinematics on the dependence of S on E and q will be considered. $S(E,q)$ for a ^{17}F beam produced via the $d(^{16}O,^{17}F)n$ reaction is as shown in Fig. 5.3. In the laboratory system, for constant differential cross sections ds/dW_{CM}, $S(E)$ is rectangular (solid line), while $S(q)$ exhibits a sharp peak at the maximum kinematic reaction angle q_{max}. Unlike the angular distribution ds/dW, $S(q)$ has to be 0 at 0° as a consequence of the differential angle ratio dq/dW.

The effect of an angular distribution ds/dW_{CM} in the case of the $^{16}O(d,n)^{17}F$ reaction[36,37] is shown in Fig. 5.3 by the dashed lines. In this case, the cross section is forward peaked, which has a drastic impact on $S(E)$: a large portion of the reaction products is shifted towards higher energies. The impact on $S(q)$ is less pronounced: while the slope at small angles is steeper, much of the yield remains at large angles.

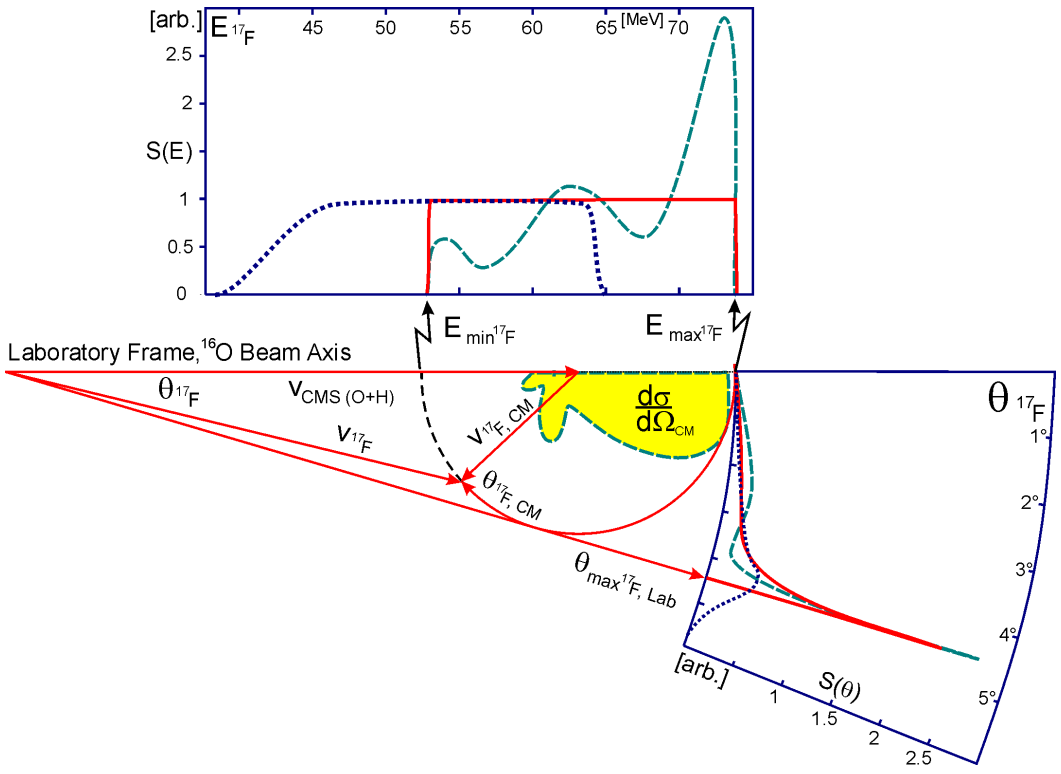

Fig. 5.3 **$S(E)$ (top) and $S(q)$ (lower right) for ^{17}F from the $^{16}O(d,n)^{17}F$ reaction with a 67 MeV ^{16}O beam incident on a thin (0.01 mg/cm^2) and a thick (1.6 mg/cm^2), windowless deuterium target. The kinematic situation is shown along with the measured[36,37] angular distribution ds/dW_{CM} in the center of mass system. Solid lines: ds/dW_{CM} isotropic, thin target. Dashed lines: experimental ds/dW_{CM}, thin target. Dotted lines: isotropic ds/dW_{CM} with energy loss and straggling effects, thick target.**

Straggling and energy losses in the thick primary target impact $S(E)$ and $S(q)$ by slowing and deflecting particles both before and after a reaction. The straggling in angle and energy varies with the square root of the target thickness, while the total energy loss is linear with the thickness. The Monte Carlo code TRIM[38] and the code described in section 6.3.4 were used to simulate these effects. The dotted lines in Fig. 5.3 show the impact of these effects. To demonstrate these effects in isolation, ds/dW_{CM} was assumed to be constant. The distribution $S(E)$ is shifted as a whole to lower energies by the energy loss, with increased width and slight tails at high energies and a slow fall-off at low energies. The sharp kinematic peak in $S(q)$ is broadened by particles scattered to smaller and, mostly, larger angles through small angle scattering. While the energy straggling is a relatively small effect compared to the width of $S(E)$ from the reaction kinematics, the small angle scattering can be of the same magnitude as the reaction opening angle.

Additional distortions of the kinematic distribution arise from several second order energy loss effects in the target. Reactions take place at different depths (and thus at different energies) in the target, creating particles with different opening cones and kinematic energy spreads. The specific stopping powers of the primary and the secondary beams and their energy dependence give rise to further modifications. A secondary particle produced in the first layers of the target has to travel through the rest of the material as a different species than the primary beam ions, experiencing a different stopping power. Fig. 5.4 illustrates the effect in the (q_{lab},E_{lab}) space due to the larger stopping power of the ^{17}F secondary particles. Especially for the backward solution, the kinematically defined relationship between angle and energy of the secondary beam particles is considerably weakened. At the same time, particles corresponding to the high energy forward solution loose less energy than these corresponding to the backward solution on the way out of the target. The lower part of Fig. 5.4 shows the results of a Monte Carlo simulation of these effects on the products of a 75 MeV ^{16}O beam from a 1.6 mg/cm^2 D_2 target.

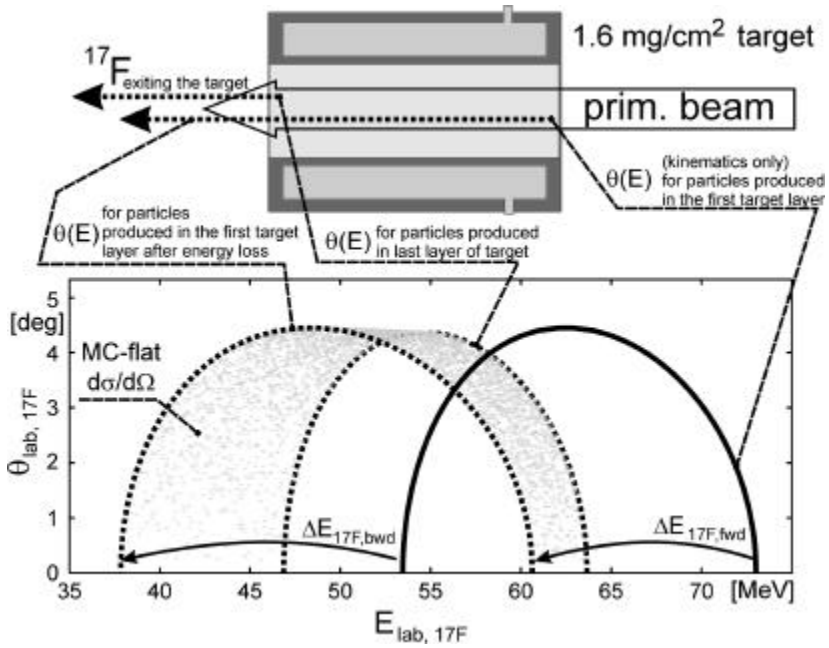

Fig. 5.4 The effect of the stopping power dependence on *Z* and *E* of an ion. The points are the results of a Monte Carlo simulation of the distribution of ^{17}F ions produced by a 75 MeV ^{16}O beam incident on a 1.6 mg/cm^2 deuterium target in a plot of q vs. E. The solid line indicates the kinematic curve for reactions in the first layer of the target. The dotted lines show the kinematic curves for particles generated in the first layer of the target after leaving the system and for particles generated in the last layer of the target.

5.1.1.2 The Radius and Time Dependence of S(r,t)

For $S(r)$ and for $S(t)$, the physical length of the production target is the most important factor. The width of $S(r)$ is given to a good approximation by the width of the radial distribution of the primary beam incident on the primary target plus a second term, which depends to first order linearly on the length of the target.

For most purposes, the time dependence of $S(t)$ can be assumed to be identical to the time structure of the primary beam, if the target does not extend more than a few cm in the beam direction. In linear accelerator systems with RF cavities and debunching capabilities, the primary beam has a sharply defined time structure with bunch lengths as short as 200 ps (FWHM) or less. In such systems, especially in an arrangement with large angular acceptance, even a moderately extended target of a few centimeters can have a significant influence on $S(t)$. This arises from the different locations in the target, where particles of distributed energies are created and from the different masses and stopping powers of the primary and secondary beam ions. For particles emerging with the same energy from a moderately extended target, the time distribution width is given by a constant term of the order of the time width of the beam bunches plus a second term which, to a good approximation, increases linearly with the length of the target. A Monte Carlo simulation for the d(^{16}O,^{17}F)n reaction in a 3.5 cm long D_2 target (1.6 mg/cm^2, 76 MeV ^{16}O beam, bunch width 0 ps) yielded a 60 ps bunch width for ^{17}F particles of 65 ± 0.25 MeV. With the same parameters, the ions emerging at 65 MeV from a 7 cm long target are distributed over 120 ps.

5.1.2 Transport Considerations

Which part of the distribution $S(E,q,r,t)$ can actually be used depends on the beam quality required in the specific experiment (i.e., which E, q, r and t are acceptable) and on the ability of the beam transport system (BTS) to move as much as possible of S into the acceptance window. Many nuclear physics experiments require a well-defined projectile energy and angle as well as a small beam spot. At the same time, the intense γ, X-ray and neutron radiation at the production target potentially interferes with experimental arrangements. To physically separate the production target from the secondary target and to control the quality of the secondary beam, a number of optical components like solenoids, magnetic dipoles and quadrupoles as well as debunching resonators can be used. The BTS and thus T in the equation $Y = T\{S\}$ moves particles in phase space from a location in S to a desired position in $Y(E, q, r, t)$.

The transport efficiency is defined as the fraction of all secondary particles whose descriptive parameters do not exceed the maximum allowed values for energy deviation DE_{max}, incident angle q_{max} and radius from the beam axis r_{max} on the secondary target. An upper limit on the transport efficiency can be obtained by comparing the product $q_{max} \times r_{max}$ with e_{St}, the particle-normalized integral over r times q of the source distribution S. e_{St} is a quantity closely related to the transverse emittance of the product distribution, and I drop the distinction even though the phase space population is non-statistical. This integral is generally approximated by a sum over the properties of the particles created in a Monte Carlo simulation of the target. If the product $q_{max} \times r_{max}$ is smaller than e_{St}, only part of the distribution S can be transported to the target station.

In RF-accelerators, such as the ATLAS linac, there is a correlation between the velocity and the time of arrival of a particle at a given location in the BTS. This makes it possible to use an RF

field to manipulate the longitudinal phase space and, thus, to reduce the energy spread of the reaction products. Limitations may arise from the achievable electric fields as well as from phase-space population. Numerically, this can be quantified by the normalized integral e_{Sl} over the velocity deviation *Dv* times the deviation in time *Dt* of the particles from the centroid of the distribution. e_{Sl} is closely related to the longitudinal emittance. The non-linear effects of the RF-field of the debunching resonator limit the maximal useful *Dt*, and therefore the minimum achievable *DE*. A limit of the transport efficiency can be obtained by comparing this *DE* with DE_{max}. In a full calculation of the total transport efficiency, phase-space related limits are to be combined with cuts arising from geometrical limitations in the BTS.

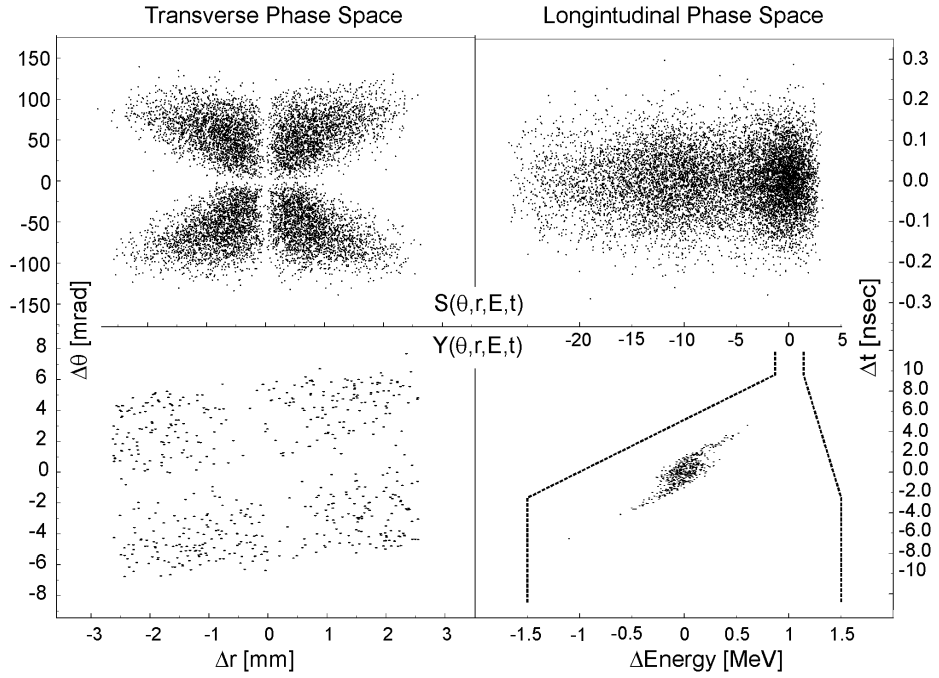

Fig. 5.5 Results of a Monte Carlo simulation of *S* (s_{tot} = 10,000) and *Y* for the setup used at Argonne. $^{17}F^{9+}$ ions are produced via the d(^{16}O,^{17}F)n reaction in a 1.6 mg/cm^2 D_2 gas target of 3.5 cm length with 1.9 mg/cm^2 HAVAR™ windows. The resulting *S*(*E*,*q*,*r*,*t*) is shown in the two upper panels. *S* is then used as input for a radially symmetric transport code simulating the impact of a debunching resonator and of the beam-optical elements and apertures located in the 15.5 m long path between the primary and the secondary targets. The calculated transport efficiency is 5.9%.

Fig. 5.5 presents phase space diagrams for *S* (upper panels) and *Y* (lower panels) from a Monte Carlo calculation simulating a 1.6 mg/cm^2 D_2 gas target with a length of 3.5 cm and HAVAR™ entrance and exit windows of 1.9 mg/cm^2 thickness, using the d(^{16}O,^{17}F)n reaction. The 10,000 particles were generated and used as an input for the radially symmetric transport code LINRAY[39]. LINRAY simulated the effects of the 15.5 m long BTS between the primary and secondary target, including the debunching resonator and the optical elements as well as the geometric limitations that cause particle losses. Details of the ion-optical arrangement used at ATLAS are given in section 4.2. Thus, the program represented an approximation of the operator *T*, acting on *S* and calculating the expected *Y* that contained in this case 594 transported particles. The predicted transport efficiency of 5.9% for $^{17}F^{9+}$, which corresponds to an over-all efficiency of 3.5% by accounting for the charge state distribution, is in reasonable agreement with the experimentally observed ~2.5%. The discrepancy is most likely caused by a reduction of the effective target thickness due to local heating of the D_2 gas along the beam axis and to the effects of quadrupole magnets which were modeled as radially symmetric lenses.

The calculated energy distribution $Y(E)$ of the particles at the secondary target is compared with a measured distribution at 65 MeV in Fig. 5.6. For a realistic time width of Dt = 175ps for beam pulses incident on the gas cell target, an energy spread of ~400 keV (FWHM) is obtained, in good agreement with the experimental results. The experimental data show a slight tail on the high energy side which can be explained by a minor error in the RF phase of the bunching- and debunching resonators, magnified by non-linear effects in the RF field of the second resonator acting on a wide time distribution.

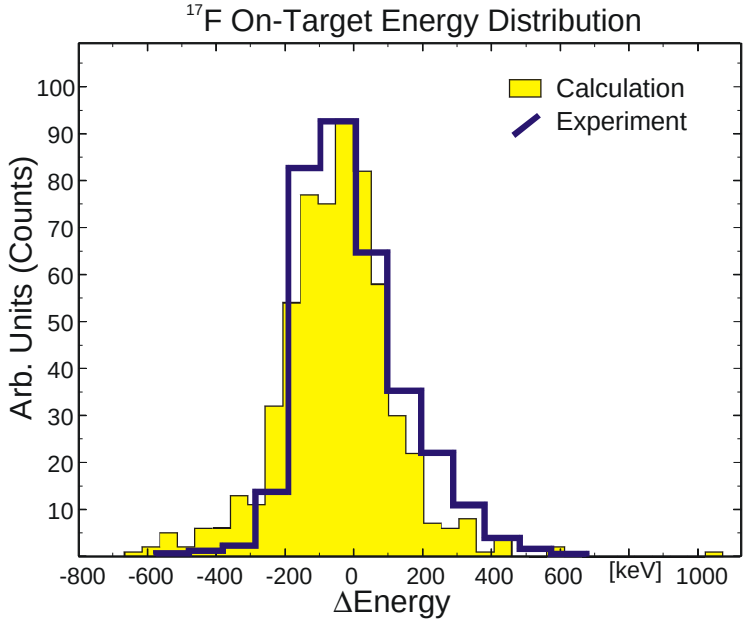

Fig. 5.6 Comparison between the simulated (filled peak) and the observed (bold line) energy distributions $Y(E)$ on the secondary target, normalized to each other. The ^{17}F beam energy was 65 MeV.

5.1.3 Typical Requirements for Production Reactions and Production Targets

For nuclear physics experiments, the usual requirements on the secondary beams are: high beam currents, a small beam spot, a small angle spread of the incoming projectiles and a small energy spread. Based on the discussion in sections 5.1.1 and 5.1.2, this translates into several general requirements for the efficient production of a given radioactive beam.

1.) In some cases, there is a choice between several reactions to produce the same secondary beam. Inverse reactions (heavy beams on light targets) such as inverse (p,n), (d,n) or (3He, d) processes, preferably with negative Q-values, should be chosen because of the narrow opening angle of the reaction products in the laboratory system. Forward-peaked differential cross-sections are an advantage. Unfavorable values of these parameters of a specific reaction may be offset by larger total cross-section.

2.) The angle and energy acceptance of the BTS should be as large as possible. Even for inverse reactions, the opening angles with respect to the beam axis are of the order of degrees and the energy spread is typically several MeV.

3.) The size of the beam spot on the primary target should be small. In the case of an RF-based accelerator system with energy debunching capabilities, there should be a tight time focus at the primary target. These conditions minimize e_{St} and e_{Sl}.

4.) The primary target should be designed to accept as large a beam current as possible.

5.) The primary target should be short, designed to minimize small-angle straggling. Since the width of $S(r)$ increases linearly with the physical length of the target, e_{St} also increases linearly with this quantity.

6.) The primary target should have a high isotopic concentration in its active area. Because of the increased energy loss, compounds containing the target nucleus represent an inferior choice compared to an isotopically pure material.

7.) Passive layers (windows), especially on the exit side of the target, should be as thin as possible. Thick windows induce increased small angle straggling, thus increasing e_{St}. They widen the energy distribution of the products, thereby increasing e_{Sl}. They also increase the energy loss of the primary beam, raising the total heat load on the target assembly. Increased straggling of the transmitted primary beam causes more secondary beam contamination due to energy tails of the primary beam.

5.2 The Primary Gas Target

As hydrogen target in the ATLAS beam-line, a solid state target like H-rich compounds (CH_2, ...) was not an option. It was shown that such material cannot withstand the thermal stress, even when mounted on a rotating disc[40]. A windowless gas target solution would have been very attractive. However, the close proximity of the superconducting debunching resonator and the need of placing a focussing element directly behind the target made such a solution very difficult to realize. The surfaces of the resonator are cooled to 4°K, requiring a good vacuum in the vicinity. Due to the refocusing solenoid, however, there was no room for pumps downstream from the target. Therefore, a gas-cell solution with metal windows was chosen.

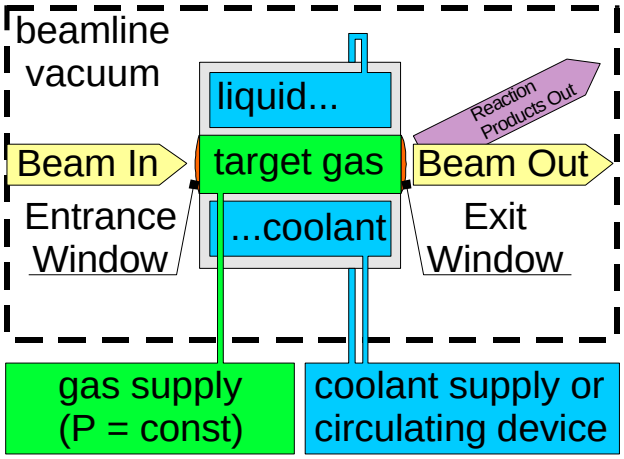

Fig. 5.7 General scheme of a production gas cell with its major utilities.

Transmission gas cells with metal windows provide high target densities without the great pumping speed needed for windowless targets. Moreover, they do not restrict the solid angle of the incident and produced particles by the apertures of a differential pumping system. This comes at the price of increased energy loss and small angle scattering of the incoming beam and the outgoing reaction products. Also, the maximum tolerable beam current is limited and at sufficiently high energies, reactions in the window foils can occur.

The basic scheme for the gas target is shown in Fig. 5.7. A target gas volume is enclosed by two foil windows and a double walled container, which is cooled by liquid nitrogen. In combination with a pressure regulation device, the cooling systems maintains constant density of the gas, an important requirement for many applications. In addition, the cooling provides an increase in density over a room temperature system. To realize an operating system, many details need to be addressed to ensure good performance and reliable operation. In the following, some details of the components involved will be given.

5.2.1 Cooling System

In principal, any cooling liquid can be used to define a constant temperature of the cell during operation. Early experiments carried out at Argonne used a mixture of alcohol and water with a commercial cooling unit. The system was found to work reliably and served its purpose well. However, for its precisely defined temperature and its large cooling power, liquid nitrogen appeared to be ideal for the application at hand. For a given pressure, its low absolute temperature of 72°K provides 4 times higher densities for hydrogen or helium targets compared to room temperature. It also is reasonably inexpensive and available at the target position in the ATLAS beam-line system. The heat load on the system was estimated to be a few tens of watts, most of which is caused by heat conduction to the outside and imperfect insulation of the cooling lines. The beam energy loss in the target contributes less than 5 watts.

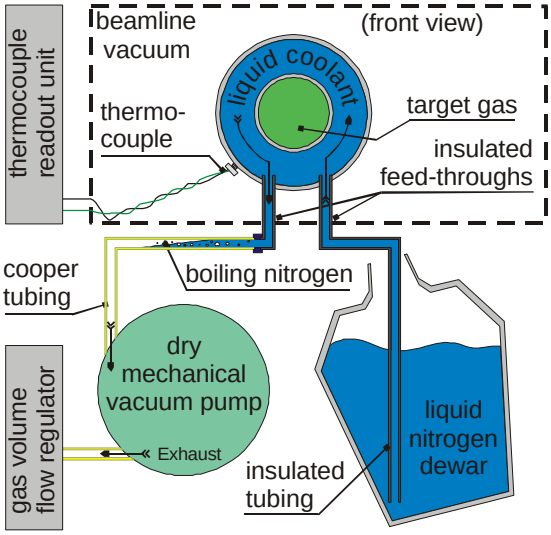

Fig. 5.8 Cooling scheme of the gas target at ATLAS, utilizing liquid nitrogen by pumping the coolant through the system.

Unlike a coolant far from its boiling point, nitrogen draws its cooling power not from its heat capacity but rather from the enthalpy needed to boil off a small fraction of the liquid. Re-cooling and circulating nitrogen is for this reason (and other mechanical problems) a non-trivial project and not worthwhile for small applications with heat loads of a few tens of watts. Instead, nitrogen from a supply is transferred through the system and then discarded. In most cases, it is necessary to boil off the leftover liquid before discarding. This was done here in a piece of intentionally poorly insulated copper tubing.

An obvious way to realize liquid nitrogen transport through the gas cell is to use the pressure of a nitrogen line, as provided at ATLAS, or a reservoir in combination with a gas bottle to force nitrogen through the system. In this case, a gas-flow regulation would limit the flow through the

system directly after a boil-off-line. However, the use of a mechanical (dry) pump to force the nitrogen through the cooling system, as illustrated in Fig. 5.8, was found to be more dependable and safer. The main advantage is that, once the flow of nitrogen through the system is correctly adjusted, loss of cooling due to gas bubbles in the supply line is unlikely as long as the nitrogen supply lasts. Also, an accidental over-pressuring of a necessarily closed system is excluded since using the pumping technique, the supply devour is not pressure-sealed. It can be refilled by an automatic system, that measures the LN_2 level, and opens or closes a valve to a larger supply (here the ATLAS liquid nitrogen line) accordingly. The flow of nitrogen is regulated after the dry pump, using gas that, heated by the pump and the copper line, has fairly constant density. To maintain constant cooling of the target, it is only required to maintain the boiling point of the nitrogen after the cell (before the pump) in the copper line. The temperature of the target was monitored constantly by thermocouple elements.

5.2.2 The Gas Handling- and Regulation System

In a gas target, the density of the desired target-isotope should remain constant over the time of an experiment. This is achieved by keeping both temperature and pressure as constant as possible. Reasons for a change in pressure are a slight leakage of the target and the expansion of gas due to local heating by the beam. Therefore, an active regulation of the target gas pressure is required. However, it is desirable *not* to have gas circulating in and out of the target. This would create additional heat-load on the cooling system and require larger amounts of possibly expensive (^3He) or dangerous (H_2) materials. Finally, a system that limits the maximum amount of gas discharged in the case of a catastrophic window failure is desired. A large amount of gas released in the high-vacuum system of a heavy ion accelerator has the potential of causing serious damage.

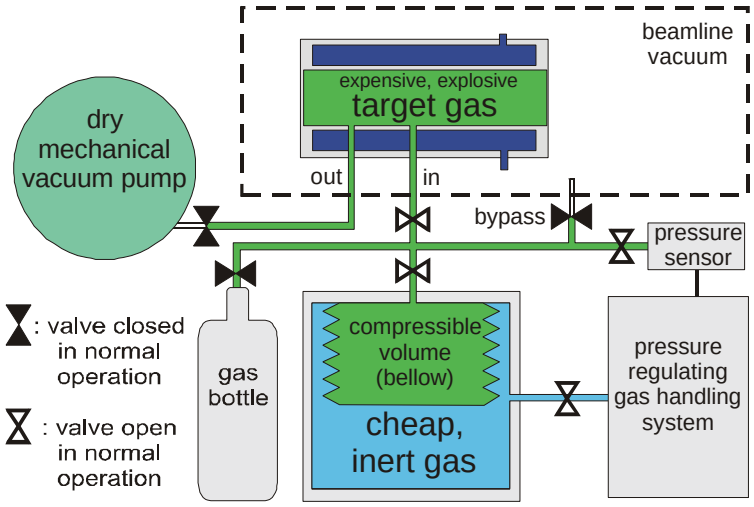

Fig. 5.9 Overview of the de-coupled gas handling- and regulation system.

A solution to the specifications mentioned above is shown in Fig. 5.9. Using a sealed metal bellow with a volume comparable to the volume of the combined gas cell and tubing is attached to the system. It is located in a bigger sealed volume, filled with a cheap inert gas, e.g. nitrogen. The pressure of this gas is controlled by a standard pressure regulating system. While controlling the pressure of the nitrogen, the pressure of the target gas is used as input of the device. This configuration automatically compensates for forces on and of the bellows.

5.2.3 Windows

Gas target windows have to fulfill a series of requirements, that often lead to conflicting design-parameters and force tradeoffs. The following is a list of desired features that need to be considered when designing a gas target window.

⇒ Minimum disturbance of the beam and the emitted particles
⇒ Reasonably large area
⇒ High tolerance to mechanical stress/pressure
⇒ High tolerance to (local) heating
⇒ High tolerance to radiation damage
⇒ Resistance to chemical reactions with the target gas

In the next section, some experiences with materials will be discussed. In section 5.2.3.2, the mounting of the windows will be described.

5.2.3.1 Material, Size and Thickness

The performance of a window under stress is partially determined by material characteristics like melting point, tensile strength and elongation, where the latter two are functions of the temperature. Equally important is the thickness of the window foil, its size and the way, it is mounted. Finally, imperfections in the production of foils and the mounting can have a major impact. Because of these many parameters, it is hard to predict, which will be the optimal material for different applications.

Parameter	maximum pressure	maximum beam power
Tensile Strength	Increasing in the elastic regime, also increased tolerance against imperfect mounting (uneven surface, unsymmetrical pre-stretch)	None
Elongation	Helpful for tolerance against imperfect mounting	None
Melting Point T_m	None	Depending on dominant mode of heat removal, up to T_m^4 dependence of maximum beam power
Heat Conduction	None	Small effect, since heat is mostly removed into target gas and via radiation
Window Size	Depending on the mode of destruction, p_{max} decreases linearly to quadraticly	None
Window Thickness	More than linear improvement through better resistance to small imperfections in material and mount	Roughly linear decrease for increased heating power due to increased energy loss; negative impact of beam quality

Table 1 Some important parameters for gas cell windows and the dependence of the tolerable gas pressure and beam power on them.

Tests were performed with different metal foils. Especially Titanium and HAVAR™, mostly a Co-Ni-Cr alloy, was found to perform well in our configuration. However, Titanium reacts chemically with hydrogen if heated, and cannot be used with this target gas. Table 1 summarizes our experience with different parameters and their impact on the performance of a gas cell target, and is intended as a guide for the choice of a material. It should be noted, that radiation damage seemed to play a lesser role than local melting of a window, at least in the case of HAVAR™.

5.2.3.2 Mounting Technique

The preferable mounting technique of the window foils onto the gas cell assembly depends on the material. It influences both window lifetime and pressure tolerance. The main difficulty with the mounting of the windows was the operation of the target at liquid nitrogen temperature. Hence the windows and their mounting had to endure the cooling and heating cycles without breaking. As shown in Fig. 5.10, the window is mounted on a stainless steel frame and the frame bolted to the cell. With 1.9 mg/cm^2 HAVAR™ windows, a pressure of 1 atm over a 1 cm diameter opening could be achieved. To seal the cell, a 1 mm diameter indium gasket was used.

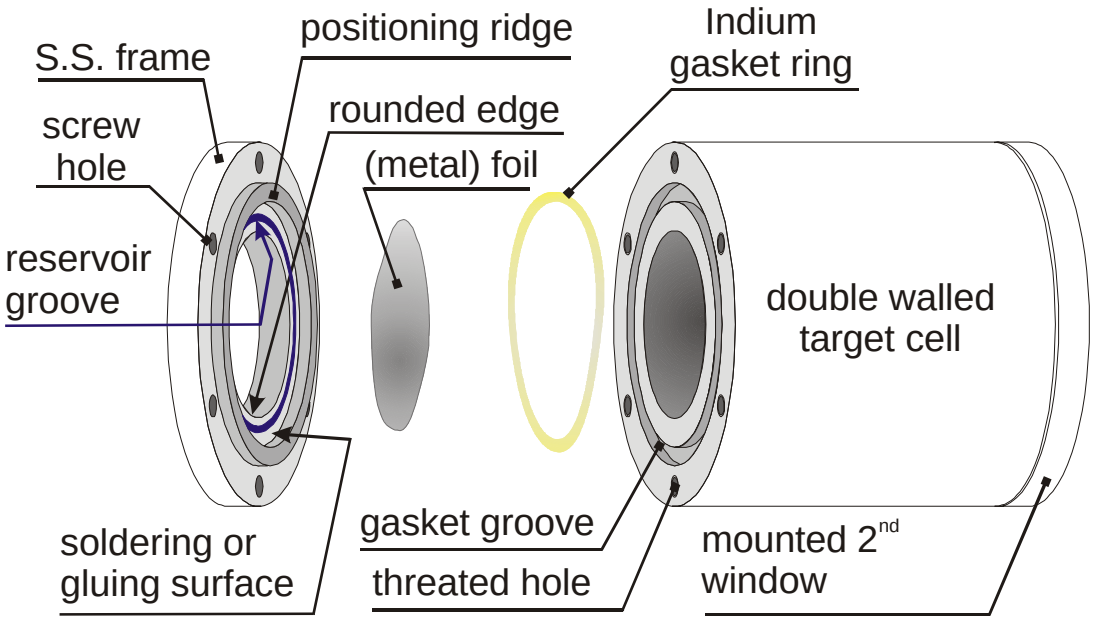

Fig. 5.10 Drawing of the window assembly of one chamber of the gas cell target

Attaching of the window foil to the frame is more problematic. Initial attempts using standard 5-minute epoxy failed, most probably due to failure of the adhesive while the cell was cooled down. For HAVAR™ foils, the following Indium soldering technique was developed[41]:

The stainless steel frame contains a small machined groove (see Fig. 5.10), which acts as a reservoir for the excess indium during the soldering process. After the frame has been thoroughly cleaned, a small amount of flux is applied to this groove using a brush. Next, a 0.5 mm diameter indium wire (99.999%, Johnson Matthey # 00155, Ward Hill, MA 01835 USA) is cut to length, fashioned into a circle, and placed into the reservoir groove. A second application of flux is brushed onto the indium wire. The HAVAR foil, cut to a diameter of 13/16 inch, is treated around the circumference with stainless steel flux. The window foil is placed centered on the mounting ring. The assembly for foil and frame is carefully placed on a small laboratory hot plate and the temperature slowly increased to 100-150 °C. The melting indium is observed to flow beneath the HAVAR foil, bonding it to the stainless steel frame. At this point another application of flux is quickly brushed around the outside edge of the foil and the temperature reduced by turning off the hot plate. When the indium sufficiently solidifies, the foil/ring assembly is removed from the hot plate for cooling. When cool, any excess flux can be rinsed off using methanol, and in some instances, mechanically removed by rubbing lightly with methanol on a cotton swab. Each window was pressure tested against one atmosphere before it was used in the experiment.

5.2.4 Gas Cell Assembly and Support System

After initial tests with a single gas-cell target, it was realized that the life span of the windows of approximately 24h required frequent re-opening of the beam-line. This was problematic not only for the time loss but also because of the contamination risk posed by the shredded, activated window-foils. Also, a slight leakage of the intact target was observed while the beam was on because hydrogen was diffusing through the heated metal foil at the beam spot. To eliminate or reduce these problems, the final production setup was designed as shown in Fig. 5.11.

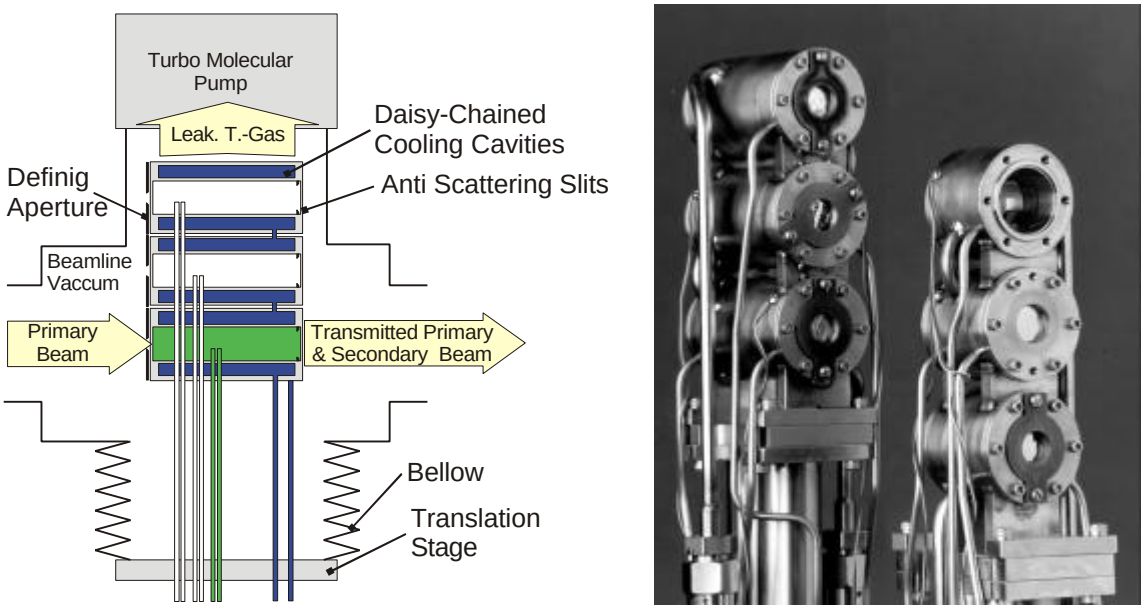

Fig. 5.11 Left: Schematic cross section of one of two cell carriers with its set of three cylindrical gas targets, mounted in a high-vacuum beam line system to produce secondary beams. A turbo pump directly above the cells improves the vacuum in the vicinity. Right: Photo of two cell carriers, one with 3.5 cm long cells, one with 7 cm cells.

Instead of only one single cell, a set of two carriers with three cells each was built. They can be moved on linear translation stages in and out of the target position. This allowed fast removal of the cells from the beam-line (e.a. for beam tuning purposes). Also, up to fife window failures could be overcome without venting the system and thus without dealing with the related time loss and contamination issues. A turbo pump above the target position absorbs a large fraction of the target gas leaking out of the cell in beam. The diffusion of hydrogen and helium through metals can be substantial, to the point where it poses a limit to the beam power. In our special configuration with an effective pumping speed of approximately 200 l/s, the pressure increased from $1 \cdot 10^{-8}$ hPa into the upper 10^{-7} hPa regime with 100 pnA beam on a H_2 cell filled with 800 hPa. As expected from the atomic masses, with a D_2 target, the leakage was smaller.

To reduce slit scattering at the window frames and to protect the stainless steel from being hit be the direct beam, each of the cells was equipped with a combination of defining aperture and anti-scattering slits. The first aperture defines the area of the cell and protects the glue or solder of the window foil from the direct beam. The second one, slightly larger, removes primary beam ions scattered off the first aperture. Not shown in Fig. 5.11 is the additional stripper foil after the cell to alter the charge state distribution of the emerging particles. A high-Z stripping material like gold decreases the average charge state while a light stripping material like carbon increases it. In the case of ^{17}F production, a maximum population of charge state 9 was desired, and therefore a $20 \mu g/cm^2$ carbon stripper foil was used.

5.3 Production Setups at ATLAS

Two different configurations were utilized to produce ^{17}F beams at ATLAS. A first, simple approach was useful to gain experience with the production, transport and tuning of a secondary beam. The second, more elaborate setup is based on the experience gained with the first configuration.

5.3.1 Initial Configuration

The gas cell was initially installed in front of the 22° bending magnet leading to the Enge split-pole spectrograph at the ATLAS accelerator (see Fig. 5.12). The angular acceptance for the secondary beam produced in the gas cell was limited to ~ 0.55° due to apertures in the beam line, thus severely reducing the transport efficiency of the ^{17}F beam. The acceptance was further reduced by the energy spread of the reaction products. For products of the d(^{16}O,^{17}F)n reaction with a 90 MeV beam on the gas cell, the total transport efficiency of the beam-line was estimated to be approximately 1% in this configuration. Including a 60% stripping efficiency into the 9^+ charge state of ^{17}F, the maximum possible transmission efficiency was expected to be 0.6%.

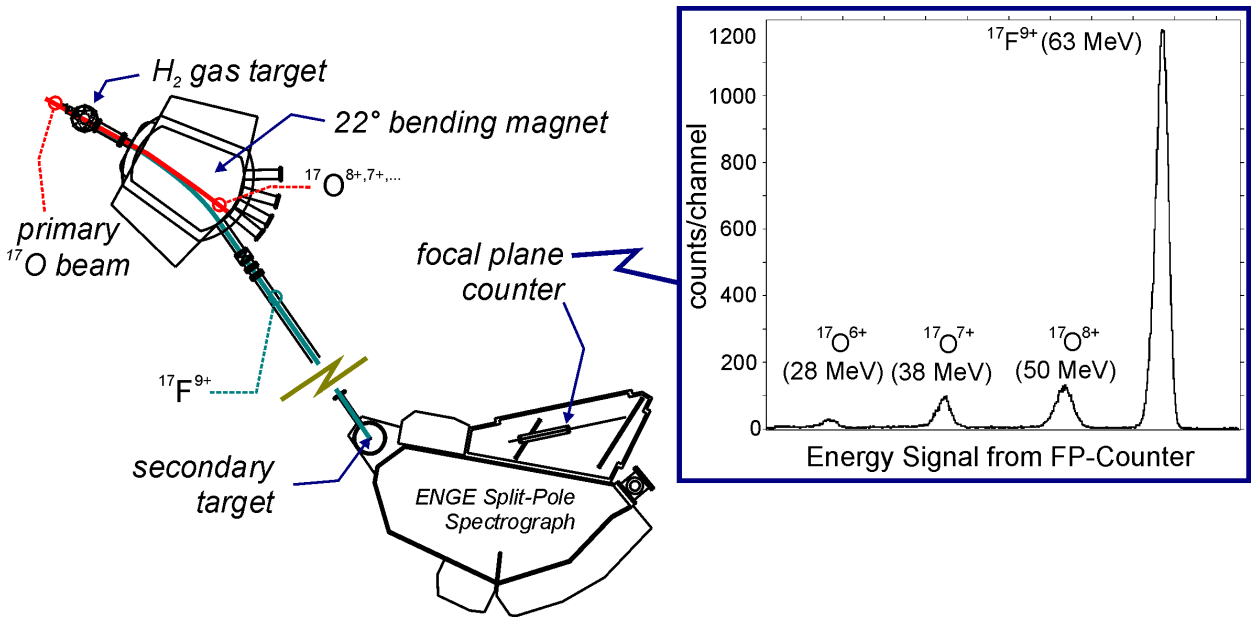

Fig. 5.12 Main: Initial production setup. Insert: Energy spectrum from the focal plane counter of the Enge split-pole spectrograph. A $^{17}F^{9+}$ beam produced with the p(^{17}O,^{17}F)n reaction and oxygen contaminants from primary beam tails with the same magnetic rigidity are clearly seen.

In this configuration[42], ^{17}F beams with energies between 55-100 MeV were produced. The d(^{16}O,^{17}F) reaction was used for ^{17}F energies below 60 MeV while the p(^{17}O,^{17}F)n reaction was preferred for secondary energies above 60 MeV. The average ^{17}F beam intensity was 700 $(s \cdot pnA)^{-1}$ and corresponded to a beam transport efficiency of approximately 0.3%. With a primary ^{16}O beam of up to 250 pnA, rates of $2 \cdot 10^5$ ^{17}F/s on the secondary target were achieved. The beam spot on the secondary target was 0.8 cm^2 in area, limited by a circular aperture. The principal contaminants of the ^{17}F beam were energy-degraded primary beam particles, i.e., ^{17}O or ^{16}O ions with the same magnetic rigidity. Their intensities varied between 10% and 50% of the total secondary beam, depending on the actual tune of the accelerator. A representative spectrum obtained with this system is shown in the insert in Fig. 5.12.

5.3.2 Improved Configuration

A new production and transport configuration used in recent experiments[43] is shown in Fig. 5.13. The production target was moved upstream by approximately 5 meters, placing it between two existing ATLAS superconducting resonators and in front of a newly installed 2.2 T superconducting solenoid. The solenoid was installed to improve the angular acceptance. It was mounted in such a way that it could be moved over a 0.63 meter distance along the beam axis. This allows optimum placement of the device for different kinematical conditions. This geometry is a compromise between the need for a sufficiently small beam envelope, as the ^{17}F particles travel through the 2.54 cm diameter collimator of the second RF-cavity, and the need to minimize the divergence of the ions so that as much secondary beam as possible can be captured and refocused by the optical elements in the spectrograph beam-line.

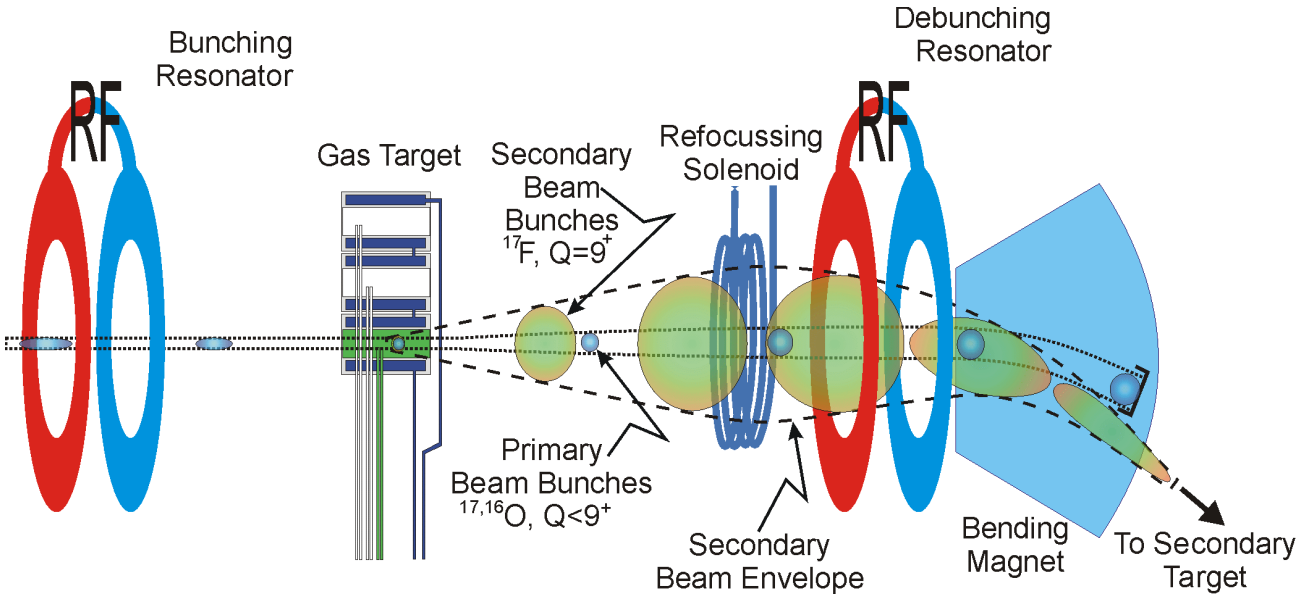

Fig. 5.13 Improved production configuration showing the impact of an added superconducting solenoid and a pair of resonators on both the primary and secondary beam bunches. While the solenoid stops the transverse growth of beam, the resonator pair reduces the energy spread of the products and moves more of them into the momentum acceptance of the bending magnet.

A superconducting "bunching" resonator located 10 m upstream from the production target was used to provide a time focus of the primary beam at the gas-cell. This minimized the longitudinal emittance of the secondary beam. The resulting strong energy-time correlation after a 3 m drift from the target to the second RF-cavity was then employed to reduce the energy spread with the second resonator. Experimentally, we found that using only the second "debunching" resonator increased the transmitted beam by about 10-20%, but that using both resonators yielded an improvement by a factor of two in beam current compared to optimization with only the superconducting solenoid. In this configuration, the total transport efficiency was measured to be 2.5%, yielding a maximum intensity of $2 \cdot 10^{6}$ ^{17}F/s on the secondary target. At the same time, the energy resolution of the beam was improved from ~1.2 MeV FWHM to better than 400 keV (Fig. 5.6). It is worth noting that this 400 keV energy spread translates into a spread of only 23 keV in the center of mass for the reaction p(^{17}F,^{14}O)α that is of astrophysics interest. The importance of achieving a time waist of the final ^{17}F energy spread is shown by the calculation presented in Fig. 5.14.

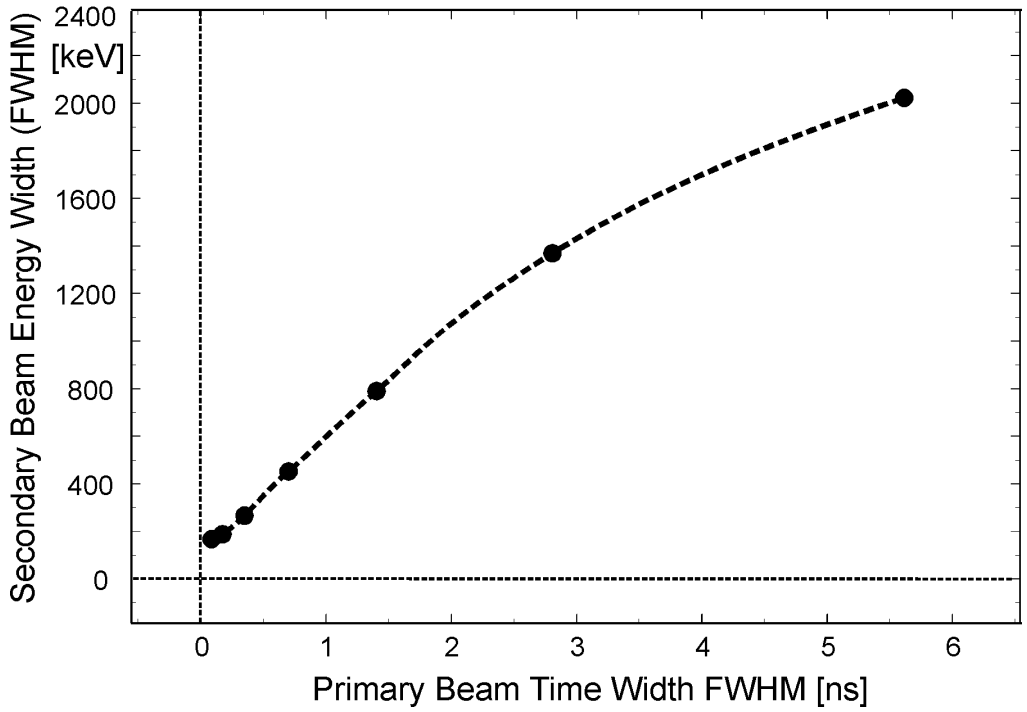

Fig. 5.14 Calculated achievable energy spread as a function of the time width of the beam pulses on the primary target. The dashed line is drawn to guide the eye.

The phase of the second RF cavity can also be adjusted to change the energy of the $^{17}F^{9+}$ beam over a range of approximately ±5 MeV, while still maintaining a small energy spread. This feature allows for the choice of production energy based partially on secondary beam yield rather than on the required secondary energy. Also, scanning excitation functions can be achieved by using the second RF cavity. This method is much faster than changing the primary energy since it involves only changes in the beam-line components after the production target.

The beam backgrounds observed in the new configuration were qualitatively different from the backgrounds in the original setup. While in some cases the primary beam leaking through was reduced well below the 10% level, products of parasitic reactions in the primary target were also observed (see Table 2).

5.3.3 Tuning

Since the process of tuning the radioactive secondary beam onto the target is non-trivial, a brief overview of the procedure used in the experiments is given here. In a first step, a weak primary beam (e.g. $^{16}O^{8+}$) transmitted through the gas target was tuned to the secondary target position. The small-angle straggling caused a considerable divergence, allowing to optimize the setting of the focusing beam-line components (solenoid and quadrupole doublets) in a configuration similar to that required for the transport of $^{17}F^{9+}$.

In the second step, all magnetic elements after the primary target were scaled from the magnetic rigidity $Br = p/Q$ of the primary beam (e.g. $^{16}O^{8+}$ at 70 MeV) to the rigidity of the secondary beam (e.g. $^{17}F^{9+}$ at 65 MeV). The primary beam intensity was then increased to a production current of ~100 pnA and a 1:1000 attenuator was inserted after the 22° bending magnet. The latter step reduced the expected ^{17}F rate on the secondary target to ~10^3 pps, allowing the use of the focal plane counter in the split pole spectrograph positioned at 0° to directly analyze the beam

with respect to mass, Z and energy. The ^{17}F yield measured at the focal plane was subsequently optimized by fine tuning the various elements of the BTS. For this purpose, the output of the energy amplifier and the same signal digitized with a custom built multi-channel analyzer were passed to the accelerator control room. It should be noted that the increased beam current in the final step of tuning is crucial. Heating effects change the effective target density on the beam axis and thereby alter $S(E)$.

5.4 Other Beams

^{17}F was the first short-lived beam produced and successfully used in physics experiments[43,44] at ATLAS. Later on, beams of ^{21}Na and ^{25}Al have been developed as well. Initial tests with (d,n) and (p,n) reactions were conducted and the results agreed with the expectations. A brief overview of the results is shown in Table 2.

Beam	*Production Reaction*	*Secondary Energy ± HWHM [MeV]*	*Intensity (pps per pnA primary beam)*	*Backgrounds (fract. of total beam [%])*
^{25}Al	^{24}Mg(d,n)^{25}Al	204 ± 0.8	$1\cdot10^3$	^{24}Mg(50) ^{25}Mg(< 1)
^{25}Al	^{25}Mg(p,n)^{25}Al	180 ± 1.5	$2\cdot10^3$	^{25}Mg(20) ^{24}Mg(< 1)
^{21}Na	^{20}Ne(d,n)^{21}Na	113 ± 0.5	$4\cdot10^3$	^{20}Ne(50) ^{21}Ne(< 0.1) ^{18}F(< 0.1)
^{21}Na	^{21}Ne(p,n)^{21}Na	113 ± 0.3	$8\cdot10^3$	^{21}Ne (40) ^{20}Ne (< 0.1)
^{17}F	d(^{16}O,^{17}F)n	40-65 ± 0.2	$2\cdot10^4$ (intensity achieved $2\cdot10^6$)	^{17}O(10) ^{16}O(10-30)
^{17}F	p(^{17}O,^{17}F)n	60-110 ± 0.2	$2\cdot10^4$ (intensity achieved $2\cdot10^6$)	^{17}O(10-30) ^{14}N(2)

Table 2 Overview: Beams produced using the in-flight technique at ALTAS.

The technique for producing beams of short-lived nuclei described here can be applied to many other isotopes. In the mass range below ^{56}Ni, there are more than 50 radioactive beams that can be produced by (p,n), (d,n) or (p,d) reactions. The secondary beam intensities depend on the parameters discussed above and on the efficiency of the mechanism to separate the primary from the secondary beam. The available primary beam intensity and the ability of the primary target to withstand thermal and radiation stresses pose specific technical limits. For light elements ($Z \leq 10$), the gas cell target can withstand currents in excess of 100 pnA. However, the increasing energy loss for heavier primary beams will become a limiting factor for the secondary beam intensities that can be achieved. A possible improvement is the use of windowless gas targets. An alternative mechanism to separate the primary and secondary beams is the use of a shadow bar as described in an article[32] from J.J. Kolata. Such a device in combination with the selection of the magnetic rigidity $B\rho$ should provide cleaner secondary beams, especially in systems with higher nuclear charge Z.

6 Experiments with ^{17}F Beams

Three physics experiments were performed with the ^{17}F beams described in the previous chapter. The first experiment, a fusion-fission study[44] on ^{208}Pb was the first successful measurement employing a ^{17}F beam. The second experiment[43] was designed to measure the ^{17}F(p,α) reaction. The third one was an extended version of the second experiment, capable of simultaneously measuring ^{17}F(p,p), ^{17}F(p,α) and ^{17}F(p,p'). The data from the last two experiments form the physics basis of this thesis as they delivered information on levels in ^{18}Ne. All experiments were set up in front of the Enge-split-pole spectrograph, that was always required to tune and monitor the beam. It also provided a measurement of the secondary beam energy.

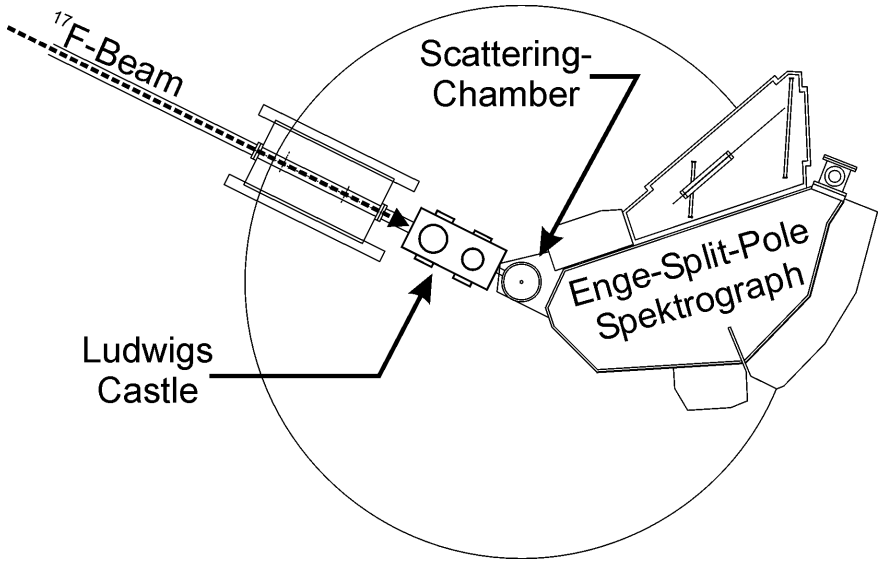

Fig. 6.1 Overview of the experimental configuration of the ^{17}F-experiments. The detectors were either located in the spectrograph scattering chamber or in a dedicated scattering chamber, called "Ludwigs Castle". The spectrograph served for tuning and monitoring purposes.

6.1 Fusion-Fission Experiment

In a semi-classical picture, low binding energies lead to large radii of single particle orbits in nuclei. ^{17}F with its magic ^{16}O core and a single proton bound by only 600 keV seems to be a good example. However, the $d_{5/2}$ ground state wave function does not favor large radii. In contrast, the first and only excited state of ^{17}F has a $s_{1/2}$ configuration and is bound by only 100 keV, making it an ideal candidate for a proton halo state[45]. Since the ground state and the first exited stated are connected[46] by a large *B*(E2) value (66.4 b^2), a certain fraction of the ^{17}F-nuclei incident on a heavy target ion will be Coulomb-excited to this state before the fusion reaction. In this case, increased break-up probability and a larger average radius could result in a considerable increase of the fusion cross-sections. To study this effect, a measurement of the fusion-fission reaction ^{208}Pb(^{17}F,f) was carried out and compared to a measurement of ^{208}Pb(^{19}F,f) with the same setup

The beam for this experiment was produced with the simple scheme discussed in chapter 5.3.1, which limited the maximum ^{17}F-current on target to 2x10^5 ^{17}F/s. This was sufficient to measure fusion-fission cross-sections down to ~1mb.

The setup which had a detection efficiency of 7.8% is shown in Fig. 6.2. Four Si-detectors, each segmented in four quadrants, were arranged around the target in the scattering chamber of the ATLAS Enge split-pole spectrograph. The coincident detection of two particles with about 100 MeV (E ~ 1 MeV/A) each in two opposing detectors is a sufficient signature for the fusion/fission reaction.

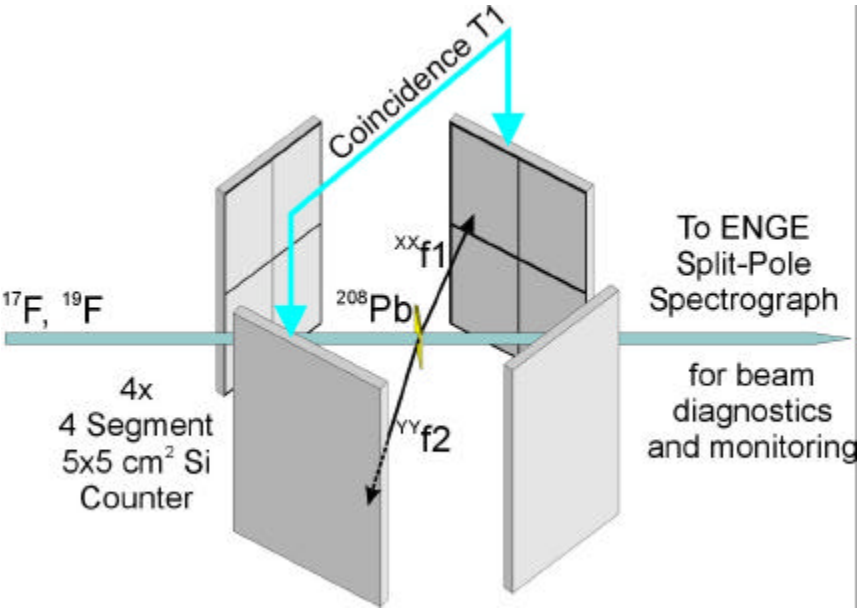

Fig. 6.2 The setup used for the $^{208}Pb(^{17,19}F,ff)$ experiment.

The results can be summarized as follows: no fusion enhancement was observed. Fig. 6.3b shows that the $^{208}Pb(^{17}F,f)$ reaction behaves at energies above 0.95 times the Coulomb-barrier like the $^{208}Pb(^{19}F,f)$ reaction, if one corrects for the different radii with an $R \sim A^{1/3}$ - law. On the other hand, Fig. 6.3a shows that $^{208}Pb(^{17}F,f)$ behaves over the full measured energy range in good approximation as $^{208}Pb(^{16}O,f)$, if one corrects for the different nuclear charge by multiplying the cross-section by 8/9.

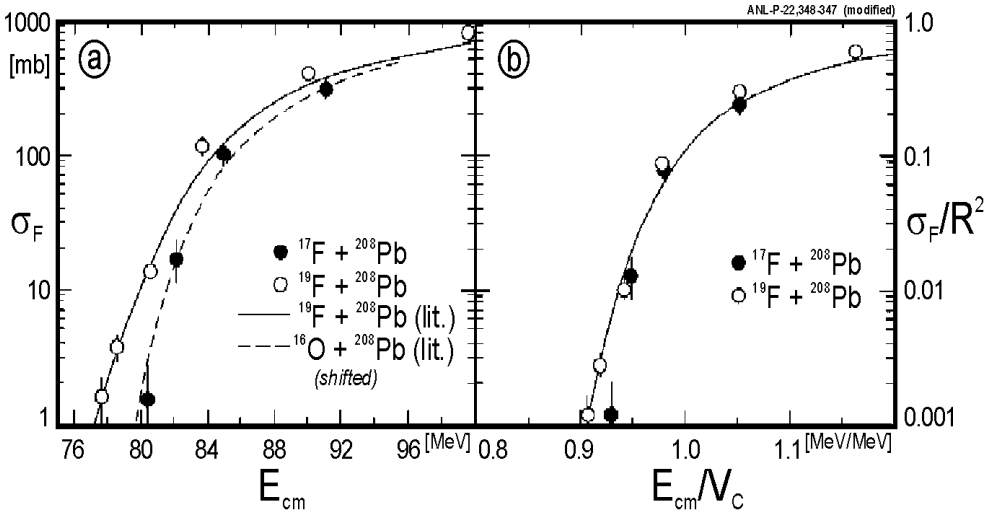

Fig. 6.3 $^{208}Pb(^{17}F,f)$ cross-sections compared to $^{208}Pb(^{19}F,f)$ data from this measurement and the literature[47,48]. a: cross-sections as a function of E_{cm}. b: normalized cross-sections (σ/R^2) as a function of E/V_C.

6.2 Ludwig[49] II

After first test runs[50], in which a magnetic spectrograph was used to detect the heavy reaction product, it became clear that a setup with considerably higher detection efficiency was needed. In order to clearly identify the reaction products from the p(^{17}F,^{14}O)α-reaction, a coincidence requirement together with a gate on the total energy of the beam was used. The experiments with the spectrograph had shown that this was sufficient to suppress the oxygen-induced background because of its lower energy. As shown in Fig. 6.4, one 300 µm thick Si-detector detected the α-particle and the other the ^{14}O-particle. Both detectors were 16-fold segmented in wedges, allowing the measurement of the azimuthal angle f within 22.5°. This provided an additional coincidence condition from the coplanarity of the reaction products.

The maximum angle q_{max} for the reaction products is given by the kinematic limit plus a minor contribution from both small angle scattering in the target and angle of the incoming beam particle. For the alpha particles, q_{max} is, depending on the reaction energy, in the order of 20° and for the ^{14}O-particle about 6°. The polar angle resolution of the detectors was provided by their segmentation into 16 rings each, resulting in a theoretical angle resolution of 0.75° for the backward detector 1 and 0.25° for the forward detector 2. However, because of the 5x5 mm size of the beam-spot, the measured resolution was 2.5° and 0.8°, respectively.

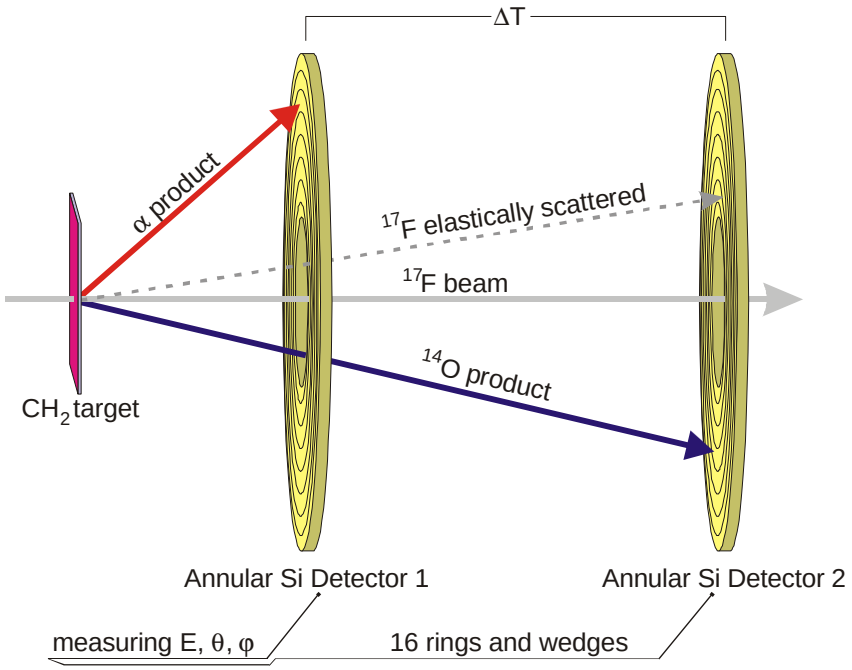

Fig. 6.4 Ludwig II, the first high efficiency setup used to measure the ^{17}F(p,α) reaction in inverse kinematics.

At the energies used, this setup had a detection efficiency of 50% to 65% for the ^{17}F(p,α)-reaction, covering center-of-mass angles between q_{CM} ~ 30°-130°. To illustrate the detection scheme, the two most important spectra are given in Fig. 6.5. Fig. 6.5a shows the energy detected in detector 1 plotted against the energy measured in detector 2. The total energy $E = E_a + E_{14O}$ is a constant given by the Q-Value and the beam energy with only minor corrections due to target effects. Since the Q-value is only -1.19 MeV, this constant is essentially the beam energy, indicated by the solid line. Since products from reactions induced by the oxygen beam

contaminations had significantly lower energies, all oxygen induced backgrounds, no matter of what nature, fall well below this line. The events in the vicinity of the line are particles originating from transfer reactions between ^{12}C and ^{17}F and are responsible for the small background in the p,α-data. However, most of these events do not fall on the required kinematic curve of $q_a(E_a)$.

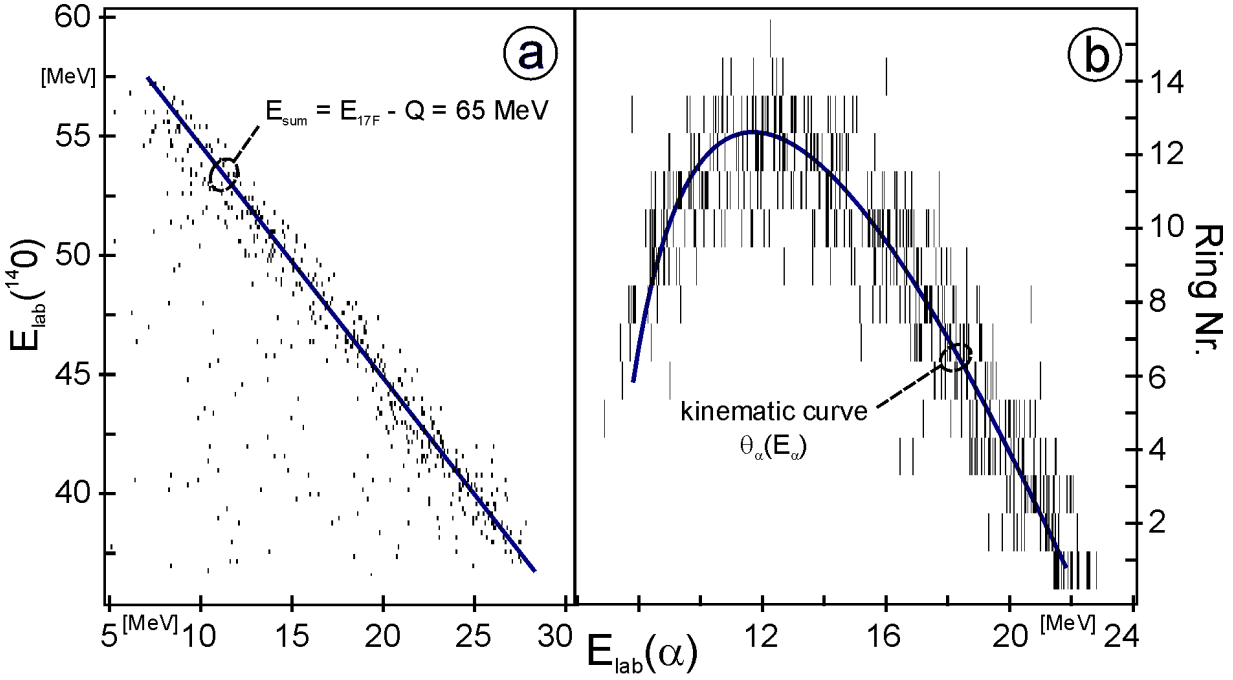

Fig. 6.5 **a) Energies of coincident α and ^{14}O particles. The coplanarity condition has been applied. b) A two-dimensional scatter plot of α-particle angle (ring number) vs. α energy for the events from a), requiring also the correct sum energy. The solid lines represent the ideal E_a-E_{14O} and q_a-E_a correlations, respectively, for events originating from the mid-point of the target.**

Fig. 6.5b shows a plot of ring number versus alpha-energy for events in the α-detector gated with the sum-energy requirement from Fig. 6.5a. Since q_a is roughly proportional to the strip number, α-particles from p(^{17}F,α) fall on a kinematic parabola. It should be noted that the apparent poor resolution is mostly due to the beam spot size, the small-angle scattering of the particles in the target and the energy width of the beam. In Fig. 6.5b, the finite angle resolution gives rise to additional widening of the distribution around the kinematic parabola. The energy resolution measured with alphas from a ^{227}Th-source was on the order of 100 keV.

6.3 Super Ludwig

For the reasons discussed in Chapter 4, the Ludwig II setup was improved by adding capabilities to measure simultaneously $^{17}F(p,\alpha)^{14}O$, $^{17}F(p,p)^{17}F$ and $^{17}F(p,p')^{17}F^*$ in inverse kinematics. The requirements on the setup were the following:

- Large Detection efficiency for p(^{17}F, α)^{14}O
- Discrimination between p(^{17}F, α)^{14}O, p(^{17}F,p)^{17}F and p(^{17}F,p')$^{17}F^*$
- Suppression of backgrounds from ^{16}O or ^{17}O in the beam
- Sufficient angular resolution for the light particle to measure angular distributions

Since the use of the annular Si-Detectors for the detection of the light particles had been successful, this technique was retained and the system was extended to cover more backward angles in the laboratory. The downside of this approach was that, because of their long range, scattered protons could only be stopped at large laboratory angles. For these processes, a simple sum energy gate described for Ludwig II could not be applied, and a discrimination based on the nuclear charge Z of the heavy particle was required. The setup used is shown schematically in Fig. 6.6.

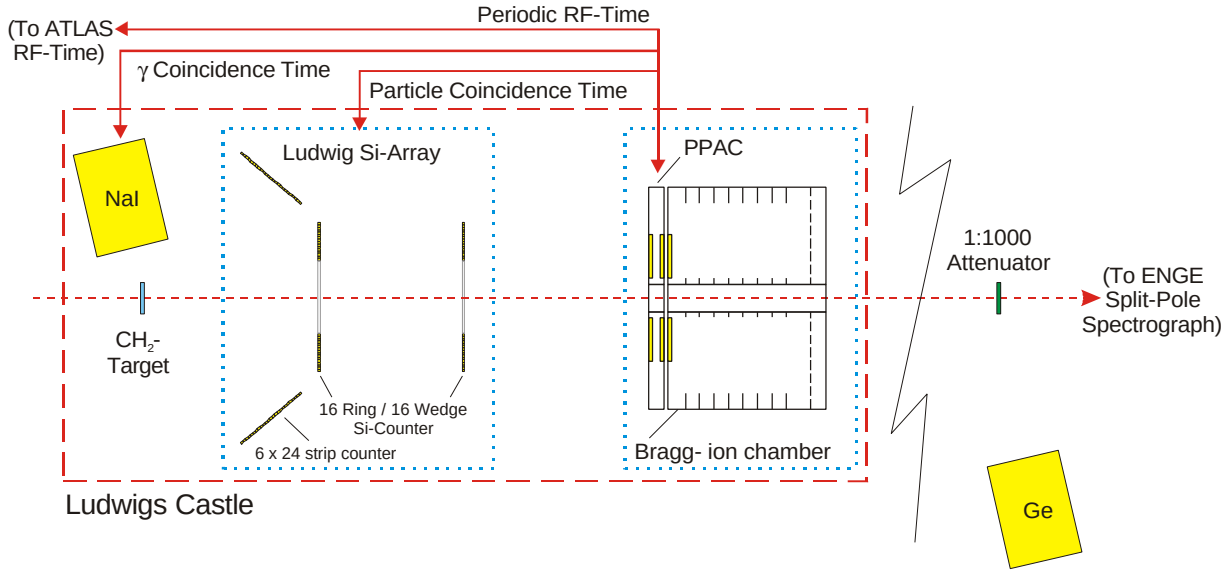

Fig. 6.6 Overview of the "Super Ludwig" setup as used in the experiment of November 1999.

The basic idea to do a coincidence experiment was carried over from the first setup. However, the nuclear charge of the heavy ion (forward) particle was measured in a newly built Bragg-type ion-chamber[51] and a PPAC. The Silicon array, now consisting of two annular counters and six 5x5cm 24-strip paddles, took the place of the backward annular counter in the old setup. As additional information, the time of arrival of the heavy particle (PPAC) with respect to the RF-Signal from the ATLAS linear accelerator system was now measured. A Ge-detector was added as beam monitor. It counted 511γ-quanta that resulted from the β^+ decay of the ^{17}F beam stopped on a 1:1000 attenuator after the detectors. This attenuator, located in the target ladder of the spectrograph scattering chamber, allowed to monitor the incoming ^{17}F-beam with the spectrograph set at 0°. As an absolute measurement of the incoming ^{17}F-beam intensity, the elastic scattering $^{12}C(^{17}F,^{17}F)^{12}C$ off the CH_2 target measured in the Bragg-counter was used.

Finally, the design included a NaI-Szintillator to measure coincident γ-quanta from the γ-decay of the excited $^{17}F^*$ produced in the target via $p(^{17}F,^{17}F^*)p'$. It was intended to identify inelastic proton scattering events at angles where a kinematic separation was not possible. However, its low efficiency together with less than expected beam in the last experiment did not allow the use of this feature.

6.3.1 The Bragg-Counter and PPAC

The decision to use a Bragg-type ion chamber for the detection of the heavy reaction product was driven by the need for Z-identification. The ion chamber could not be very deep (15 cm were the absolute limit) and required an opening at 0° to allow the direct beam through. Finally, it had to provide a good timing and energy signal.

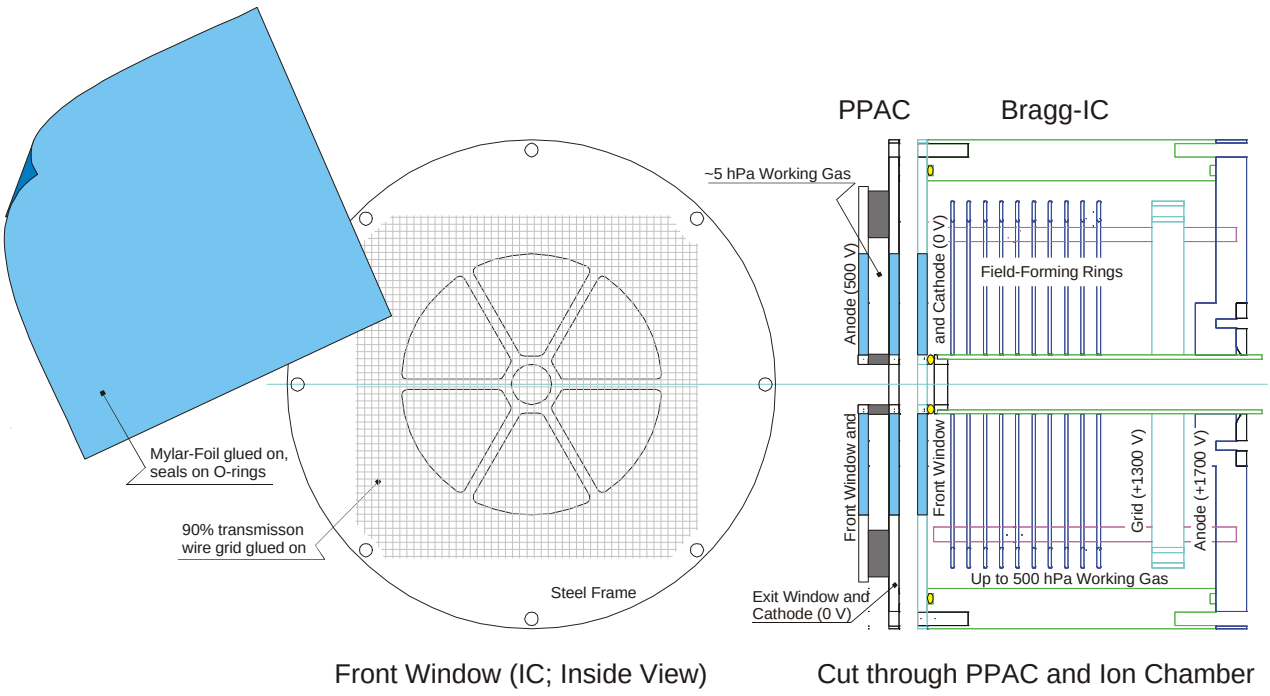

Fig. 6.7 The Bragg-ion-chamber assembly with PPAC in cross-section and a scematic drawing the ion chambers pressure window.

On the right part of Fig. 6.7, a schematic of the detector system is shown, indicating the major components. The pressure window which serves also as cathode, has to withstand a pressure of up to 500 hPa without significant distortions. For this, a 90% transmission support grid was glued on the stainless steel window frame, and a Mylar foil was stretched over the grid at the same time. The window was sealed directly on the Mylar foil with O-rings at the inner tube and the chamber wall.

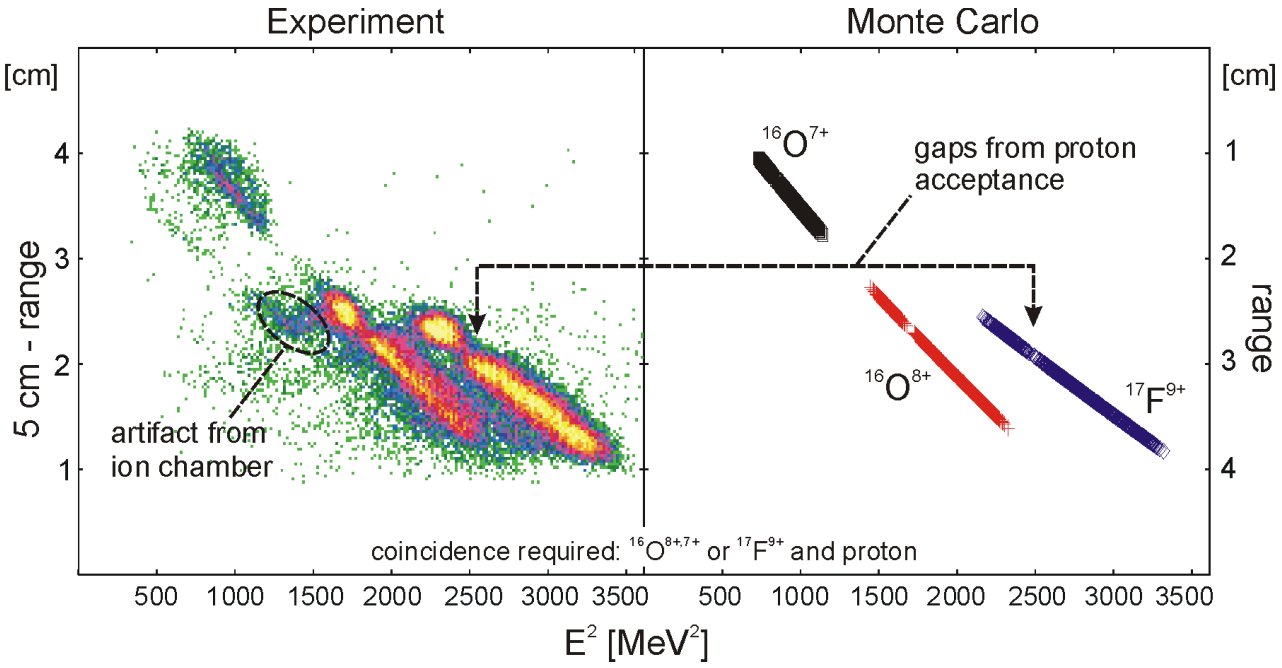

Fig. 6.8 Experimental- and simulated data from the annular Bargg chamber.

The PPAC in front of the ion chamber provided the time signal for the coincidence as well as the start signal for measuring the range in the Bragg counter. It was designed as a completely independent detector with an entrance- and an exit window, serving also as electrodes. The shape of the windows was identical to the window of the ion chamber, but since the working pressure was well below 10 hPa, no grid was needed to support the aluminized Mylar foils.

The energy resolution of the ion chamber was of the order of 2%, depending on the range and energy of the particles. The *Z*-separation achieved was sufficient to separate ^{17}F and ^{16}O. Plots of E^2 vs. range for elastic scattering of protons from the ^{17}F and ^{16}O beams are shown in Fig. 6.8. The experimental data (left) also include contaminations from background reactions. Three groups of particles are identified. The gaps in the ^{17}F and $^{16}O^{8+}$ groups are caused by the gap in the q_{lab}-acceptance of the Silicon-detector-array for protons. The marked satellites in the data originate from imperfections in the detector window. On the right side of Fig. 6.8, a simulation of this configuration is shown, calculated under the assumption of ideal energy resolution in the ion chamber and isotropic elastic proton scattering. The Monte Carlo code used will be discussed in section 6.4.

6.3.2 The TOF-RF Information.

The measurement of the time of flight of a particle at the PPAC with respect to the accelerator RF-signal turned out to be an important signal for particle identification.

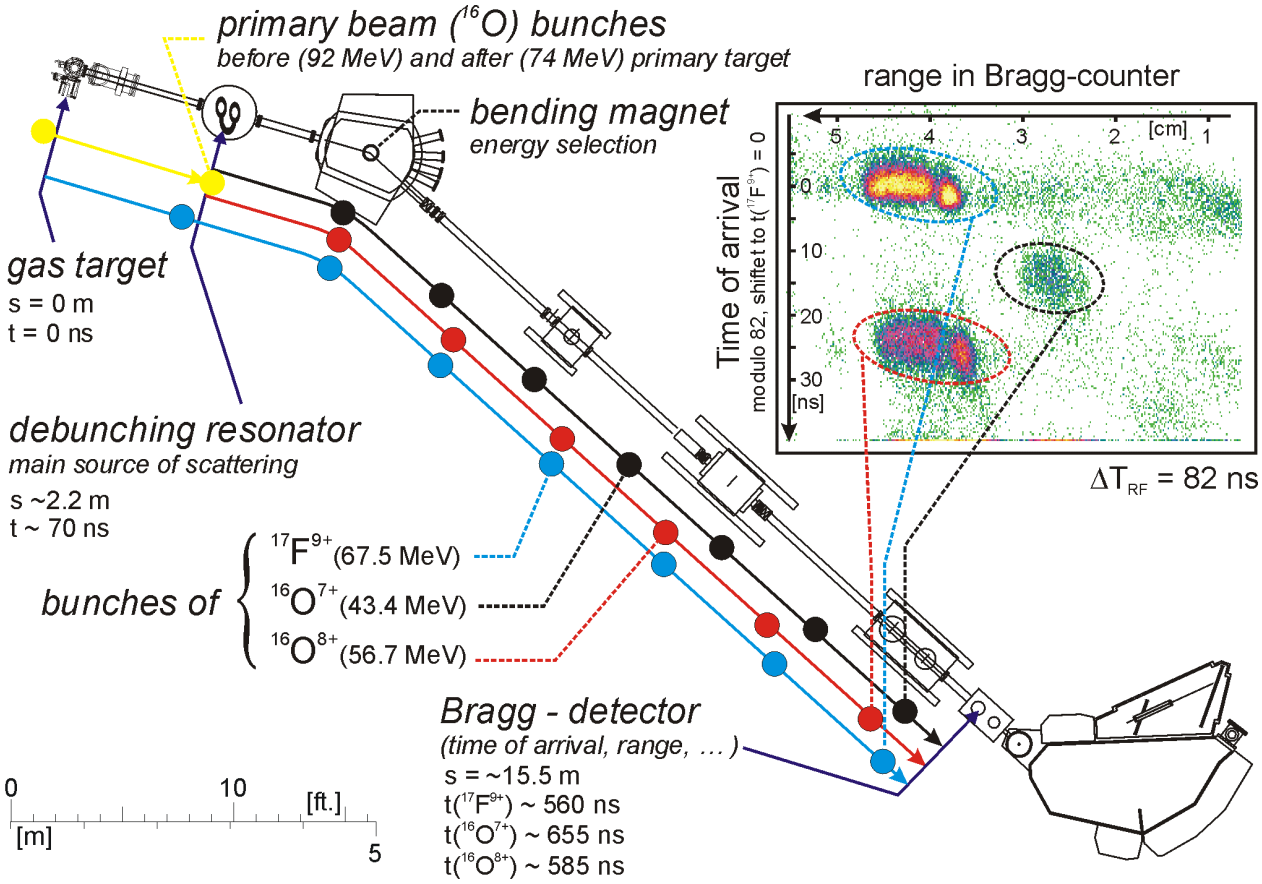

Fig. 6.9 The time of flight measured with respect to the ATLAS linear accelerator RF plotted vs. the range of the particle in the Bragg counter.

The time of arrival of both $^{16}O^{8+}$ and the $^{16}O^{7+}$ at the secondary target differed by 15-30 ns from the time of arrival of $^{17}F^{9+}$. Since for the 16 m long flight path, the beam bunches of $^{17}F^{9+}$ and $^{16}O^{8+,7+}$-ions widen and overtake each other, this cannot automatically be expected. It should be mentioned that the flight time differences of heavy particles from different reactions in the secondary target to the PPAC are of the same order as the time differences caused by the energy spread of the beam.

To illustrate this in more detail, Fig. 6.9 shows the floor plan of the transport system from the primary to the secondary target. Also shown are the location of bunches of the primary beam and secondary ^{17}F beam along the beam-line at an arbitrary moment in time. In addition, bunches of energy-degraded primary beam are shown, originating mostly from scattering at the collimator of the debunching resonator or its heat shield. As an inlay, a plot of the RF-time of arrival (modulo 82, the time between two bunches at ATLAS is 82 ns) vs. range in the Bragg-counter is provided. For Si-Bragg-detector coincidences, one clearly makes out three groups. By gating with e.g. E^2-Range (Fig. 6.8), one identifies them with ^{17}F-induced particles, $^{16}O^{7+}$ induced particles and $^{16}O^{8+}$ induced particles. Inversely, this classification allows the identification of the debuncher as main source of scattering by simulating the flight times of the various groups.

Using the TOF-Range spectra as a particle gate, ^{14}O-particles appear in the ^{17}F-group, since they are ^{17}F-induced. This allowed to clearly identify the $^{17}F(p,\alpha)^{14}O$ reaction, since the ^{14}O has to fall into the ^{17}F-group in this spectrum, and into the oxygen group in, for example, the E^2 versus range plot.

6.3.3 The Si-Array

The heart of the setup is a large array of Silicon strip- and annual detectors with a total of 94 channels. A view onto the setup from the vicinity of the target along the beam axis is shown in Fig. 6.10, left side.

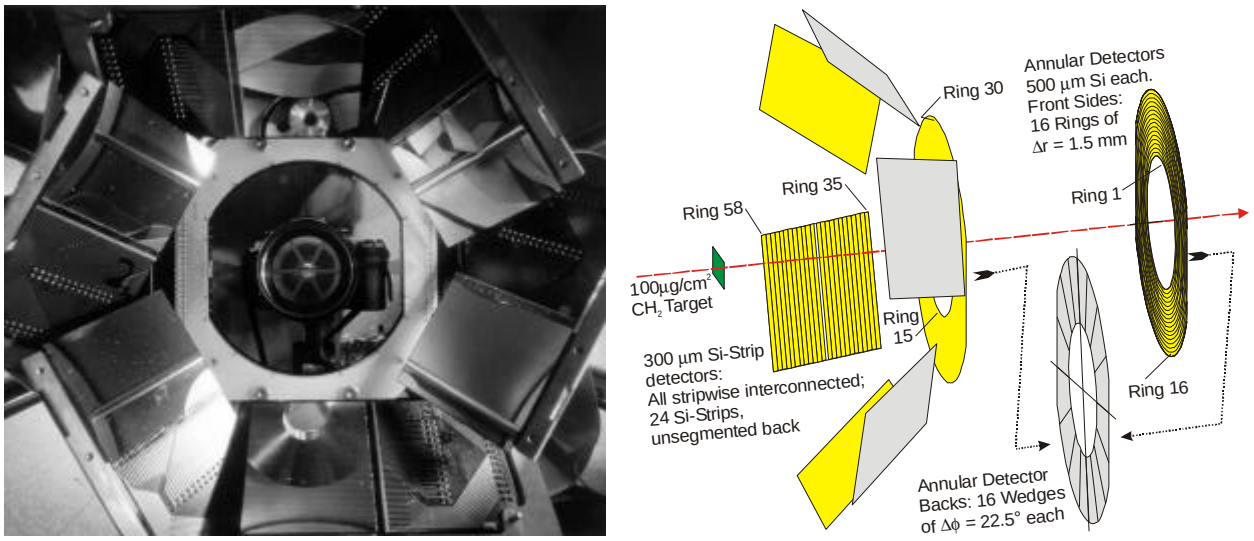

Fig. 6.10 Left: Photo from the vicinity of the target position. The second annular detector is not visible from here. Through the hole, the entrance window of the PPAC can be identified. Right: Schematic view of the Silicon-detectors.

The right side of the figure gives a schematic of the silicon-detector array. The segmentation, as indicated, is chosen for good theta resolution. To minimize the number of electronics channels, six 24-strip counters were strip-wise connected and read out as “hexagonal rings”. In the data

analysis, the strips were numbered from 1 (central ring of the forward annular detector) to the outer pseudo-ring on of the six paddles. To better relate ring numbers to laboratory angles, the numbers 15 and 16 were used twice (same angle from the target center), and the numbers 31 through 34 were not used. This choice was taken in order to represent in the spectra the physical gap in q_{lab}-acceptance between 24° and 32°.

To identify individual reaction channels the spectra shown in Fig. 6.11 were used. A Monte Carlo calculation for the expected ^{17}F induced particle groups (right) and measured data, gated by $^{17}F^{9+}$ and the particle sum energy (left) were compared. The simulation indicates, that there is no clear discrimination of the elastic and inelastic proton groups for angles $q_{lab} < 50°$. The punch-through of the protons at different angles causes intersections of the lines of the elastic and inelastic groups. The p(^{17}F,p)^{17}F reaction is represented by the dominant line between ring 21 and 58. From strip 52 on downwards, the inelastic scattering p(^{17}F,p')$^{17}F^{495}$ mix with the stronger (p,p)-group, and will be discussed later. The α-particles show the expected kinematic behavior.

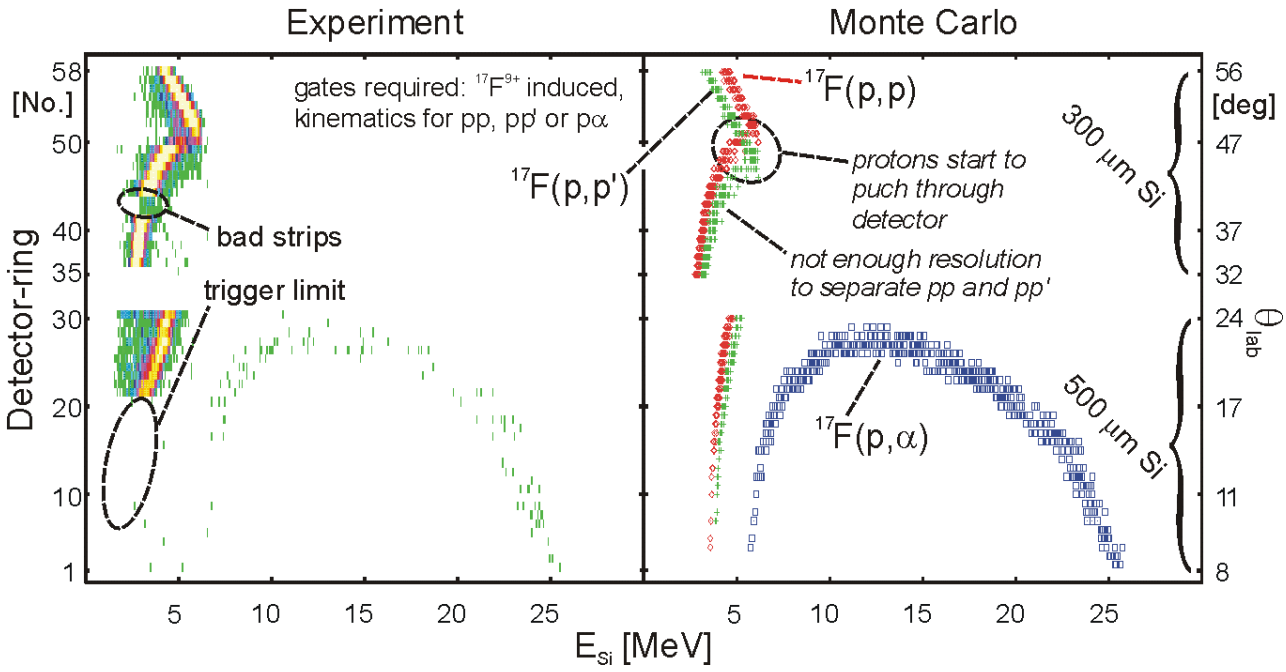

Fig. 6.11 Measured (left) and simulated (right) data in the Si-array. The ^{17}F-induced processes p(^{17}F,p), p($^{17}F^{*}$,p') and p(^{17}F,α) with their respective event groups are shown.

6.3.4 Energy versus Energy

The use of the sum energy of the light and the heavy particle (see Fig. 6.5) as a condition to discriminate the ^{17}F(p,p) or ^{17}F(p,p') processes against elastic scattering of ^{16}O(p,p) is not possible by simply using the beam-energy and Q-value as a measured quantity. The punching-through problematic of the protons at forward angles makes it impossible to directly measure the total energy of the event. However, additional information can be derived from the spectrum plotting the two energy signals E_{Si} versus E_{Bragg} and comparing them with a Monte Carlo simulation of the same spectrum (see Fig. 6.12).

As in the Ludwig II setup, the ^{17}F(p,α) reaction can be separated from oxygen-induced background processes by the sum energy of the ^{14}O-particle and the α-particles. Ambiguities in the identification of the α-particles exist only with protons scattered off ^{17}F, which, however, have

very different scattering angles. The signal of the heavy ion in the Bragg-counter showed some non-linearities. Signals from particles that were stopped far from the anode suffered from recombination losses, which lead to curvatures in the E_{Si}-E_{Bragg} curves, especially for low energy signals. This effect did not severely impact the ability to use the $E_{Si} - E_{Bragg}$ spectrum to discriminate proton scattering off ^{17}F from the scattering off ^{16}O. The two proton groups that overlap in this spectrum (see Fig. 6.12 right) fall into very different laboratory angle regions.

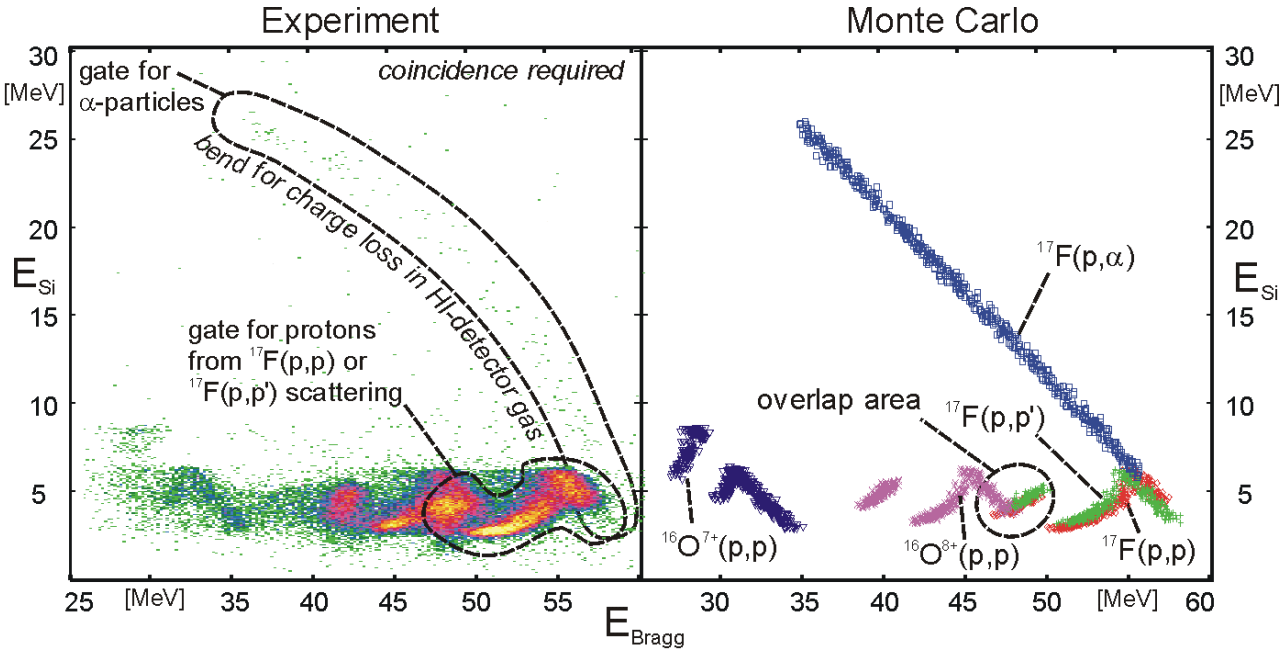

Fig. 6.12 A plot of energy measured in the Si-array versus energy measured in the Bragg-counter. The curvature in the experimental data is caused by recombination effects in the detector.

6.4 Universal 3D-Montecarlo Package

The interaction of ions with matter plays an important role in this thesis, both to model the particle distributions from the production target and the spectra observed in the experimental setup. A set of tools for Monte Carlo simulations was developed, that can tackle both problems. It consists of two independent programs and a set of minor tools.

`Source` simulates an extended (production) target for reactions in two-body kinematics or a radioactive source. An extension for three-body processes or reactions with subsequent decay is possible. However, the code does not allow different processes in one run, i.e. each event represents a reaction or decay of the one specific type. To simulate separate reactions, the processes are treated independently in different runs and are added later. The model target consists of three layers. From these, the first and last layer act as dead layers. In the dead layers, particles loose energy according to energy-loss-tables[38] and undergo small-angle scattering[52] as well as energy straggling[53]. In the 2nd or reaction layer, particles are created according to an excitation function and an angular distribution. The algorithm first determines the interaction depth in the reaction layer. The stopping power dE/ds of the particle and the ds/dE are folded to a ds/ds where s denotes the length of the path traveled in the reaction layer. A length s_{react} on the path of the projectile ion, at which the reaction occurs, is randomly chosen, using the ds/ds as a weight. The

path through the middle layer to the interaction point and the path of the outgoing products are treated like two additional dead layers.

The program is controlled by an input file defining the reaction, ds/dE, the target materials and the geometric dimensions. Q-values can be given relative to an internal database. In addition, optional files for an angular distribution ds/dW and the starting energy distribution of the projectile particles can be supplied. By command line arguments, beam parameters, the desired number of events and the desired output quantities are defined. The output is a table providing on request the following quantities for the produced particles: E, q, f, E_{born}, q_{born}, f_{born}, $q_{cm,born}$, velocity, mass, nuclear charge, charge state, time of flight and position. The parameter with the index "born" indicates that the values at the moment of creation without any further target interaction are provided. There are also special parameters, that provide the data in the correct input format for the second program of the Monte Carlo set, `Detectors`.

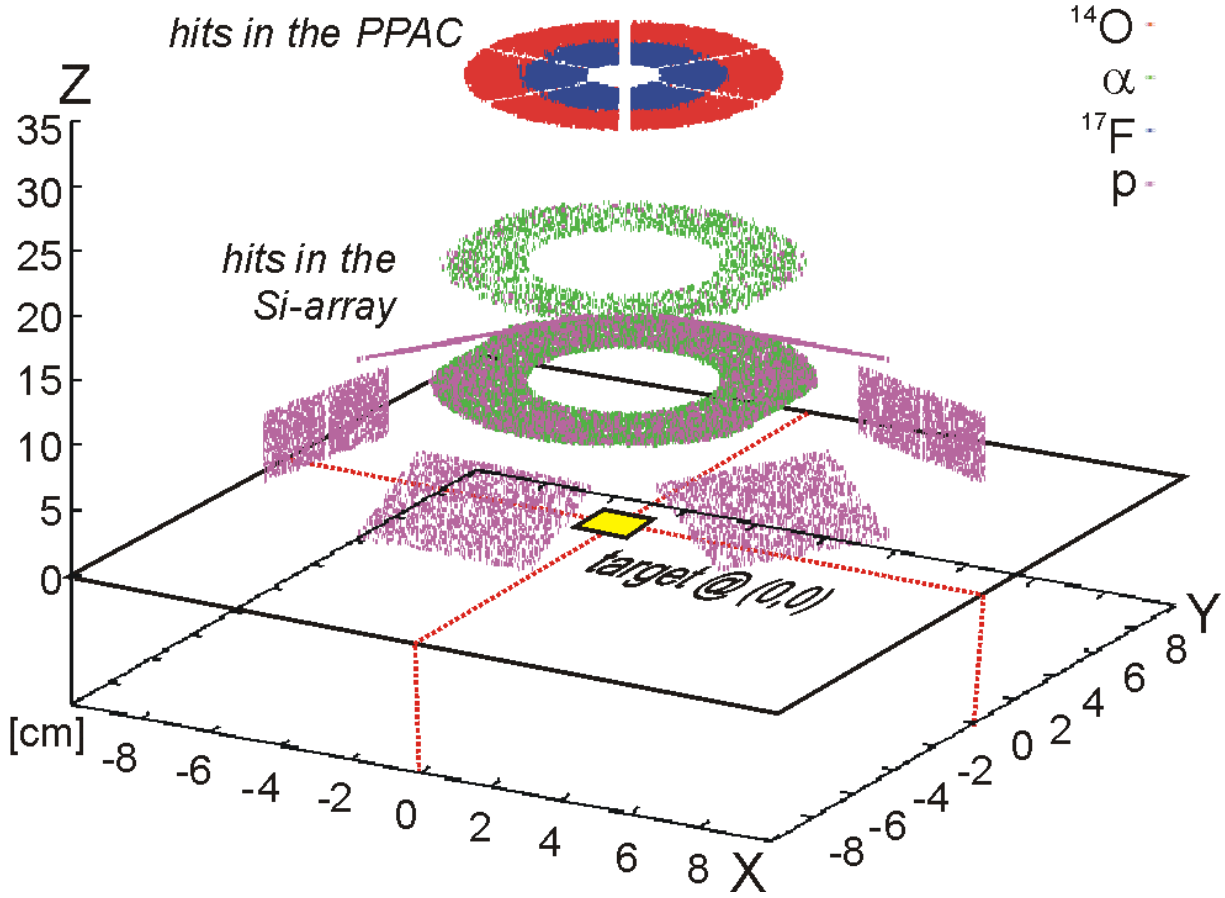

Fig. 6.13 Hits in the Super Ludwig setup simulated for the ^{17}F-induced processes p(^{17}F,p) and p(^{17}F,α), assuming the target in the (0,0)-position and a 65 MeV ^{17}F beam. The shape of the PPAC entrance window and of the Si-detectors is visible. The gap in the middle of the strip detectors originates from the read-out system of the experiment.

`Detectors` allows the definition of any number of detectors in the three dimensional space around the target. Annular ring detectors, standard circular detectors or rectangular strip detectors with any number of layers can be created. This allows the simulation of dead layers, windows and *DE-E* telescopes.

For each particle hit, the following values are provided: time-of arrival, position, hit-detector- and strip. For each target layer, the energy loss, the maximum *dE*/*dx* and the range in a layer can be calculated. In addition, all data provided by `Source` can be passed through to the output of `Detectors`. This information is sufficient to produce a three-dimensional hit pattern, to simulate a telescope or a Bragg-counter and to treat effects of dead layers. Especially, the punch-through of particles can be simulated and a first-order approximation of a magnetic spectrograph is feasible with the help of some external scripts. However, some limitations exist. A particle hitting one detector cannot, after punching through, travel through vacuum before hitting another detector. Also, since no realistic particle transport in the detector material is calculated, some effects, especially those due to loss of charge, cannot be simulated. These restrictions had only very limited influence (e.g. the bend E_{Si}-E_{Bargg} curve in Fig. 6.12) on the analysis of the experiments discussed here.

The definition of the setup, `Detectors` reads from a file specifying the geometry and the materials involved. Their positions are given in Cartesian coordinates with respect to the target position, and the material of the detector layers is described in a molecular notation. Pseudo-detectors, i.e. detectors that are not evaluated, can be used to restrict the acceptance of the real detectors by blocking them. The calling parameters `Detectors` define, which quantities are to be calculated for each particle and allow to set a coincidence level. The latter is defined as a minimum number of particles required to have hit in order for the event to be passed to the output. The data file produced by `Source` is analyzed line-by-line and an output table with the respective detector response is generated. Unlike `Source`, `Detectors` already supports more than two particles per events.

The output of both `Source` and `Detectors` is processed with standard UNIX utilities like `awk`, `grep` or `sed` and visualized with any graphics program that is capable of importing ASCII-tables. Fig. 6.13 gives a hit-pattern of the setup shown in Fig. 6.6 for simulated p(^{17}F,p) and p(^{17}F,α) scattering. The geometry of the setup is nicely outlined by the hits. In addition to the two main programs, some tools were written that provide simple gating and binning functions. The major benefit of the concept is the separation of production of particles in a reaction or a source and the detection. The system can be easily debugged and filters can be used between the production and detection of particles. Finally, problems that do not involve the detection can be treated with `Source` alone. For more information, see the readme-file of the program in the Appendix -section 8.2. All Monte Carlo calculations in this thesis are done with a combination of `Detectors` and `Source` or with `Source` alone.

7 Data and Results

The data presented here originate from two experiments, carried out in August 1998 and November 1999. In the first experiment, measurements of the $^{17}F(p,\alpha)$ reaction with both thin (100 $\mu g/cm^2$) and thick (500 $\mu g/cm^2$) CH_2 targets were performed. The setup used is described in section 6.2. In this experiment, we were not able to distinguish between elastic and inelastic proton scattering of ^{17}F and ^{16}O, since no *Z*-identification of the heavy reaction product was available, and the solid angle coverage was not adequate. However, the measured $^{17}F(p,\alpha)^{14}O$ excitation function was used to check previous assumptions[25] about the level scheme in ^{18}Ne. In the second experiment, additional thin-target data on the $^{17}F(p,\alpha)$ reaction were obtained using the experimental configuration described in 6.3. In addition, the $^{17}F(p,p)$- and the $^{17}F(p,p')^{17}F^{495}$ reactions were also investigated simultaneously. Since the two setups use different data analysis techniques and have different acceptances, the data of the two experiments are discussed separately in section 7.1 and 7.2, respectively. Conclusions from the combined information are drawn in section 7.3.

7.1 Data from the August 1998 Experiment

In the Ludwig II configuration, described in section 6.2, two different targets were used. One thick 500$\mu g/cm^2$ CH_2 target was employed to search in relatively short runs for regions of increased yield in the $^{17}F(p,\alpha)$ excitation function. The results using this configuration were part of our first publication[43] on $^{17}F(p,\alpha)$ and are shown in Fig. 7.1, compared with an estimate of the direct contribution taken from the literature[13].

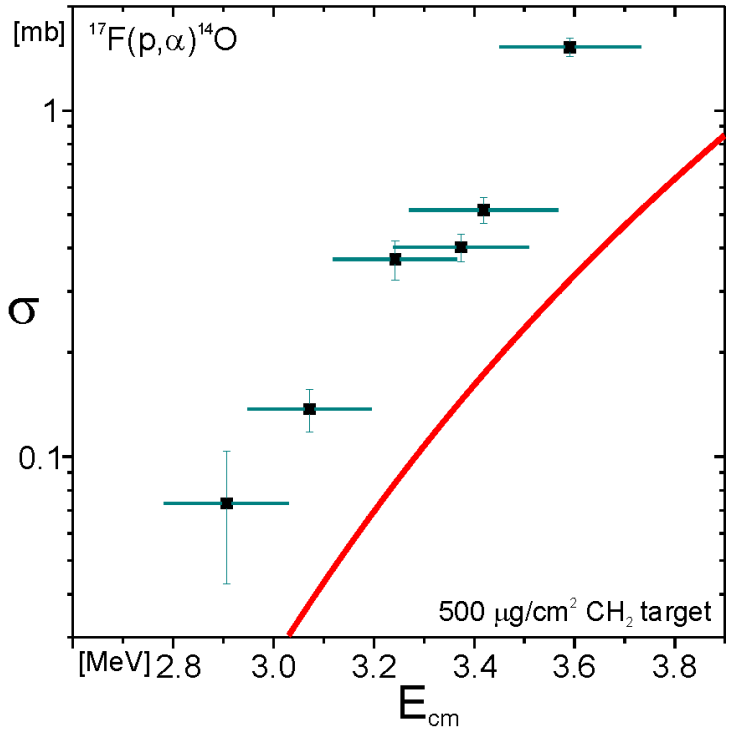

Fig. 7.1 **Thick-target cross-sections plotted as a function of the center-of-mass energy. The horizontal error-bars indicate the target thickness rather than an uncertainty. The cross-sections error bars indicate the statistical error only. The solid line is an estimate for the direct contribution taken from the literature[13].**

The horizontal error bars indicate the area of integration over the energy loss in the target rather than an uncertainty in energy. The beam energy uncertainty was less than 15 keV in the center of mass system, arising mostly from the energy distribution of the ^{17}F beam particles on the target. The errors in the cross-sections shown here are purely statistical. The systematic error is estimated to be less than 20%, mostly due to uncertainties in the ^{17}F beam intensity and the angular distributions of the α-particles.

In addition to the thick target measurements, studies with a thin 100 µg/cm^2 CH_2 target were undertaken, measuring an excitation function in the region of 3.3 MeV < E_{cm} < 3.7 MeV and probing the expected[25] resonances around E_{cm} = 2.3 MeV. Fig. 7.2 shows the measured cross-sections in these regions of E_{cm} < 3 MeV and E_{cm} > 3 MeV.

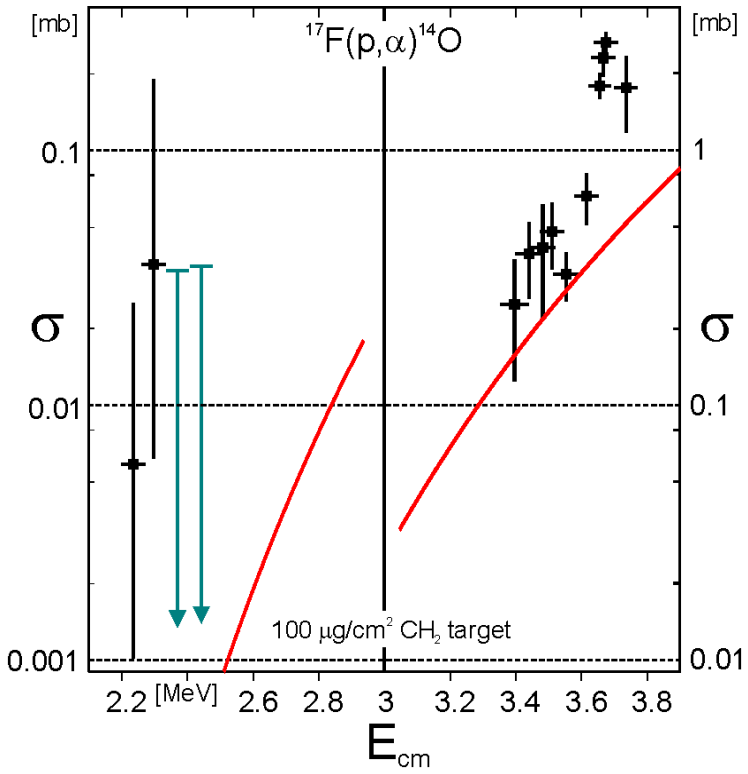

Fig. 7.2 Thin target cross-sections of ^{17}F(p,α)^{14}O. The solid line indicates the estimated direct contribution. The error-bars are statistical in s and represent the folded target thickness and beam energy spread in E_{cm}.

The energy resolution of the ^{17}F-beam was ~500 keV and the energy loss in the target 700keV, resulting in a combined energy resolution of better that 70 keV in the center of mass system with a systematic uncertainty of 10 keV (center of mass) from the ^{17}F-energy distribution on the target. In addition to the statistical uncertainties of the cross-sections shown in Fig. 7.2, a 20% systematic error is expected from the uncertainties of the ^{17}F beam intensity and the alpha angular distribution. Within the statistical uncertainties, the thin target results agree with the thick target measurements.

Together with the total cross-sections, angular distributions for the ^{17}F(p,α)^{14}O reaction were measured. For that purpose, the two-dimensional spectrum of ring-number vs. $E_{lab,a}$ (Fig. 6.5b) was separated into five angle bins, as shown in detail for the data from the Super Ludwig setup in Fig. 7.5. The number of counts in each bin was compared with a Monte Carlo calculation for isotropic emission of α-particles in the center-of-mass frame and an angular distribution calculated

from the ratio. As shown in Fig. 7.3, the result did not allow to restrict the spin and parity of the resonance to a certain value. The solid and the dashed lines indicate calculations for the angular distributions of 1^- and 4^+ states, respectively. No discrimination between these alternatives is possible because of a lack of data at the smallest and largest angles in the center-of-mass system. For reasons of radiation damage, the forward Si-detector which detected the outgoing ^{14}O particles, could not be positioned closer than 4° to the beam, thereby severely limiting the acceptance at small and large center of mass angles.

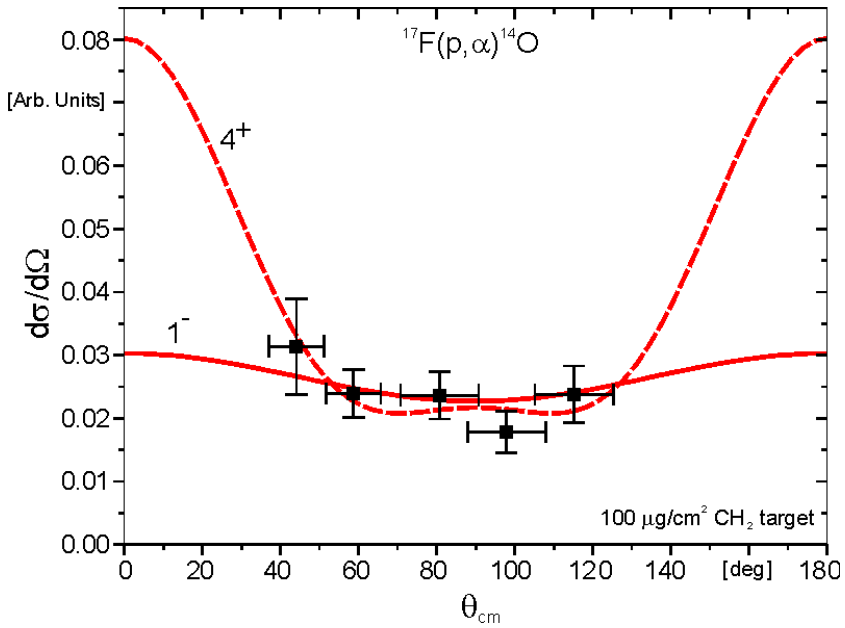

Fig. 7.3 Measured angular distribution of the α-particles at E_{17F} = 66 MeV. The solid and dashed line indicate the expected angular distributions for a J^p=1⁻ and J^p=4⁺ resonance, respectively. The measurement is inconclusive with respect to the total angular momentum of the resonance.

7.2 Data from the November 1999 Setup

Performed with the Super-Ludwig setup described in section 6.3, this experiment generated data on $^{17}F(p,p)$, $^{17}F(p,\alpha)$ and $^{17}F(p,p')$ reactions. All measurements were performed with a 100 µg/cm^2 target. The (p,α) measurements are therefore directly comparable with the thin-target data from the August 98' run. Fig. 7.4 shows the high-energy data of both experiments combined. One thick target point at E_{cm} = 3.24 is included, which is in good agreement with the thin target data. Also, the overlapping points of the two thin target experiments agree except for the point at E_{cm} = 3.6 MeV, for which an average will be used for the further analysis.

As in the experiment in summer 1998, angular distributions of the α-particles were measured. Fig. 7.5 shows both the data and the method of analyzing it for two energies close to the resonances at 7.06 and 7.91 MeV in ^{18}Ne. On the left side, the raw data (vertical bars) are overlaid with simulated events* from a Monte Carlo calculation for the reaction assuming an isotropic angular distribution. Also shown are the regions in which both the data and the Monte Carlo counts were summed.

* Note, that not all counts of the Monte Carlo simulation are shown in the figure.

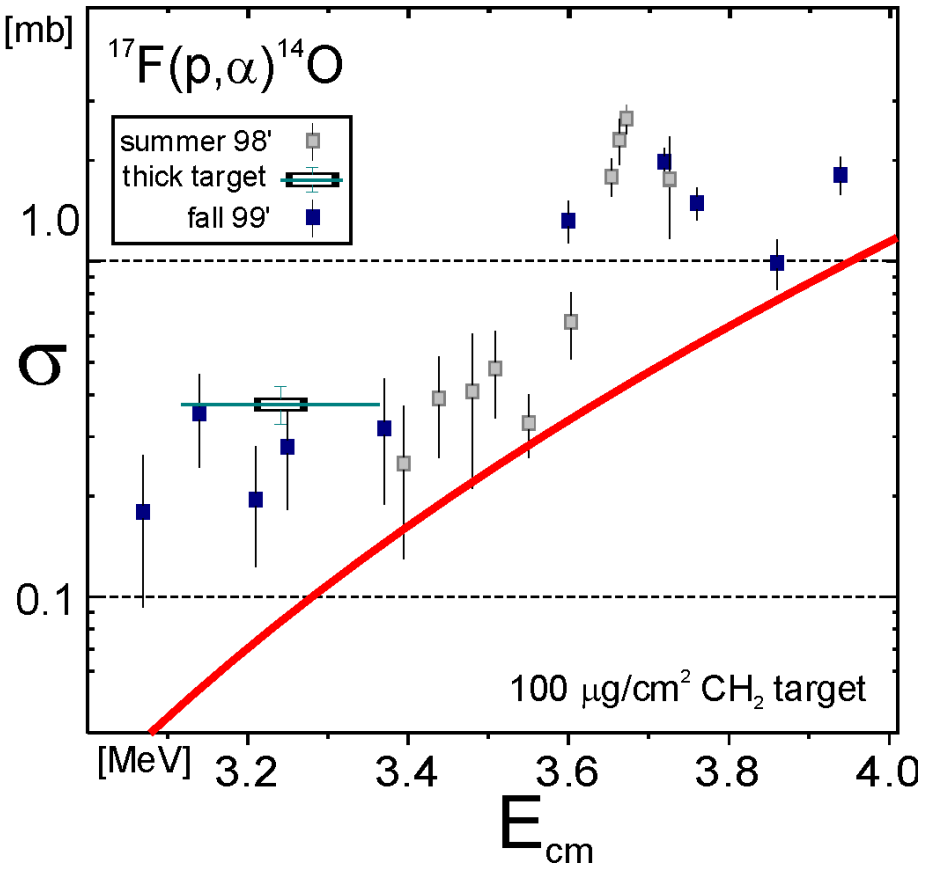

Fig. 7.4 **$^{17}F(p,\alpha)^{14}O$ cross-sections measured with 100 μg/cm² targets. Data from August 98 are shown along with the data from the November 99 experiment and the calculated direct reaction cross sections (solid line). Error bars are statistical.**

If the total number of α-particle counts in the data is N_{data}, the fraction in a given region $N_{reg,data}$ and the corresponding numbers of α-particles in the Monte Carlo simulation N_{MC} and $N_{reg,MC}$, the unnormalized cross-section is given by

$$\frac{ds}{d\Omega}(q_{cm,MC}) \propto \frac{\frac{N_{reg,data}}{N_{data}}}{\frac{N_{reg,MC}}{N_{MC}}} \tag{7.1}$$

This procedure ensures, that efficiencies, target effects, beam-spot size etc. are properly taken into account since they are also included in the Monte Carlo simulation. Similarly, the center of mass angle $q_{cm,MC}$ for the region is determined by averaging the center of mass angles $q_{cm,i}$ of all Monte Carlo events that fall into it:

$$q_{cm,MC} = \frac{\sum_{i=1}^{N_{reg}} q_{cm,i}}{N_{reg,MC}} \tag{7.2}$$

$q_{cm,MC}$ is therefore a solid-angle-weighted average scattering angle of the respective bin. The resulting angular distributions is shown on the right side of Fig. 7.5. Unfortunately, the statistics at the large angles is not sufficient to rule out certain spin assignments for the respective resonances (Fig. 7.5). Some information, however, can be obtained for the resonance at E_x = 7.6 MeV, which is discussed below (Fig. 7.9).

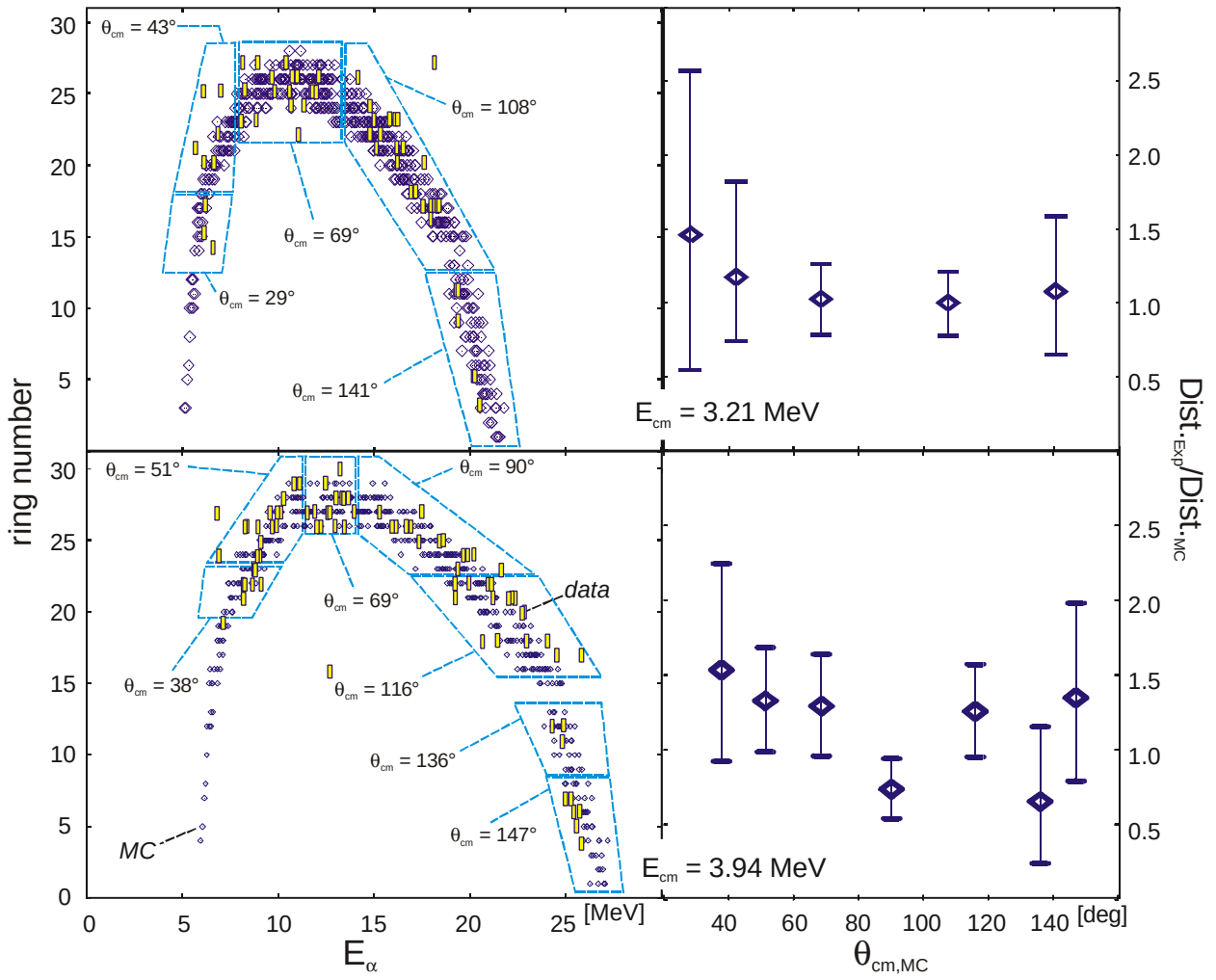

Fig. 7.5 **Alpha data for ^{17}F(p,α) at E_{cm} = 3.94 MeV and E_{cm} = 3.21 MeV . Left: Binning of the raw data into groups together with isotropic Monte Carlo calculation. Right: Derived angular distributions with statistical errors[54]**

The elastic proton scattering data were evaluated in a comparable way to the α data: regions of the detector were assigned to center of mass angles q_{cm} by averaging over the center-of-mass angles of counts from a Monte Carlo calculation. However, in order to calibrate detection efficiencies for protons, a different scheme was employed. The detection efficiencies for protons were expected to deviate from the values obtained from a an alpha source calibration. The range of the protons in the silicon detector (for most angles > 0.5 mm) is comparable to the width of the detector ring segments (1.5 mm). Since the protons enter the detector at an angle, a fraction of the protons will pass from one segment to another, thereby changing the electronic response of the detector and complicating the data analysis.

Since the kinematics of elastic scattering of protons off ^{16}O is very similar to the ^{17}F case, the well measured[55] elastic proton scattering off ^{16}O was employed to determine the systems response. Protons scattered off the ^{16}O beam contamination were analyzed analogue to the technique described for the α-particles. The result was compared with a Monte Carlo calculation of the proton response of the idealized system with zero-depth detectors. Using measured proton scattering phase shifts from the literature to describe the center of mass angular distributions, deviations of the order of 10% were found.

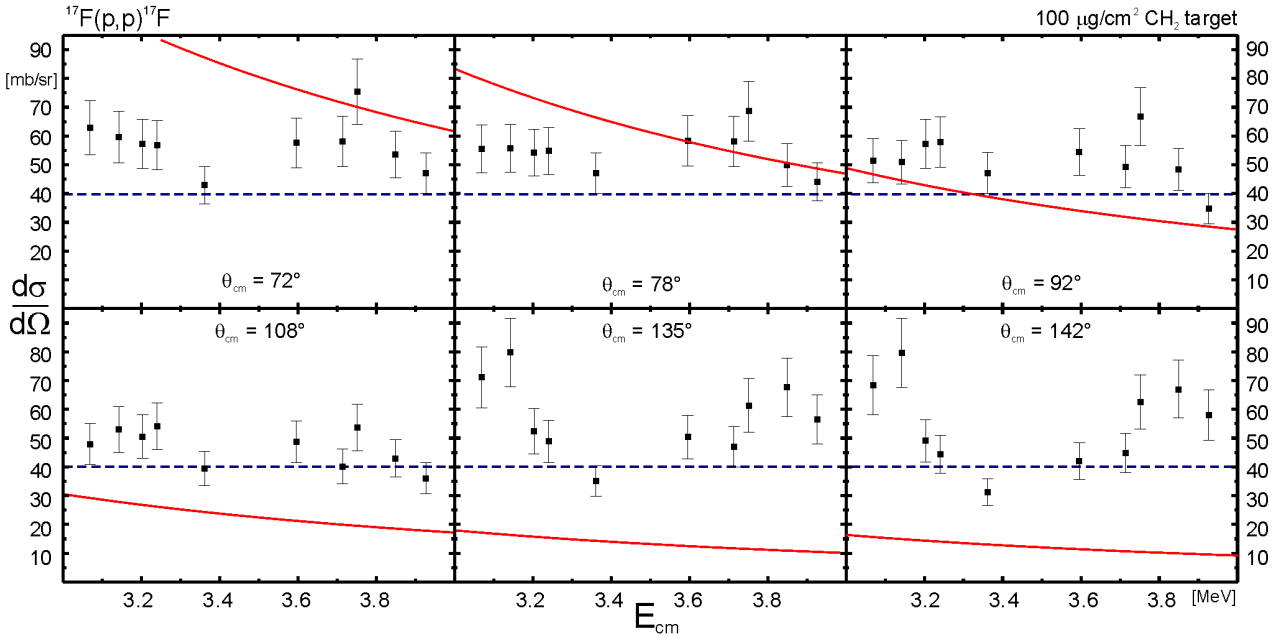

Fig. 7.6 **Excitation functions for elastic proton scattering off ^{17}F. The solid lines are the Rutherford cross-section, the dashed line a geometric estimate of the nuclear potential cross-section. The error-bars are dominated by the uncertainties of the ^{17}F beam intensity.**

With these efficiencies, the same approach of binning and comparing count rates to a Monte Carlo calculation of ^{17}F(p,p) assuming isotropic angular distribution was employed to determine the angular distribution. The excitation functions of ^{17}F(p,p) at six angles in the range 72° < q_{cm} < 142° and 3 MeV < E_{cm} < 4 MeV is presented in Fig. 7.6. Also shown is the Rutherford cross-section and the geometric cross-section of a hard sphere with radius $R = 1.25*17^{1/3} + 0.8$ [fm] to provide a scale.

A measurement of the cross-sections for inelastic scattering ^{17}F(p,p')^{17}F^{495} was possible only in a small angle regime (q_{lab} = 52.5° - 56.5°), providing one data point at q_{cm} ~ 70°. The insert in Fig. 7.7, right, shows this segment in the E_p-q_{lab}-plane as "projection area". At all other angles, a separation of elastic and inelastic scattering was problematic: It was decided, not to use data from angles where either of the groups starts to punch through the detector. Because of the finite beam-spot size, detector effects and multiple scattering, elastically scattered protons could easily be mistaken as part of the inelastic group at these angles. At angles below 42°, the energy separation of the two groups becomes too small, again making a distinction difficult.

The analysis of the inelastic data at q_{cm} = 70° was done with two different assumptions about the actual shape of the elastic background under the inelastic peak: A linear elastic tail starting at the minimum of the Q-value distribution and tail derived from ^{16}O(p,p) elastic scattering. These two alternatives are shown on the left side of Fig. 7.7 as thinner dotted and dash-dotted lines. No detailed knowledge about the actual shape existed, the use of the oxygen scattering represented only an approximation since the energy of the protons from ^{16}O(p,p) elastic scattering was lower and therefore closer to the electronic thresholds. More severely, the ^{16}O beam was expected to show a different intensity distribution over the target area and was wider in energy. While the linear background assumption is likely an overestimation of the actual situation, the oxygen scattering peak is probably an underestimation because of its proximity to the threshold. The average of the two alternatives was used. If one method was in agreement with the assumption of no signal, the

error bars were extended downwards to zero. Only for two energies, a clear signal was identified. The resulting cross-sections are given in Fig. 7.7, right side, assuming an isotropic angular distribution.

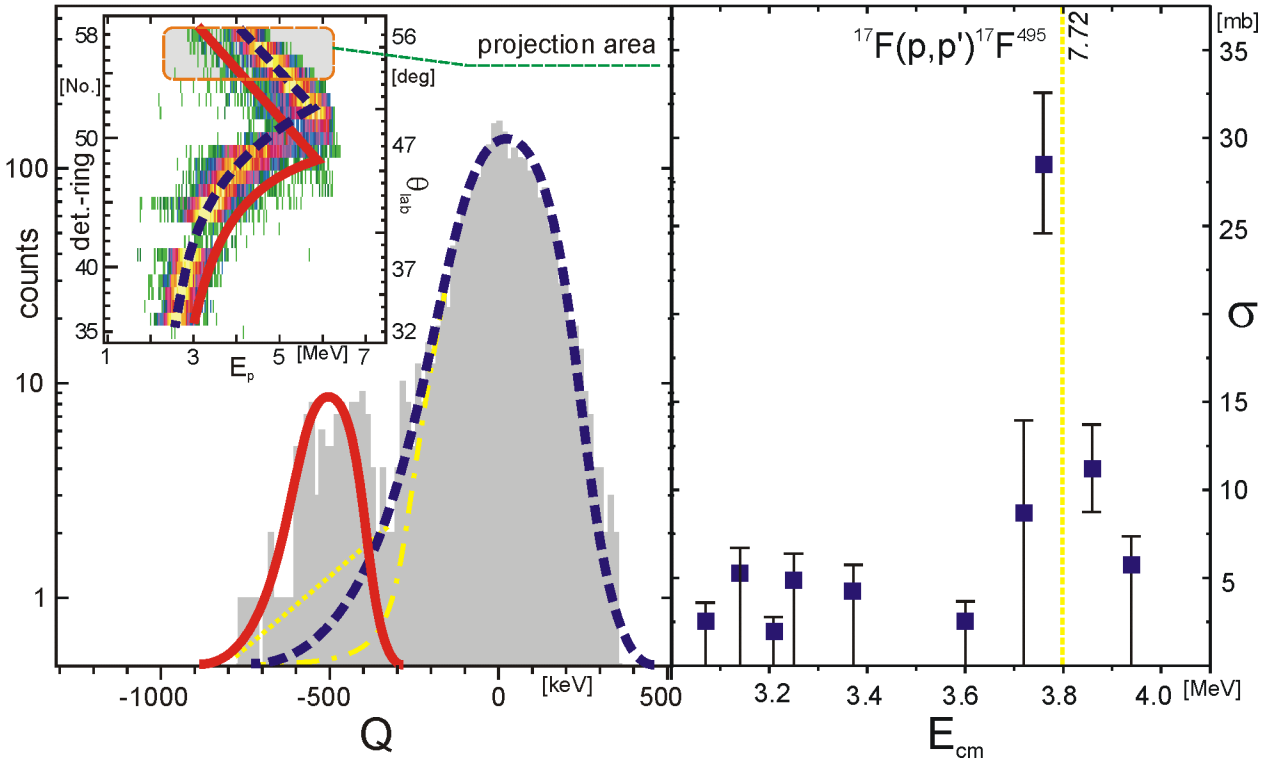

Fig. 7.7 **Right: Cross-section for the inelastic scattering ^{17}F(p,p')^{17}F^{495}, populating the first excited state in ^{17}F at 495 keV. The error-bars are statistical or upper limits. Left: Q-value spectrum of the elastic and inelastic proton scattering of one run measured at E_{cm} = 3.76 MeV. Insert: Scatter plot in the q_{lab}-E_p plane. The solid line shows the kinematic curve expected for inelastic scattering, the dashed line for elastic scattering. The dotted and dash-dotted lines show two different assumptions about the background under the inelastic peak.**

7.3 Assignment of States in ^{18}Ne

In the following, spin-parity assignments of states in ^{18}Ne will be attempted, combining all available information, i.e. known states in the mirror nucleus ^{18}O, Coulomb-shifts, excitation functions and the observed partial widths. Fig. 7.8 shows all known levels in both ^{18}O and ^{18}Ne. It can be stated[56,57] that all states up to the first 2^- (E_x = 5453 MeV) state are already identified and assigned to analogue states in the respective mirror nucleus.

The next group of states in ^{18}Ne is located at E_x = 6150, 6297 and 6353 keV respectively. In a recent measurement[15], the 6150 keV level was assigned 1^- (G = 50 keV) and the 6353 level 2^- ($G\tilde{}$ 50 keV). That is consistent with our first p,α-experiment, in which we observed yield in the 6150 keV region, but not around 6353 keV. From the average of our two data points in the region and the measured total width, we calculate a value of $G_a = 3.2^{+5}_{-2}$ eV for the 1^- state. No direct information on the ratio of $G_p/G_{p'}$ is available for this state. However, in the elastic scattering measurement of Ref.[15], a large value of $G_{p'}$ and the observed width of 50 keV would have resulted in a peak at E_{cm} = 1.7 MeV, which was not reported. We therefore assume $G_{p'} << G_p$ for this state.

The state at E_x = 6297 keV was observed in ^{16}O(^{3}He,n) and ^{20}Ne(p,t) measurements. Since low-lying negative parity states in ^{18}Ne are not expected to show large Coulomb shifts[58], it is likely to be the analogue state of the 3^- state at E_x = 6404 keV in ^{18}O. The suggested other assignment of 4^+ is unlikely since the 3^- state would be missing in this case and no 4^+ state is expected in this region. From the Wigner limits, the inelastic proton and alpha widths $G_{p'}$ and G_a of the state cannot exceed 3.3 keV and 1.8 eV, respectively. Our limit for G_a from the data is 3.4 eV. Since a measurement of the excitation function for elastic proton scattering[15] does not show a strong resonance, the total width has to be small.

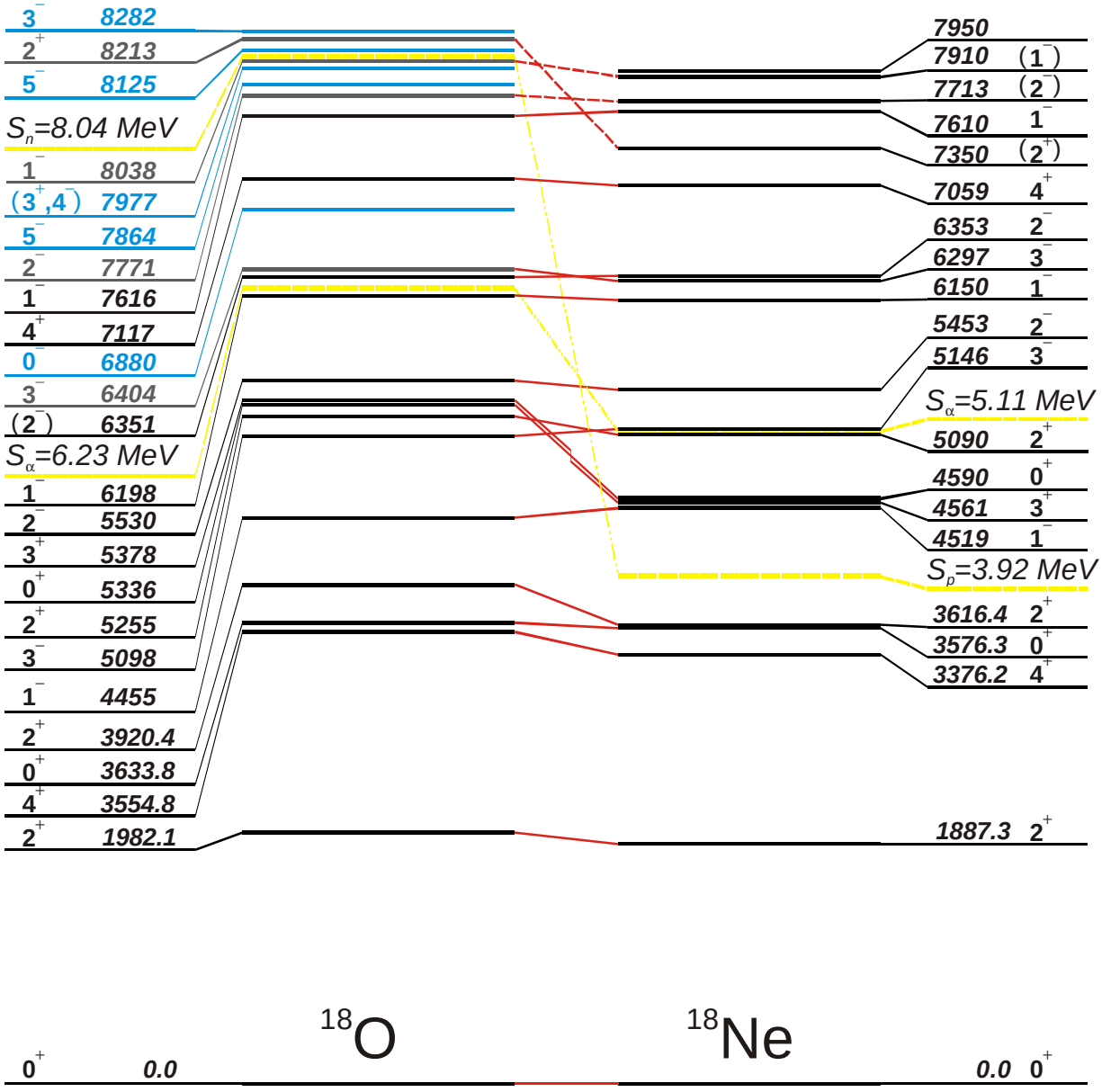

Fig. 7.8 Assignment of levels in ^{18}Ne and their analogue states in ^{18}O

Our assignment of the 7059 keV level to be 4^+ is supported by the following observations: the pp-elastic scattering excitation function agrees, especially at the sensitive angle of q_{cm} = 142°, with this assignment (see Fig. 7.10, Fig. 7.11). Since the state is expected to have a strong ^{14}O + α

component[58], it should also have a large α-width. With a total width of 80 keV, which fits our (p,p)- and (p,α) data, we find G_a = 38 eV and thus a reduced width of 0.52. Only an upper limit for the inelastic proton width $G_{p'}$ < 0.6 keV was obtained, which is consistent with the Wigner-Limit of 0.62 keV.

For the state at E_x = 7350 keV, (G = 73 keV) little experimental information is available, since it was covered on resonance only in the ^{17}F(p,α) measurement with the Ludwig II setup. The observed α-strenght is in reasonable agreement with the assumption of a 2^+-state with G_a = 43 eV. However, 1^- , 3^- or 4^+ are also possible spin-parity assignment. Since there is no missing 4^+ analogue state in ^{18}O left for assignment, this possibility can be ruled out. A 2^+ state would be the analogue of the 8213 keV level in ^{18}O. For a 3^- assumption, the analogue state would be at E_x = 8282 keV and should have a large α-strength, which we do not observe. For a 1^- assignment, the correspondent state would be the at 7616 keV in ^{18}O. Since we can exclude a 2^+ assignment for the next higher level at E_x=7.61 MeV in ^{18}Ne, and because theoretical arguments[58] require the 2^+ state to come down in this energy region and because of weak evidence from elastic scattering (the data point at E_x = 7.29 MeV is low, as expected for a 2^+ state, see Fig. 7.10, Fig. 7.11) we tentatively assign the 7.35 MeV state to be 2^+.

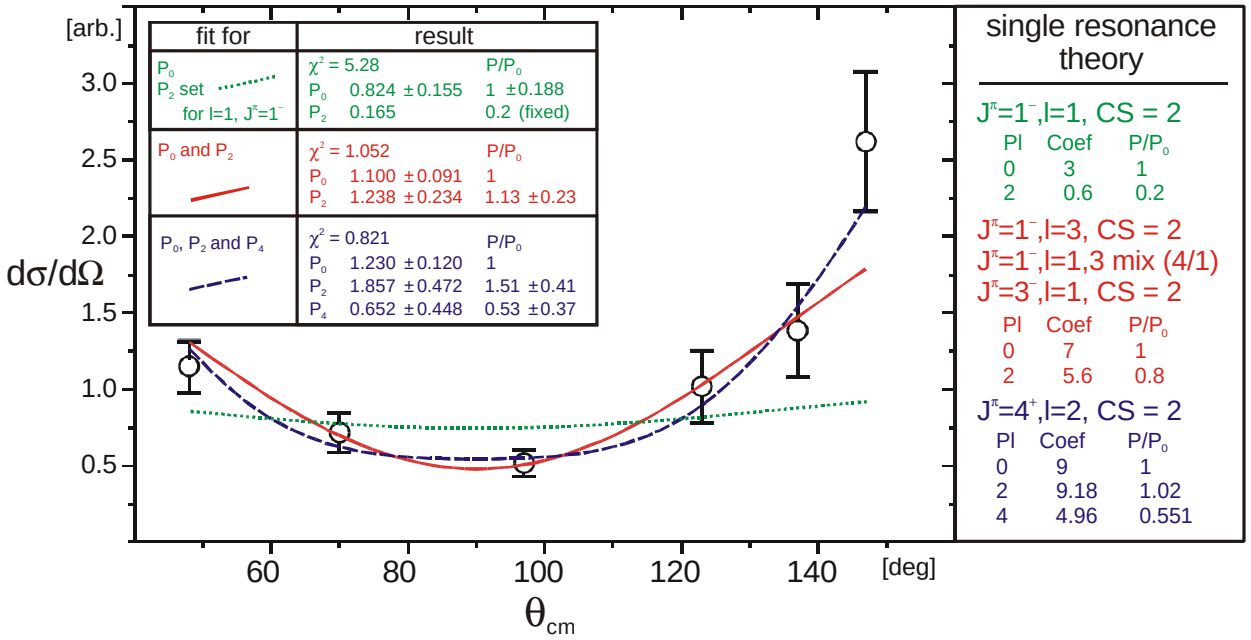

Fig. 7.9 **Fit of spherical harmonics to the a angular distribution near the E_x =7.61MeV in ^{18}Ne assuming a 1^- -state, free parameters P_0, P_2 and free parameters P_0, P_2 ,P_4. Right: Theory values for the cases of $J^p = 1^-, 3^-$ and 4^+, in the latter two cases for the channel spin with the maximum ratio s(140°)/s(90°) (CS=2).**

The state at E_x = 7.61 ± 0.02 MeV (G = 72 keV) is strongly populated in the (p,α) reaction. The choices from the Wigner-limits (see Fig. 3.4) are $J^p = 1^-, 2^+, 3^-$ and 4^+. The elastic scattered proton excitation functions exclude the $J^p = 4^+$ possibility since this would produce a clear peak in the spectrum in Fig. 7.10. Also, there is no known 2^+ or 4^+ state in the mirror nucleus left for assignment. The (p,α)-angular distribution (Fig. 7.9) allows a 1^- assignment for a ≥ 20% l = 3 contribution, requiring an expected admixture of the $f_{7/2}$ intruder into the resonance. Similarly, a 3^--state can produce the observed angular distribution. However, a 3^- assignment would have a G_a of 0.43 keV, 7.7% of the Wigner limit. The ten times larger reduced alpha-width (0.72 in

Ref[59]) and the extensive Coulomb shift of the then-mirror state at E_x = 8282 keV in ^{18}O make such an assignment less likely. We therefore suggest a 1^- assignment. Here, the Coulomb-shift would be minimal ($E_{x,18O}$ = 7.62 MeV).

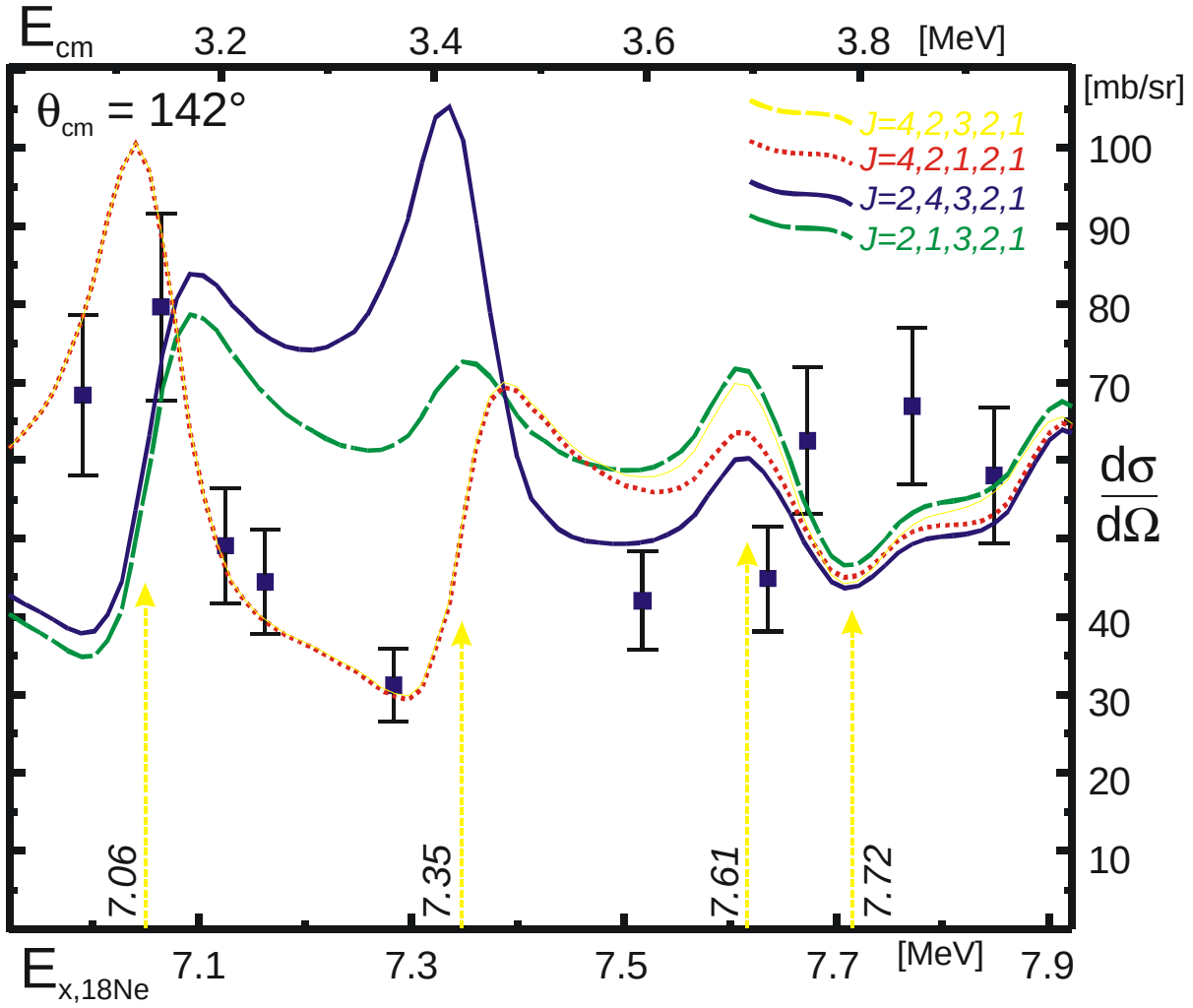

Fig. 7.10 R-Matrix calculation (MULTI) and ^{17}F(p,p) elastic scattering data at q_{cm} = 142°. While no information for the states above E_x = 7.3 MeV can be obtained, the 7.06 MeV state can be assigned to be 4^+, G = 80 MeV. The numbers for the respective line styles refer to the total angular momentum J of the states at E_x = 7.06, 7.35, 7.62, 7.72 and 7.91 MeV.

Both ^{16}O(^{3}He,n) and ^{20}Ne(p,t) measurements identified a state at E_x = 7.713 keV in ^{18}Ne. We also find a peak in the excitation function for inelastic scattering at E_x = 7.72 ± 0.02 MeV with a width of 80 ± 40 keV. The errors in the width and the resonance energy are dominated by the uncertainties of the beam particle energy distribution and the statistical errors from the least squares fit (see Fig. 7.12). Expression 3.10 (no background term) was used to fit the 7.72 MeV resonance. The assignment of a certain spin and parity to this level is difficult. Since the (p,α) yield for this state is small, one can conclude that it is likely an unnatural parity state. There is a 2^--level in ^{18}O at E_x = 7771 keV. The elastic scattering data do not exclude this possibility, and the large inelastic scattering width supports a $J^p = 3^+$. Thus, this level is tentatively assigned 2^-.

At the highest energy corresponding to E_x = 7.86 MeV in ^{18}Ne, we observe an increase in yield of the ^{17}F(p,α)^{14}O reaction. In ^{16}O(^{3}He,n) and ^{20}Ne(p,t), a state is observed at E_x=7.91 MeV, but no

spin assignment has been made. From our data point and the resonance energy, we obtain a lower limit for its width of 50 keV with a partial alpha width of $G_a > 1.0/(2J+1)$ keV and a best fit for a width of ~70 keV and a $G_a = 2.2/(2J+1)$ keV. It is, however, possible, that the strength of the state is considerably larger. The alpha angular distribution (see Fig. 7.5) is not conclusive, but consistent with a small angular momentum, including 3^-. Since there is at least one 1^- state in ^{18}O (E_x = 8038 keV) left for assignment, which should not show a large Coulomb shift, we tentatively assign the state at 7.91 MeV to $J^p = 1^-$. There is also a possibility of the state being the analogue of the 3^- at E_x = 8282 keV in ^{18}O.

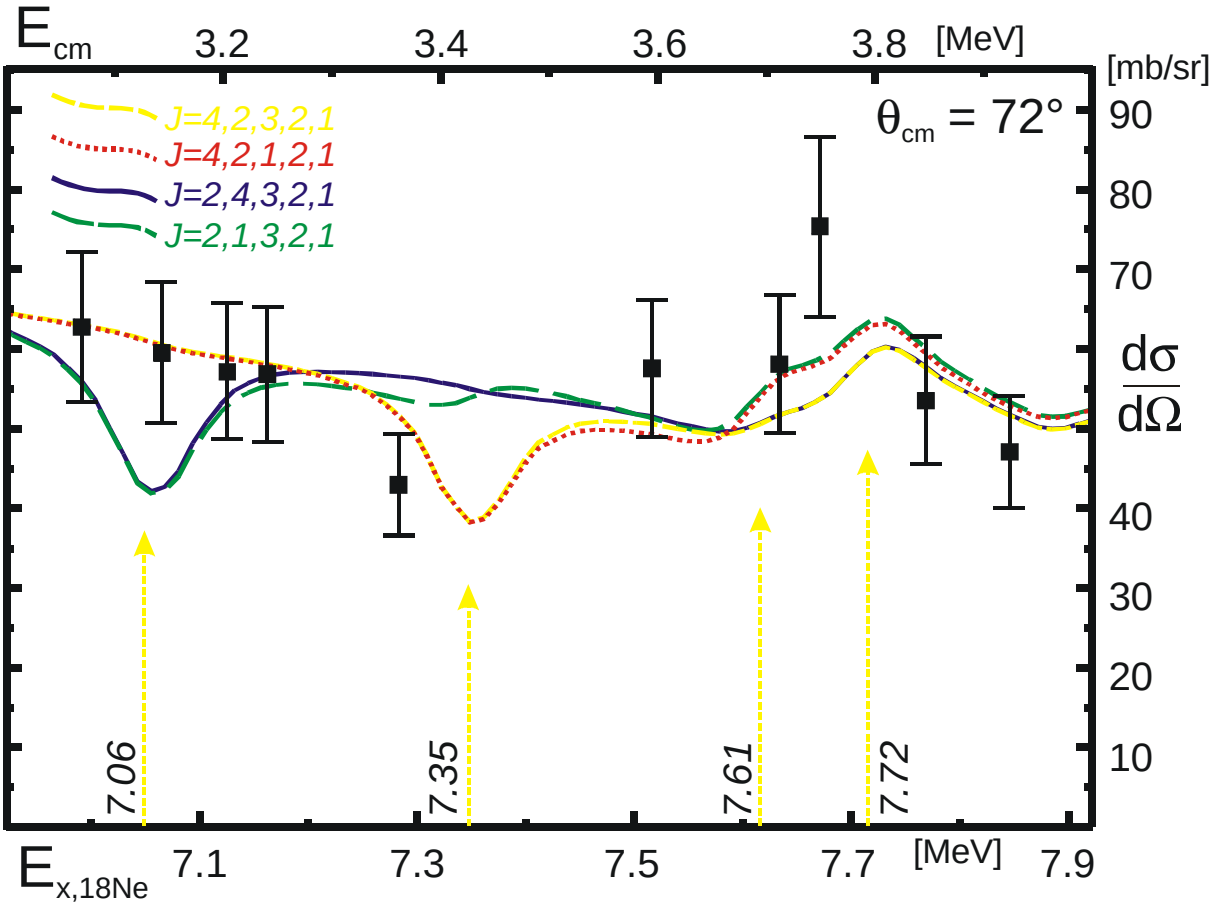

Fig. 7.11 MULTI-R-Matrix calculation (scaled by 0.4) and ^{17}F(p,p) elastic scattering data at q_{cm} = 72°. Weak evidence for a 4^+-assumption for the E_x=7.06 state and the 2^+-assumption for the E_x=7.3 MeV state can be derived from the data. The data in the E_x = 7.6 MeV region is non-conclusive.

Finally, is should be noted, that the thick target measurement (see Fig. 7.1) showed a (p,α) yield below E_{cm} = 3 MeV that is significantly above the estimated direct background. Since there are no low-lying natural parity states in ^{18}O left for assignment, this could indicate that the direct contribution is underestimated, at least in this energy region. Another possibility is, that the state observed in the (^{3}He,n) and (p,t) experiments at E_x = 6.30 MeV and now assigned 3^- is identical with the 2^- state at 6.35 MeV, clearly seen in the recent proton scattering experiments[15]. This suspicion is fed by the surprising non-observation of a state at 6.30 MeV in that measurement. Its reported width of 140 keV from the (^{3}He,n) experiment is in clear disagreement with the (p,p) result. In this case, the 3^--state would still be missing, and could well be located between 6.35 < E_x < 6.9 MeV, contributing to the observed yield.

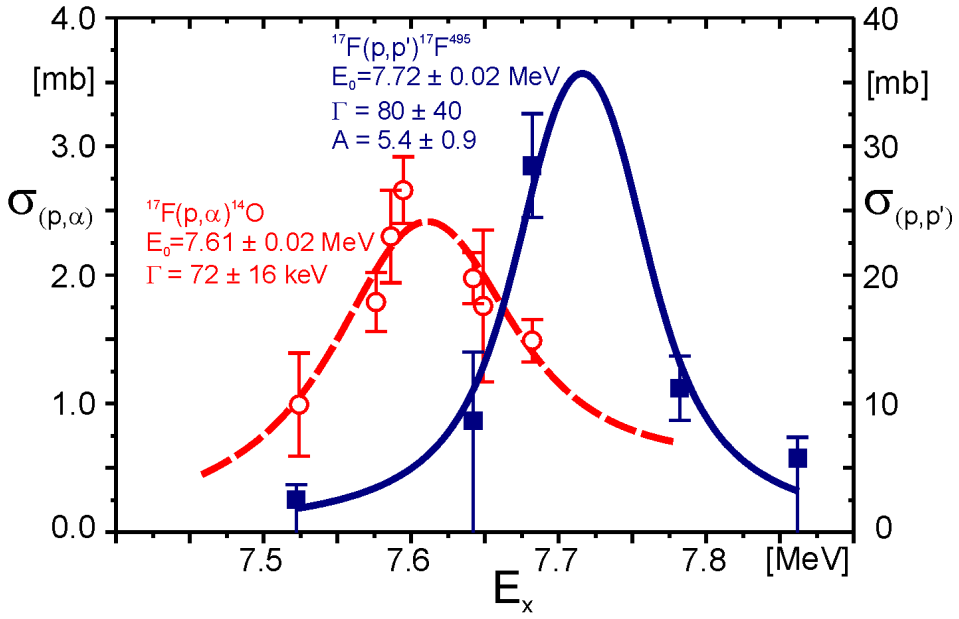

Fig. 7.12 Excitation function of inelastic proton scattering (solid line) in comparison with the excitation function for the ^{17}F(p,a)^{14}O reaction. The least squares fit to the data takes the target thickness and the finite energy width of the beam into account.

Fig. 7.13 shows a least squares fit to all alpha resonances using the expression 3.10 for each peak as a parameterization.

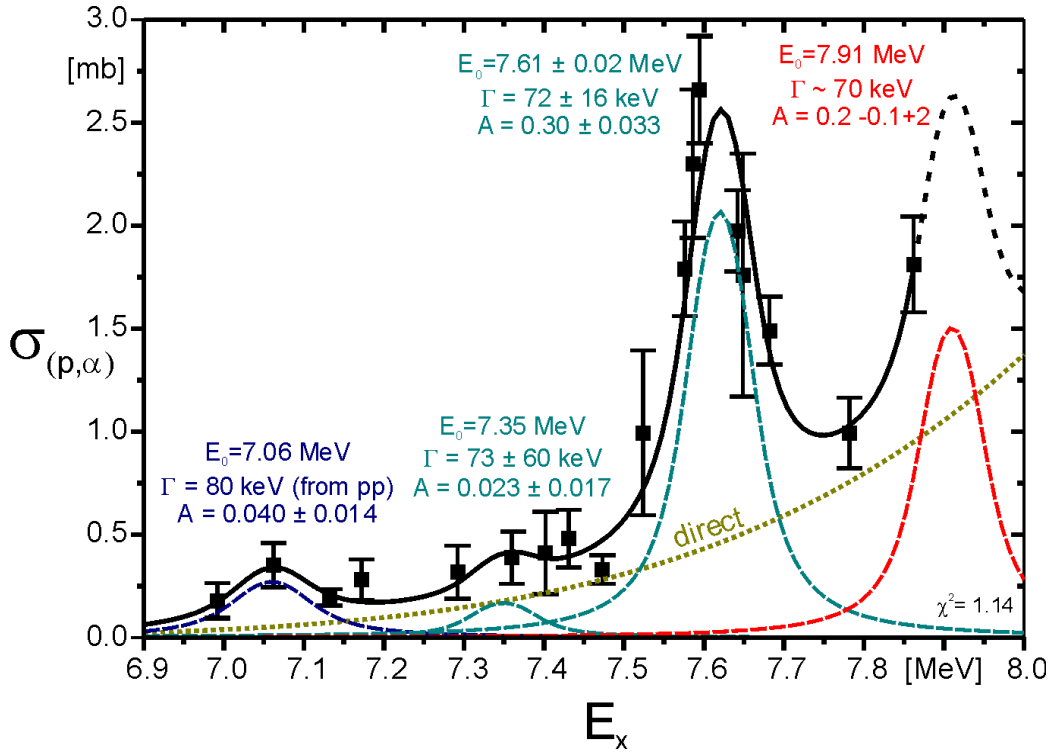

Fig. 7.13 Least squares fit to four resonances in ^{17}F(p,a) to determine the widths and amplitudes. The solid line represents the sum, the dashed lines the respective resonances and the dotted line the direct background as provided by Funck and Langanke.

The energy values for all but the 7.61 MeV state were taken from the literature, and the direct contribution (mostly 1^-) from Funck and Langanke[13] added as a first order correction. Note, that

in principal, the background should be treated as an interfering term instead of as an offset to the cross-section. However, since it is a small contribution, the resolution of the present measurement does not allow to decide about the phase. This does introduce a substantial uncertainty for the strength of the resonances at 7.92 and 7.35 MeV if one of these should be 1^-. In the fit, the width of the 7.92 MeV resonance was adjusted to 70 keV and for the 7.06 MeV resonance to 80 keV, a value compatible with both elastic proton scattering and (p,α) data. For the 7.92 MeV resonance, the error in G was estimated by a comparing results with different width and their impact on they quality of the fit of the 7.61 MeV resonance.

The parameters for the states in ^{18}Ne are summarized in Table 3, combining the information gathered in this thesis, from theory and from other recent measurements. The values of G_a are calculated using equation 3.12 except for the value for the 6.15 MeV state, that is based calculated using equation 3.13. For the 7.72 MeV data point in ^{17}F(p,p'), equation 7.5 was used for $G_{p'}$ instead for G_a.

J^p	$E_x(^{18}Ne)$ [MeV]	$E_x(^{18}O)$ [MeV]	G [keV]	G_a [eV]	$wg_{(\alpha,p)}$ [eV]	G_p [keV]	$G_{p'}$ [keV]	$\frac{G_a}{G_{a,Wigner}}$
1^-	6.15	6.198	50[a] ± 5	3.2^{+5}_{-2}	9.6^{+15}_{-6}	50 ± 5		0.25
3^-	6.30	6.404	small[a]	< 3.4 < 1.8[b] 0.34[c]	2.4[c]	small[a]	< 3.3[b]	
2^-	6.35	6.351	~ 50[a]	–	–	50		–
4^+	7.06	7.117	80 ± 40	38·± 13	324 ± 117	80 ± 40	< 0.6	0.5
(2^+)	7.35	8.213	73 ± 60	43 ± 32	215 ± 163	73 ± 60	< 2	0.004
1^-	7.61	7.62	72 ± 16	1000 ± 110	3000 ± 330	72 ± 16	< 4	0.013
(2^-)	7.72	7.771	81 ± 40	–	–	68 ± 40	13 ± 5	–
(1^-)	7.92	8.04	> 50 [~70]	> 300 [~730]	[~ 2200]	[~70]	[< ~6]	[~0.005]

Table 3 Compilation of resonance parameters for states in ^{18}Ne for E_x = 6-8 MeV. Errors are 1 s, unsymmetrical errors are calculated according to a Poisson distribution[54]. Indices:
[a]taken from Gómez del Campo[15]
[b]from Wigner- limit
[c]estimate by Hahn[25] et al.

7.4 Astrophysical Reaction Rates

Calculations of astrophysical reaction rates for the ^{14}O(α,p)^{17}F reaction based on equations 3.2 and 3.4 are presented in Fig. 7.14. On the left side, the contributions of the resonances is shown independently with the error bands from the uncertainty of the respective G_a. In the following, the relative importance of the respective resonances in the temperature range $0.5 < T_9 < 3$ is discussed. At all but the highest temperatures well above $T_9 = 2$, which occur in X-ray bursts, the 6.15 MeV 1^- state dominates. The uncertainty of its G_a -value gives raise to an uncertainty of one order of magnitude in the resonant ^{17}F production in this region. The 4^+-state at E_x = 7.06 MeV gains importance around $T_9 = 2.5$. Only at very high temperatures of $T_9 \sim 3$, the two states at E_x = 7.61 and 7.91 MeV contribute significantly. The 2^+-state ate 7.35 MeV has no importance for the stellar ^{14}O(α,p)^{17}F rate at any temperature.

The right side of Fig. 7.14 compares the contributions to the stellar ^{17}F production mechanisms. The direct contribution (long-dashed line) is about as strong as the contribution from the combined high-lying states (short dashed line) in the range of 7 MeV < E_x < 8 MeV in ^{18}Ne. At the temperature expected for the break-out from the HCNO-cycle (0.4 < T_9 < 1.0), the direct contribution exceeds the combined yield of these resonances, while in later phases of hot novae or X-ray bursts (T_9 > 1.5), the high-lying resonance yield is more important than the yield from the direct process. However, at all but the highest temperatures of (T_9 > 2.5), the 6.15 MeV 1^- resonance dominates all other channels before the high-lying states take over. Therefore, one can conclude, that the direct contribution does not play an important role in the stellar production of ^{17}F at temperatures between 0.5 < T_9 < 3.0. The total combined yield falls almost on the solid curve marked "resonances" and is therefore not shown in Fig. 7.14. As long as the uncertainty in G_a for the E_x = 6.15 MeV resonance is large, the question of the phase of the direct (mostly 1^-) contribution relative to the 1^- resonances is of minor importance for <σv>. Below T_9 = 0.5, a strong interference term between the direct channel and the 6.15 MeV resonance contribution is predicted[25] by Hahn et al. Their G_a value of 2.3 eV for this state is well within our experimental uncertainty. With our slightly larger value of 3 eV, we get a about 1.5 times larger rate. However, given the uncertainties, their estimate is in excellent agreement with our measurement.

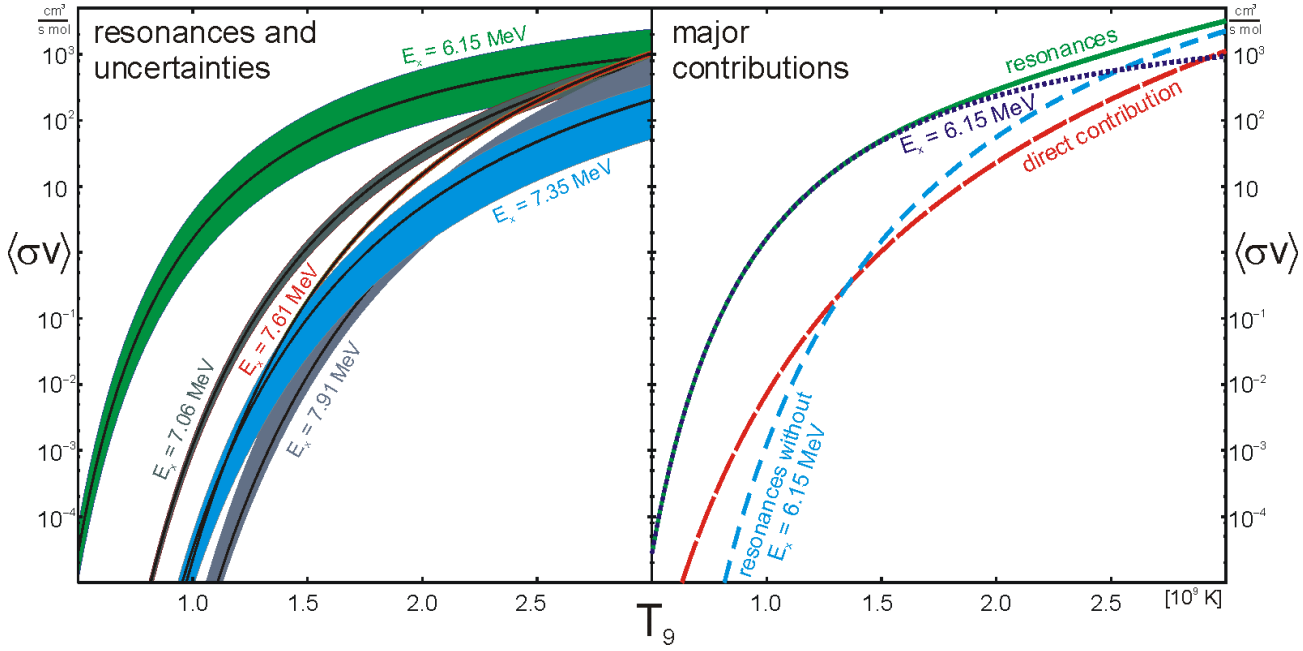

Fig. 7.14 Astrophysical reaction rates. Left: The independent resonances with error bands arising from the uncertainties in G_a, Right: The major contributions, i.e. the resonance at 6.15 MeV, all known resonances, all resonances in the range 7 MeV < E_x < 8 MeV and the direct contribution from Funck and Langanke.

For convenience, the Table 4 gives evaluated expressions for the respective resonant contributions to the reaction rate shown in Fig. 7.14. Since all terms are of the form

$$C_1\left(\frac{1}{T_9}\right)^{\frac{3}{2}} e^{\left(-\frac{C_2}{T9}\right)} \qquad (7.3)$$

only the coefficients C_1 and C_2 are given.

The 3^- state at E_x = 6.30 MeV, if present, was estimated[25] to have an alpha width G_a = 0.34 eV. Using this number, an additional term would result:

$$\langle sv \rangle_{6.29} = 6.74 \cdot 10^4 \left(\frac{1}{T_9} \right)^{\frac{3}{2}} e^{\left(-\frac{13.6}{T9} \right)} \tag{7.4}$$

This yield would be less important than the contribution of the 6.15 MeV resonance at lower temperatures and less important than the E_x = 7 MeV group of resonances at high temperatures.

Contribution to $\langle sv \rangle$ [cm^3 / (mol·s)]	C_1	C_2
1^- resonance at E_x = 6.15 MeV in ^{18}Ne	$2.7^{+4.2}_{-1.7} \cdot 10^5$	12.02
4^+ resonance at E_x = 7.06 MeV in ^{18}Ne	$7.58 \pm 2.3 \cdot 10^6$	22.6
(2^+) resonance at E_x = 7.35 MeV in ^{18}Ne	$6.04 \pm 4.5 \cdot 10^6$	25.9
1^- resonance at E_x = 7.61 MeV in ^{18}Ne	$8.43 \pm 0.9 \cdot 10^7$	29.0
$(1^-,3^-)$ resonance at E_x = 7.91 MeV in ^{18}Ne	$6.2^{+16.8}_{-2.5} \cdot 10^7$	32.4

Table 4 Resonant contributions to $\langle sv \rangle$ of ^{14}O(p,a)^{17}F

Comparing our work with the previously known information and assumptions, we find deviations in the assignments of the states in the 7 MeV region in ^{18}Ne. Especially the state at E_x = 7.35 MeV, previously assigned to be 1^- and now reassigned to be 2^+ with a much smaller *wg* has lost its astrophysical importance at temperatures above T_9 = 2. Supporting evidence for the quantitative calculations[25] on the astrophysical reaction rate of the ^{14}O(α,p)^{17}F reaction in the temperature range of $0.5 < T_9 < 2.0$ was found in a direct measurement.

7.5 What is left to do?

On the question of the ^{14}O(α,p)^{17}F reaction, an additional measurement determining G_a of the E_x = 6.15 MeV resonance in ^{18}Ne is required. With better statistics on this parameter and a verification of the assumption that $G_{p'} << G_p$ for the 6.15 MeV state, a reliable reaction rate over a large temperature range would be provided. To gain information on the expected rates at the lowest temperatures of $T_9 < 0.5$, a determination of the phase of the direct background in the vicinity of the resonance is required. The first of this two undertakings seems feasible with the technique described in this thesis, for the latter, a significantly stronger ^{17}F beam would be required to overcome the even lower cross-sections off resonance.

The next step would be to tackle the ^{18}Ne(α,p)^{21}Na reaction. We have already demonstrated the production of a ^{21}Na beam. This allows to use the system ^{21}Na + p in an analogous way as we used the ^{17}F + p configuration to determine G_a, G_p and the inelastic proton width. However, in this case, the sum of about 10 inelastic widths G_{pi}, corresponding to energetically accessible excited states in ^{21}Na, has to be determined together with a strength distribution in the inelastic channel.

The measurement of the ^{15}O(α,γ)^{19}Ne reaction with its narrow resonances is a particular experimental challenge. It would be the simplest to postpone it until the second generation radioactive beam facilities become operational, providing higher intensity beams of superb energy resolution. However, using an inventive, novel technique...

8 Appendix

8.1 Thanks

I would like to thank everybody on the following long (and still incomplete) list of people for their help and support for this thesis, for being good colleagues, for enduring my moods between enthusiasm for a new (not always good) idee and poorly concealed anger about setbacks. These people are / thanks to...

- ... my advisors Ernst Rehm and Hans-Joachim Körner of whom the first had to put up with me and my teasing of his VAX-centered worldview for the last four years and the latter who had not much benefit from sending me to Chicago besides that I could not screw up his computers here in Munich.
- ... Cheng Li Jiang who checked the analysis of all data presented in this thesis and who at least tried to keep me from attempting impossible experiments.
- ... John Schiffer who always forced me to explain *exactly*, why I wanted to do something, taught me physics and did calculations, that would have been my business to do.
- ... Michael Paul for coming to my experiments all the way from Israel, for LN_2-frozen bananas and all the other fun we had during the experiments.
- ... Richard Pardo who did the transport part of the calculations used to predict the secondary beam intensity and managed to actually tune the beast onto target, usually at about 4 a.m.
- ... Thomas Faestermann for reading through this thesis and patiently answering my questions while writing it.
- ... Robert Janssens for a lot of practical advice, help with our beam times and (!) BBQed Burgers on his famous 4^{th} of July celebrations.
- ... Ingo Wiedenhöver who helped with the electronics of way too many channels of silicon.
- ... John Greene, who made not only our targets but first of all spent a combined two months of his life making windows for the gas cells and did a substantial part of the development of the (tricky) window mounting technique.
- ... Irshad Ahmad for providing radioactive sources and for a lot of answers to questions concerning radiation safety and gamma detection.
- ... Tsu-Fang Wang, now at LLNL, who was the first at ANL to have the idea for our beam production technique and who came many times from California to Illinois, just to see "it" happen.
- ... Bruce Zabransky, who did not only the mechanical engineering of the cells and the movable solenoid mount but also patiently explained to me once a week which number-something screw matched which drill and where to find both of them.
- ... Jim Specht and Bruce Nardi of whom the first build an actually working automatic liquid-helium and LN_2 refill system for the superconducting solenoid and the gas cells and the latter for building and programming the electronic controller for it.

- ... Dale Henderson and Tad Pennington who had to suffer through several broken detector windows and always somehow, somewhere found the parts to build jet another gas handling system. Without Dale's experience, the annular Bragg counter would never have worked.
- ... Ken Teh, our UNIX-wizard, for lending a hand in computer questions even through my Microsoft text processor kept renaming him "Ken The".
- ... Phil Wilt, who did a great job building my real-time 10 MHz multi-channel analyzer for beam tuning
- ... John Rohrer and Jim Joswick who not only helped to set up the hardware of our primary target assembly, but also put up with the regular disappearance of turbo pump carts, gaskets and O-rings from their stock.
- ... Tom Mullen and the health physics team who always remained helpful and friendly in the face of hydrogen bombs and loose contamination in the beam-line.
- ... Garry Zinkan and the accelerator team which did their best to make our experiments work even through we produced "a big mess" in the beam-line tunnel, lovingly dubbed "the submarine" for being absolutely inaccessible after we put in the gas cell.

Finally, a big thanks to and all the people who helped in the beam times and are not listed above: Alan Chen, Alexandro Sonzogni, Andreas Heinz, Francesca Borasi, Jack Caggiano, Jeff Blackmon, Juha Uusitalo, Michael Smith, Peter Parker, Ralf Segel and Rolf Siemssen.

8.2 Documentation for the Monte Carlo Package.

The Source code of the program is available from the author on request. The following is the readme.txt -file distributed with the code.

```
                    *** S O U R C E  and  D E T E C T O R S ***
                                and some related tools

A 3D-Monte Carlo (MC) system for two particle reactions in a layered target with a set
of user defined detectors. The two-particle restriction might fall in a later version,
parts of the system can already handle more particles.

1 GENERAL CONCEPT
=================

"Source" produces table, in which every line represents one event of a user defined
reaction in a three layer user defined target or simulates a Source, like e.g. and Al-
pha source. This output can be used directly, or filtered by the tool Gates. A
satisfactory  output file can be plotted(e.g. with GNUPOLT), histogrammed by Hist, or
passed on to Detectors, that will read the input file and test each event for hits in
the detectors. It outputs a file similar to that of Source, now including information
about positions of hits in absolute coordinates or strip- and detector numbers. Again,
the output can be filtered with Gates, plotted with GNUPOLT, and histogrammed with
Hist.

It should be mentioned, that awk (or the GNU version of it,  gawk) work fine with this
files, which provides additional freedom to manipulate the events (calibration, change
of units, sum-energies, ... ).

2 SOURCE
========

Source is the first program in the chain of tools described here. It provides the "raw"
events, that can be processed to closer resemble the data actually measured  in the
detectors of the experiment. The Monte Carlo simulation is based on reaction kinematics
and Zieglers stopping power formulas. The straggling algorithm used is based on semi
empiric equations, that provide reasonable results for most cases.  However, especially
to obtain a better energy and angle straggling, it is possible to calibrate these func-
tions by "Fudge Factors", that can be obtained by  running e.g. TRIM or fitting
experimental data. For performance reasons,  the position of the particles is simulated
in a cruder way, (only one step per layer with some empirical correction function) and
will be unreliable for large angles and thick targets. For thin targets like foils or
for thick targets but small angles, the simulation should be ok.

The outline of Source's function: Source reads a reaction definition file (RDF), and
runs a number of particles through this system. For each incident beam particle, a line
of output is send to the UNIX standard output device (stdout), i.e. the terminal, if
not redirected. The contents of the line is controlled by a string "TableComString",
that lists the parameters (like energy or angle) of the products and/or the individual
beam particle, that are desired. The name of the RDF and how many particles are used,
some basic parameters of the incident beam are controlled by the command line. Addi-
tional parameters of the simulation as well as of the output (like units) can be
supplied optionally via switches.

Besides the RDF, there are other (optional) input files, that can be used to define an
angular distribution of a reaction, the precise energy profile of the beam or its angu-
lar spread. Unlike the RDF, which is a well commented file, these input files are
merely dumped arrays of fixed length, and should be produced by some suitable software
(like a 5-liner my the user, a shell-script or a spread-sheet program with capabilities
to export ASCII)
```

```
2.1 SYNTAX AND PARAMETERS:
--------------------------

Source [-switches] TableComString ReaFName #_Particles EBeam dEBeam dABeam

All parameters, except for switches, MUST be provided. "Zeros"(e.g. for dEbeam) are not
recommended, since I did NOT debug for such cases. Since a lot of people like to see
examples first, I provide some simple ones here:

examples:    Assuming, that the RDF "16Odn17F.reak" contains information about
             the inverse 16O(d,n)17F reaction, i.e. the target is 2H-gas or CD2.

   Source 3e3t 16Odn17F.reak 10 80 .01 .01

             a two column table (energy and angle) of the reaction product (17F) with
             10 lines, calculated according to the target and reaction definition in
             the file "16Odn17F.reak"

   Source -B 0.5 -GRd 3e3t4e4t 16Odn17F.reak 100 80 .01 .01 >

            Similar, but with an extended beam-spot of 0.5 mm (one sigma)
            radius, Gaussian distribution of beam particles. The table now
            has 100 lines and includes also the second reaction product
            (neutron).
            The output of the polar angles is now in degree (-d). Note, that
            the -B switch was put separately. "-GRTdB 0.5 " would have also
            worked, but NOT "-GRTBd 0.5 ". Switches with parameters have to
            be last. That can cause erratic error messages, since the scanner
            might not discover the problem until processing a later parameter.

    Source 3H3S4S 17FCH2a14O.reak 100 80 .01 .01

            Simulating the 17F(p,alpha)14O reaction in a CH2 target,
            this produces the required output for the program Detectors
            (see below) to detect coincidences in a detector array. The 3H
            (CM angle at birth) will be ignored by Detectors, and can
            be used to generate a plot, that shows, which Detector Strips
            relate to what CM-angles.

2.1.1 Switches
--------------

Here is a complete list of all switches:

 v  Be wordy about the internal parameters
 R  Beam spot round (instead of square)
 G  Beam spot gaussian (instead of a flat distribution)
 B <size> define the size/radius of an extended beam spot in mm,
    either the limits or one sigma, depending, if the -G option
    is active.
 d  Output all polar angles (theta) in degree
 D  Output all angle in degree
 r{GW|GO|FW|FO} <double> parameters for random number output:
   rGO <Centroid of Gaussian>
   rGW <Sigma of Gaussian, about 0.43 * FWHM>
   rFO <Center value of flat random distribution>
   rFW <Max. deviation from Origin>
 m  All output of the dimension length in mm
    (instead of the default cm)
 s  <iseed > sets an iseed for the random number generator
    (positive integer)
 z  If a product particle is stopped in the detector, zero all its
```

```
    parameters, and the output of the <PartNr.>S-comand is completely
    suppressed.
 x  Save the internally generated cross section array XS(E) to
    "EXSDist.out"
 a  Save the initial beam angular distribution to file "ABeamDist.out"
 A  Load the initial beam angular distribution from file
    "ABeamDist.dat"
 e  Save the initial beam energy profile as used for the MC to
    "EBeamDist.out"
 E  Load an beam energy profile from file "EBEamDist.dat"
 W  Load ADist XS(Om) and convert internally to XS(th) from file
    "dSdWCMDist.dat"
    (note, that this file should be the cross-sections dSigma/dOmega,
     so they are, in general, NOT zero at zero/180 degree).

     Format of the file :
       3600 lines:
         angle (beginning of bin) <WhiteSpace> RelativeValue
       for example:
       ================= BOF ==================
       0       4.600000
         .
         .  (3598 more lines)
         .
       3.14072 0.600003
       ================= EOF ==================

       (the BOF/EOF line are not text of the file)

 t  Save ADist XS(th) save file "dSdTCMDist.out"
 T  Load ADist XS(th) from file "dSdWCMDist.dat"
    (note that this distribution should go to zero for zero and 180
     degree. HOWEVER, Source does not enforce such a rule.
    Format: As in the case of the -W switch for "dSdWCMDist.dat"

The distribution files mentioned (.dat o .out) here have all the same structure:

    x y data-points (x equally spaced).
      The beam distributions have 512 elements.
      The angular- and energetic cross-sections have 3600 elements.

2.1.2 Commands for table output, the format of the TableComString
-----------------------------------------------------------------

The TableComString list a row of independently evaluated parameters of one to (at pres-
ent) 2 letters, that correspond each (with exception of {2|3|4}S) to one column in the
output table. A table string of "3e4e", for example, will result in a table of two col-
umns and #_Particles events lines, the first column being the third, and the second
column the forth particles energy after leaving the target. There are no spaces allowed
in-between the entries, repetitions are allowed.

 Format: Entry[Entries]

         Before each Entry, a single dot '.' is allowed (but not required)
         to increase readability of the command string. Only some dots
         can be used, but no dot after the last entry is accepted.

The most important group of commands provides information on particles 2 (the projec-
tile), 3 (the product) and 4 (the "other" product/residual). In this sense 2,3 or 4 is
the number of the particle Pn in a reaction of the type P1(P2,P3)P4. The following com-
mands are therefore all start with one of this numbers and then the letter given below.
Note, that particle 2 disappears in the reaction. Therefore, the letters have a differ-
ent meaning then for particle 3 and 4.
```

```
   e  Energy after the target (MeV)    (2e: at the reaction point)
         stopped particles: Disregard!
         uncharged particle: After reaction!
   t  Polar angle theta (RAD/deg)      (2t: at the reaction point)
         stopped particles: Disregard!
         uncharged particle: After reaction!
   p  Atzimuthal angle Phi (RAD/deg)   (2p: at the reaction point)
         stopped particles: Disregard!
         uncharged particle: After reaction!
   s  Atomic charge of particle, randomly chosen according to Robinett/
      Bobinette and Baron & Delaunay PRA 12(1975)40. The target correction
      (from the 12C optimized code) done assuming, that the charge state
      equilibrium is dominated by the first element given in the
      passive layer definition on the respective side of exiting the
      target. For details, see the RDF file explanation.
   E  Energy after reaction   (2E: before the target)
   T  Theta (RAD/deg) born, measured relative to the direction of
      flight of particle 2 in the moment of reaction. For one reaction
      energy, 3T vs. E3 is the kinematic parabola without any straggling
      effects. (2T: Angle of incident beam particle before interaction
      with the target)
   P  Phi in the system of moving particle 2 at moment of
      birth. Corresponds to 3T,4T commands, 3T-4T = PI/-PI. (RAD/deg)
      (2P: Phi of beam particle hitting the target)
   H  Angle theta in the Center of Mass at moment of birth,
      corresponds to the T-command (RAD/deg).
      (3T: Always 0)
   x,y,z Last position in target [CM/mm]. For uncharged particles and
         particle 2 always the reaction point. i.e. 2zxy = 4xyz for an
         uncharged particle 4 (a neutron). For a charged particle, the
         Z component is always the location of the first or the last
         surface of the target.
           Stopped particles: Disregard!
   X,Y,Z Last x-y-z component of the particles DIRECTION. Behaves as
         a unit vector pointing in direction given by p,t, which are
         defined as described above.
   r  Radius of the particle measured from the beam axis at last
      target layer.
   v  v/c0, calculated from e-parameter.
   f  flight-time of the particle, measured. The moment of the incident
      particle hitting the 1st target layer defines T=0. Please not, that
      the time  parameter is a crude measure, derived from linear middle
      velocities and linear distances in each layer.
      (i.e.: dT,layer= sqrt((x1-x0)^2+(y1-....) / ((v0+v1)/2))
   m  Mass of the particle in amu
   n  Nuclear charge (Z) of the particle in e+
   S  short for com's 'Lemntpxyz', but always in cm and rad, with no
      regard to switch settings like -m or -D. Used to generate output
      for the program Detectors (see way, way below!)

The following commands don't have a number in front of them, but are related to one of
the particles, Nr. 2:

  x,y,z  Position of beam particle hitting target where z is always
         zero (the position of the entrance window.

 The last group inserts non-particle related columns in the output file:

  L  Print a "|" (vertical line) in the middle of that column.
  r{G|F} Random number (Gaussian or linear).
    rG:  A number randomly generated using a Gaussian distribution
         centered around the origin and with a sigma defined by the
```

```
          -rGW and -rGO switches, see above. The defaults are 1 for
          Sigma => FWHM about 2.36, and centroid around 0.
          The maximum/minimum value, however is Centroid +/- 5 Sigma.
     rF:  A homogeneously distributed random number around the origin
          and with a width defined by the -rFW and -rFO switches. Defaults
          are the width 1 around the origin 0, allowing for values
          between -0.5 and +0.5.
```

Note, that Source (since a lot of numerics and stepping over distributions is involved) is fairly slow compared with Detectors and especially tools like awk, Hist or Gates. For several thousand events, it might make sense to include more parameters than needed for one particular plot in the output in order to avoid a re-run for the next plot.

2.1.3 The Parameter #_Particles, EBeam, dEBeam and dABeam

These parameters must be supplied to Source. They have to following meaning:

#_Particles	The number of particles thrown at the target. Zero is a permissible value, and results in no calculations performed. However, since the initialization is performed, switches like -x (dump the created cross-sections XS(E)) work.
EBeam [MeV]	The beam energy in MeV, it should not be zero.
dEBeam [MeV]	One Sigma of the gaussian energy distribution of the beam, resulting in a spectrum with a FWHM of about 2.36 times dEBeam
dABeam [deg]	The probability distribution to create a primary particle with a certain incident angle is created by using a gaussian distribution with dABeam as sigma, that is then multiplied by the Angle itself and finally normalized. This is an approximation for Gauss(Angle)*sin(Angle) for small angles.

2.2 STRUCTURE OF THE REACTION DEFINITON FILE (RDF)

The RDF is a plain text file, that is designed to be (reasonably) readable by humans, i.e. it allows for comments and so on. It is read at the start of Source and the source of most of its parameters describing the reaction and all the parameters describing the target. The target consists of three layers, of which only the middle one permits reactions. However, straggling and particle tracing is done for all the layers. It is assumed, that the particle enters the target from the Layer-One side (z = 0) and proceeds through the material. The reaction is modeled as a two-body process (reaction or decay) and allows for adjustment of Q-values etc.

The following (between the lines of star (*)) is a syntactically correct RDF with lots of comments to explain the entries:

```
**************************************************************************

Reaction file for Source:   d(16O,17F)n

 This text will not be interpreted by Source since it is before the
 keyword "B..." in the next line (can't write it here, that would
 trigger the interpreter!):

BEGIN

! projectile  (this line is a comment and will not be interpreted,
! since it starts with an exclamation mark (!).
!   Note, that Source knows masses and nuclear charges of all stable
```

```
!   and most known unstable isotopes.

16O

! A line "DC" after the definition of the beam indicates, that the
! particle decays instead of reacting with the target. This is
! implemented by assuming a zero-energy gamma target!

! DC          (here commented away, since we want a reaction!)

! A single line "SM" will switch off all processes before the decay
! and create a parent nuclei evenly distributed in layer 2. This
! Source Mode is  only valid after DC, otherwise, an error message will
! be displayed (Source will interpret "SM" as the element samarium, and
! complain about the missing isotopic mass)

! SM         (here commented away, since we want a reaction!)

! observed particle 3, the ejectile, in T(P,E)Residual

17F

! ============ 1st layer, HAVAR ============== !
! In seperate line:
!   * First the material,
!       Note, that the numbers before the brackets are molar
!       contributions to the material, that have to be integer.
!       Note also, that isotopes can be given (60Ni), but are not
!       needed. If no isotope is given, the natural isotope mix
!       (average mass) is assumed.
!   * The thickness in mg/cm**2
!   * The physical length [mm].

42(Co)20(Cr)13(60Ni) 1.9 0.01

! Note, that the first element herein will be used to correct the
! atomic charge of an ion leaving the target in this (backward)
! direction, passing through this window. In this case, the correction
! would be done for Z = 27 (Cobalt). See also the comment on the 3rd layer.

! Straggling normalization for 1st layer for particles 2 to 4 in the
! format:
! NrOfPar  ThicknessCompare[mg/cm^2] ECompare[MeV] AValue[deg] EValue[MeV]
!                                                    1 Sigma      1 Sigma
! The procedure works like this: Fit the "real" distribution with a
! gaussian (energy case) or an gaussian times sin(angle) for the angle
! case for particles with an energy as close as possible to the energies
! involved here (real means a high-quality simulation or measured data).
! Enter the values found in degree and MeV after the number of the
! particle (2-4) each in one line.

2 1.0 90.0 0.3294 0.1297
3 1.0 60.0 0.5987 0.1584   ! not really needed; products go forward!
! 4 is the neutron, don't give a value!

ENDLAYER

! ========== Gas Target: 2H ============== !
! First the material, then the thickness in mg/cm**2, then
! the physical length [mm]
! All the same as above, except that the first element of the
! target compound HAS to have an isotopic mass, since this is by
! definition the particle "1" in 1(2,3)4 of the reaction.
```

```
1(2h) 1.6 35

! Straggling normalization for 2nd layer for particles 2 to 4 in the
! format
! NrOfPar ThicknessCompare[mg/cm^2] ECompare[MeV] AValue[deg] EValue[MeV]

2 1.0 80.0 0.1278  0.08705
3 1.0 70.0 0.1633  0.08897
! 4 is the neutron, don't give a value!

! the next line indicates, that you are done with corrections. It has
! to be present, even if there are no corrections made (which is good
! for most cases!!)

ENDLAYER

! ============ 3rd layer, HAVAR ============== !
! First the material, then the thickness in mg/cm**2,
! then the physical length [mm]
! (all the same as layer 1)

1(C)420(Co)200(Cr)130(Ni) 1.9 0.01

! Note, that a minimal contribution of carbon was added as first component
! of the target. This will simulate a thin carbon stripper foil after the
! gas target of this example, since the charge states will be corrected
! for the 1st target component, here for Z=6 (carbon)

! Straggling normalization for 2nd layer for particles 2 to 4 in the
! format
! NrOfPar ThicknessCompare[mg/cm^2] ECompare[MeV] AValue[deg] EValue[MeV]

! 2 Not necessary: Primary ions don't leave target in this simulation
! (100% reaction rate!)

3 1.0 60.0 0.5987 0.1584

! 4 is the neutron, don't give a value!

ENDLAYER

! ========= Q- Value correction/excitation for the reaction ==========

! Q-Value: Give an EXCITATION to the mass value from the database,
! and assign it to a particle (all four particles can be excited). To
! correct a wrong Q-value in the database, you can also assign a
! "negative" excitation to a particle. Note, that positive values of
! the products and negative values of the projectile/target correspond
! to more negative Q-values.

! 1 37.89999
! 2 0.0
! 3 0.495
4 0.0

! (none of the lines above has any effect. The first three, since they are
! commented away, and the 4th one because, the value (0) is the default.
! Note that the third one, without the comment (!), would simulate the
! (dominant!) production of 17F in the 1st excited state instead of the
! ground state.

ENDQ
```

```
! ========== Definition of the X-section for the reaction ===========
!
! The following keyword starts the interpretation of the cross
! section information XS(E) of the reaction. Note, that it is not done
! in an array of fixed length and step width as in the case of angular
! distributions  XS(Theta), but in data-points, that are then used to
! generate such an array internally. I felt that angular distributions
! would be generated by Legendre Polynomials, so the user can easily
! provide an array type input, while here measured data points would
! be used more commonly.
!
! PS: Why did I include XS(E) in this file, but not XS(Theta?). Because
!     XS(Theta) can change rapidly with energy, I thought, it would be
!     simpler to supply this information, if needed, for the energy
!     of interest.

CROSSSECTION

! In which system are the data-points measured? In the system of the
!
! T    = target, here 2H, which is the lab system for this reaction
! C    = Center of Mass System
! P    = Projectile System, which is here 16O.
!
! The data below was measured in "normal" kinematics (d,n),
! which is the projectile system for our reaction, that is inverse.

P

! First, the units of X-section and then, in a new line,
! the unist of the Energy.
! Accepted units are:
!    b = barn or mb 0 millibarn and
!    MeV      or eV

mb MeV

! Energy-Range of the X-Section-section !  ! For technical reasons, I
want to have the energy of the first and the ! last data point ahed of
the data itself!

2.15 16.0

! Data points from the Landolt-Boernstein compilation.
! You have to provide at least two, and they have to cover the energy
! range of interest for the reaction. Note that the magnitude of XS(E)
! plays no role in the Monte Carlo simulation. However, the next
! version of Source will probably inform about expected total yields
! by once integrating over the region of interest.

2.15   65
2.2    95
2.27  105
2.30  130
2.35  100
2.45   95
2.57  115
2.63  150
2.7   170
2.78  195
2.9   200
2.95  190
```

```
3.00  150
3.1   400
3.5   375
3.6   400
4.0   410
4.5   450
5.0   500
6.0   470
6.5   420
7.0   460
7.5   420
8.0   400
10.0  280
16.0  150

! indicate the end of the list of cross-sections and the end of this
! file by the keyword STOP:

STOP

This line will not be interpreted by Source... (its after STOP)

*************************************************************************
```

Note, that the lines with the stars (*) are not part of the RDF! This concludes the description of Source.

3 DETECTORS ===========

Detectors is a tool, that reads either from the standard input or a given input file data of particles, where up to six coincident particles (from one nucl. reaction?) are organized in one line. Particles are born at individual points in space, have nuclear charge and energy and a direction in space relative to the z-axis of the system.

Detectors takes its information about the geometry and material make-up of the detectors from a detector definition file (DDF), in which strip detectors, annular (strip) detectors and circular detectors can be defined. Each particle is tested for hits in one of the detectors, and disappears at the moment of interaction (later versions might be able to transmit particles!).

For each event, a line with one or more particles in the input file, a line of an output table is generated. The composition of this line can be controlled much as in the case of the program Source discussed above. A TableComString contains a sequence of tokens, of which each represents one (or a few) output columns. The output table is supposed to be redirected into a file or piped into a filter tool like Gates, a histogramming tool like Hist or to be directely plotted with GNUPLOT.

While Detectors does not have extensive Gating capabilities on its own, it allows to define a multiplicity level, and to suppresses output of all lines, that don't reach this level.

3.1 SYNTAX AND PARAMETERS ------------------------

Detectors -switches TableComString

Detectors need only one parameter, the TableComString. The switches influence only the input/output of the program, but not the way, it performs its operation.

EXAMPLE: Detectors -C 2 -I mc/dn.dat 1e1t1x1y1z0x0y0z > mc/dn.DET

3.1.1 Switches

```
 --------------

 v             be wordy about the parameters and detectors.
               A table of the detector's parameter is printed.
 C <CoinLevel> require coincidence level <CoinLevel> for output
               0 prints all events, 1 events with one hits or more
               and so on
 D <DetFile>   Use det. file <DetFile> instead of 'detectors.dat'
 I <InFile>    Use Input file <InFile> instead of stdin
 S             Do hit spectra and output them to stdout
 t             Don't generate tables, disregarding TableComString
```

3.1.2 The TableComString

As in the case of the program Source, the TableComString is a sequence of independent Tokens, that each prompt Detectors to add one (or more) columns to the output table, that is printed to the standard output. Again, there are no blanks etc. allowed in the string.

```
 Format: Entry[Entrys]

         Before each Entry, a single dot '.' is allowed (but not required)
         to increase readability of the command string. Only some dots
         can be used, but no dot after the last entry is accepted.
```

The first group of entries starts, again as in the case of Source, with a number, that represents the number of the individual particle in the event line of the input. HOWEVER, the numbers in general don't match the numbers from Source, but merely reflect the order of particles in the event as passed to Detectors. If you see lots of zeros in the output, you probably used the typical numbers ("3" and "4" for the products) from Source. You should have used "0" and "1". The commands are

(0-5)<letter>, where letter is:

```
 T  flight time between the spot of origin to the spot of interaction [ns].
 e  Energy
 v  velocity in units of C0.
 t  Theta, the polar angle [rad]
 p  Phi, the azimuthal angle [rad]
 x,y,z last position in Cartesian coordinates [cm]
          Not defined for non-interacting particles, otherwise the
          point in space, where the particle hit a detector.
 X,Y,Z last x,y,z component of the direction of movement.
          Not defined for non-interacting particles, otherwise the
          direction that the particle had, when it hit a detector.
 m  Mass of the particle [amu]
 n  Nuclear charge Z of the particle [e+]
```

in the (0-5)<letter>-command group, a subclass is defined for the interaction of charged (and so far only charged) particles with the detectors. These commands start with

```
 D<letters>, where letter is:

 d  number of the detector hit, starting with 0 (!)
          The number is assigned according to the order of definition
          of the detectors in the DDF. -1 is issued, if no detector
          was hit, or the particle does not exist.
 s  Strip number that was hit.
          Strip numbers start with 1, O is returned, if no strip was
          hit.
```

```
 a   The incident angle of the particle on the detector plain, measured from
     the detector plain, i.e. PI/2 is a perpendicular hit.
 DL<0-9><letter>
     commands to calculate the responds of a detector, based on Ziegler-tables
     for energy loss. These letters are:
 e   The energy loss in the layer => the energy signal from this layer
 p   The maximum stopping power, that the particle encounter in this
     layer => Bragg-Peak, if the particle has the right energy range.
 r   the range of the particle in the detector material. For convenience,
     the stopping range of the ion is subtracted from the thickness
     of the layer [mg/cm**2] divided by the sin() of the particles
     angle (as given by the Da-command).

     NOTE: The first layer has the number 0!

  NOTE: If no particle with the specified number exists, zeros are printed,
        one for each parameter except for the Detector number, which is set
        to -1 for convenience. That allows to create easy plotable files
        with fixed colum numbers while using input files with variable
        numbers of parameters per event. Be aware so, that if not always
        the same particle is missing (eg. product 3 or product 4 for is
        stopped in the production target), a mixing of product types might
        occur.


 The second group of commands does not have a leading number, but
 consists of only one letter.

 l  Echo the complete input line.
          Transport the whole input file to the output file, and just
          add some columns or even only filter for hits without adding
          further information.
 b  Echo ignored leading part of input line (before first '|').
          This allows to transport a few columns from Source
          (e.g. CM-angle)
          through Detectors without producing a huge table, that would
          from the use of the "l" command.
 L  A vertical line symbol '|'
```

3.2 THE INPUT FILE FORMAT

The input file is read by default from the standard input, but can also use a file in the file system (see -I switch). The line of the input file have this structure:

```
   Ignored Part  Particle[0]                    Particle[1]....   (up to 6)
   <"any" text> '|' E M Z Theta Phi X0 Y0 Z0 { '|' E M Z Theta Phi X0 Y0 Z0 }
          double:   ^ ^   ^     ^   ^  ^  ^
         integer:       ^
            UNIT:   MeV       amu e+     rad rad    mm mm mm
                  (P.Data)  (Part.ID)  (Movement)  (Origin)
```

It is important to note, that the ignored part can contain any text EXCEPT the vertical line symbol "|", since that triggers the data acquisition cycle of Detectors. The ignored part can be used for output of Source (or any other tool for that matter) to be passed through Detectors without processing, using the -b switch. It is important (for your comfort) to note, that Source produces exactly the sequence needed for one particle with the nS command, see above).

3.3 THE DETECTOR FILE FORMAT

As in the case of Source, the detector Definition File (DDF) of Detectors is rather readable. Unfortunately, some of the information needed, which are points in space, that describe corners of detectors, are a little cumbersome to calculate. I recommend a spread sheet tool like MS Excel or so to help you do it right. Again, I think that a well commented but actually syntactically correct file is more helpful than a description of the file in detail.

```
**********************************************************************

 *** Detector Definition File (DDF) for Detectors ***

This file contains the parameters for the detectors used
in a p(17F,Alpha)14O , p(17F,17F*)p' and p(17F,17F)p
experiment. The setup consists of a CH2 target, all
reaction products go forward in the laboratory system.
The light particles (alphas and protons) are detected
in large area silicon strip detectors:
There are two annular silicon ring detectors, (inner
radius 2.4 cm, outer radius 4.8 cm), each with
16 rings of 1.5mm radial diameter, around the beam axis
and 6 silicon strip detectors (5x5cm, 25 2mm strips),
that are attached on the outer radius of the first
silicon ring detectors. The latter are tilted under an
angle of 35.3deg towards the target. (90deg + 35.3deg
from the beam axis as z-axis).
The silicon ring detectors are 500mue and 1000mue thick,
the strip detectors are 300 mue thick.
The heavy ions are detected in an annular ionization
chamber (Donut shaped, with a hole in the middle!),
with a PPAC on the front. We will take the PPAC wire
plane as z-position of this detector, and assume no
angular position resolution. It has an inner active
radius of 0.92cm (yes, pretty small hole!), and an
outer active radius of 5.08 cm. The make-up of the
PPAC and ion chamber is: 1.5mue MYLAR foil, 1cm/2torr
Isobutane gas, 1.5mue MYLAR foil, 2.5 mue MYLAR foil,
about 3" freon gas at 350 torr.


This is a rough sketch
of a cut along the z-axis, showing only the to and
bottom strip detector:

 Y
 ^
 :       \ Upper Si-Strip-Det.
 :        \/
 :         \              2nd Ring Det
 :          |           |/             |P|----------|
 :          |           |              |P| Ion      |
            |           |              |A|  Chamber |
Target                                |C|----------|
 |
 |-------------------------------------------------> Z
 |
                                       |P|----------|
            | 1st Ring  |              |P|          |
            |/          |              |A|          |
            |           |              |C|----------|
           /
          /\
         /  Lower Si-Strip Det.
```

```
  (The X-axis points into the plane, away from you)


The following line triggers the interpreter, from now on,
commenting text has to be "commented away" with an
exclamation mark (!) in the first position of the line.

BEGIN

! Since the program source does not allow to redefine
! its coordinates, Detectors got this ability. We Define
! the origin of the system with respect of the system of
! the incoming particles first. All coordinates are in
! cm, measured with respect to this (x y z) origin.

0.0 0.0 0.0

! NOW follows a list of the detectors used.
! It has a format, consisting of a first line to describe
! the geometry, which is then followed by a number of up to
! 10 lines for 10 different (infinitely thin!)detector layers.
! The geometry definition has this format:
!
!       Center:     Point1:     Point2:     Strip Data:
! Type  CX CY CZ  P1X P1Y P1Z  P2Y P2X P2Z  Width NStrips
!   |   --------------------v-------------------    |
! (Char)                  (real)                (integer)
!
! Type                's', 'a', or 'c' accordingly
!                     s = strip detector,
!                     a = annular strip detector (round with hole)
!                     c = circular detector (a round detector)
!
! Center x, y, and z  this is either
!                        a,c: the center of the detector
!                        s:   1st corner (basis corner) of the
!                             strip detector
! Point1 x, y, z      this is a point on
!                        c: the edge of the circular detector,
!                        a: the INNER hole of the annular detector
!                        s: A close corner of the strip detector
!                           (NOT the diagonal one to "Center")
!                           NOTE: The strips will lie normal to
!                           the line defined by the points
!                           "Center" and "Point1", strip 1
!                           is the closest to "Center".
! Point2 x, y, z      similar as Point1, but:
!                        c: A point on the edge of the circular
!                           detector, 90deg turned.
!                        a: A point on the INNER hole of the
!                           annular detector, 90deg turned
!                        s: The 3rd corner of the strip detector,
!                           that is NOT the diagonal one of Center,
!                           BUT IS the diagonal one of Point1.
!                           NOTE!!! The strips will lie parallel to
!                           the line defined by the points
!                           "Center" and "Point2". This line
!                           is the outer border of strip 1.
!
! Width               width of the strips or rings, a dummy for c
! NStrips             number of strips or rings, a dummy for c
!
! The layer definitions have the format
```

```
!
! <Thickness [mg/cm**2> <material>,
!
! where the thickness is simply a (floating point) number, integers
! also ok, and the material is defined as in Source, e.g. 1(C)2(2H)
! for deuteriated PE foil, 1(Si) for silicon and so on. Note, that
! this information is optional. A detector without thickness is still
! hit by particles, and the energy loss in it is zero. Layers higher
! than the last defined layer behave accordingly.
!
! We start with the first detectors along the flight path
! of the particles from the target. That ensures, that the
! these detectors shadow the detectors behind them, and not
! vice versa! There is no test done, which one is really hit
! first. The definition is that the detectors are processed
! in order of appearance in this file and are numbered this
! way, starting from 0.

! In our case, these are the strip detectors. To calculate
! the corners of the detectors, it is highly recommended to
! use a spread sheet like Excel. In this case, I calculated
! the points of the first (upright) detector by hand, and the
! rotated the points in 60deg increments using MS Excel. If
! the table is done in a format similar to the input format
! for detector lines, a cut & paste does the trick to get
! the values in here.
! Debugging will be described later.

! Detectors 0 - 5, 23.6-47.1 deg, 300mue Si-counters with
! a thin dead layer of SiO

! Det. 3 is up, 4 is phi=60deg, 5is phi=120deg and so on
! counterclockwise around the Z-Axis, measured from
! the Y-axis. The far edge of the detectors is at 11cm
! from the target while the close corner is at
! 11-sin(35.3)*5cm

s -2.5         4.8          11  -2.5           8.879         8.108  2.5           4.8
11  0.2 25
 0.01 1(Si)1(O)
70.0  1(Si)
s   2.906921939   4.565063509  11     6.439439561   6.604563509   8.108   5.406921938
0.234936488  11  0.2 25
 0.01 1(Si)1(O)
70.0  1(Si)
s  5.406921938     0.234936492 11    8.93943956   -2.274436493   8.108   2.906921937 -
4.56506351   11  0.2 25
 0.01 1(Si)1(O)
70.0  1(Si)
s   2.499999998  -4.800000001  11     2.499999996  -8.879000001   8.108  -2.500000002  -
4.799999999  11  0.2 25
 0.01 1(Si)1(O)
70.0  1(Si)
s  -2.906921941  -4.565063509  11    -6.439439564  -6.604563506   8.108  -5.406921938  -
0.234936488  11  0.2 25
 0.01 1(Si)1(O)
70.0  1(Si)
s  -5.406921938    0.234936494  11    -8.939439559    2.274436497   8.108  -2.906921935
4.565063511  11  0.2 25
 0.01 1(Si)1(O)
70.0  1(Si)

! Now for the annular Si detectors, first the one, that
```

```
! connects to the strip detectors above, since it is closer
! to the target. The first one is 500mue thick.

! Detector 6, 12.3-23.6 deg

a 0.0 0.0 11.0   2.4 0.0 11.0   0.0 2.4 11.0   0.15 16
  0.01 1(Si)1(O)
116.6  1(Si)

! And the other one, 1000 mue thick
! Detector 7, 7-13.8 deg

a 0.0 0.0 19.5   2.4 0.0 19.5   0.0 2.4 19.5   0.15 16
  0.01 1(Si)1(O)
233.3  1(Si)

! We finish with the doughnut-shaped ion chamber, which we
! represent as a single round strip around the z-axis.
! With the inner active radius of 0.93 and the outer radius
! of 5.08 cm, we have a 5.08 cm -0.93 cm = 4.15 cm "strip"

! Detector 8, 1.5-8.2 deg

a 0.0 0.0 35.0  0.93 0.0 35.0  0.0 0.93 35.0  4.15 1
0.21 10(c)8(h)4(o)
0.007 4(C)10(H)
0.21 10(c)8(h)4(o)
0.35 10(c)8(h)4(o)
12.8 4(F)1(C)

! Note, that this is a demo. Of course, the accuracy of the
! calculation does not justify to include e.g. the gas of the
! PPAC, and one could simply combine the first 4 layers in a
! 0.77 mg/cm**2 strong MYLAR foil. That would also speed up
! the program, since a lot less layers need to be calculated


! Finally, a line STOP tells Detectors to stop looking for
! more detectors in this file...

STOP

... and all text after STOP is ignored, like in front of
BEGIN. Even keywords, as you can see.

**********************************************************************

This (without the lines of stars (*)) ends the DDF, used as an
example here.

Finally a HINT for debugging the DDF, once the Syntax-Errors are removed.
Use Source with an isotropic Reaction like proton scattering on gold,
(without the Rutherford-forward peaking) and create this way a large
file of particles, that emerge from your source point.

  Source 3S AuPPAu.reak 10000 10 0.1 0.1 > pp.dat

Then run Detectors with the DDF, that you want to use, and have the
three-dimensional coordinates of the proton hits, the detector number
and the strip number tabulated:

  Detectors -C 1 -I pp.dat 0x0y0z0d0s > AllDet.debug
```

```
Use the tool Gates (see below) to isolate individual detectors and strips
in small files, for example for all strips of detector 7:

  Gates "4 0 0" < AllDet.debug > Det0.debug

or detector 0-5, strip 3 (in our example a kind of intercepted ring)

  Gates "4 0 5 5 3 3" < AllDet.debug > SripDetS3.debug

Finally use gnuplot (the "splot" command and "set view"
or just plot for one plane) to see the whole setup or the selected
detectors in 3D, where the hits "paint" the active detector surfaces.


4 THE ONE-D GATING TOOL Gates
=============================

Gates reads a file from the standard input (stdin) and checks given columns for ranges
of values. If the value is in the range, the line is echoed to the standard output.

Gates has a single argument, which is a string containing the Column number, (integer)
the lower and the upper limits (real) for the corresponding column in the table read
from stdin, accepting columns 1 through 32, but echoing also longer input lines. If
more than one gate is defined, a line is rejected, if any of the data elements in it
does not pass its gate. Up to six gates can be defined for one pass of gates. A nega-
tive column value indicates a NOT condition (NOT in the interval between Lx and Hx).


  Syntax: Gates "ArgumentString"
          ArgumentString: [-]C1 L1 H1 [[-]C2 L2 H2] ... [[-]C6 L6 H6]

           NOTE: The quotation marks are technically not part of the
                 syntax, but a hint, that q's are needed to pass a string
                 with blanks in it as ONE UNIX parameter. Gates will not
                 accept e.g. three parameters for the number and lower limit
                 and upper limit of a column instead of a string, which would
                 result from e.g. 'Gates 1 3.55 4.76' instead of
                 'Gates "1 3.55 4.76"'

By running multiple passes of Gates, the (still) missing options for "NOT in " or con-
ditions like "in gate1 OR in gate2" can be replaced by either running a file with one
gate and another gate, summing the output by adding the second run to the output of the
first run like

  Gates "some gate" < In.dat > Gated.dat
  Gates "some alternative gate" < In.dat >> Gated.dat
                                       ^this means: Add to file!

5 THE 1D HISTOGRAMMING TOOL Hist
================================

   Syntax: Hist "ArgumentString" FName_Core
           ArgumentString: L0 H0 Channels0 [L2 H2 Channels2] ...
                                                  [L4 H4 Channels4]

           NOTE: The quotation marks are technically not part of the
                 syntax, but a hint, that q's are needed to pass a string
                 with blanks in it as ONE UNIX parameter. Same as in
                 the case of Gates.

Like Gates, Hist is intended to be used as part of a UNIX pipe that processes ASCII-
tables. It behavior is somewhat different so. The input from stdin is directly an un-
filtered copied to stdout. In the same time, up to five histograms for the five first
```

columns of the output are integrated, using for each histogram all data elements in that column, that fall into the limits of the corresponding spectrum, no matter if the other data elements match the other histograms' acceptance windows. After EndOfFile on the stdin is reached, the tables are output to files, whose names are generated in the following way:

```
    NameForHist0 = FName_Core + "0" + ".dat"
                   ^from the command line
```

Each histogram file consists of two columns, the beginning position of a bin (e.g. in energy, if the corresponding data in the input table column was energy), and the number of counts that fell into this bin.

6 THE 1D HISTOGRAMMING TOOL Hist2

```
   Syntax: Hist InputColum From To Channels
```

Like Gates, Hist is intended to be used as part of a UNIX pipe that processes ASCII-tables. Instead of a copy of the input, a Histogram of the desired colum is send to the standard output.

The histogram file consists of two columns, the beginning position of a bin (e.g. in energy, if the corresponding data in the input table column was energy), and the number of counts that fell into this bin.

8.3 The Program GAMMAW

A program in SPEAKEZ to calculate Wigner limits used to generate the graphs shown in this thesis.

```
LISTING OF PROGRAM GAMMAW
 1 PROGRAM GAMMAW
 2 $  get the parameters
 3 REQUEST Z1
 4 REQUEST Z2
 5 REQUEST M1
 6 REQUEST M2
 7 REQUEST RN
 8 $  if the radius is set to 0, estimate it
 9 IF (RN .EQ. 0) THEN
10   REQUEST R0
11   IF (M1 .GT. 1.1) THEN
12     RN = R0 * M1**0.3333
13   ELSE
14     RN = 1.0
15   ENDIF
16   IF (M2 .GT. 1.1) THEN
17     RN = RN + R0 * M2**0.3333
18   ELSE
19     RN = RN + 1.0
20   ENDIF
21   RN
22 ENDIF
23 $
24 REQUEST E1
25 REQUEST E2
26 REQUEST ESTEP
27 REQUEST MAXL
28 $
29 GAMMA=ARRAY(INTPART((E2-E1)/ESTEP+1),MAXL+1:)
30 ENE=ARRAY(INTPART((E2-E1)/ESTEP+1):)
31 HBAR=197.33
32 ESQR=1.44
33 $
34 MU=M1*M2/(M1+M2) * 931.501
35 $
36 FOR L=0,MAXL
37   FOR E=1,INTPART((E2-E1)/ESTEP+1)
38     EMEV = E1+E*ESTEP
39     ENE(E) = EMEV
40     ETA = ESQR*Z1*Z2/ (HBAR*SQRT(2*EMEV/MU))
41     K = SQRT(2*MU*EMEV) / HBAR
42     RHO = K*RN
43     COULOMB(L,ETA,RHO,F,FP,G,GP)
44     P = RHO/(F*F+G*G)
45     GAMMA(E, L+1) = 1000 * 3 * HBAR**2/(RN**2 * MU) * P
46   NEXT E
47 NEXT L
48 $
49 END
```

(Gamma(E,l) in keV, radius in fm, masses entered in unit, energies entered in MeV)

9 References

[1] H. Bethe, Phys. Rev. **55** (1939) 434

[2] C. E. Rolfs, W. S. Rodney, "Cauldrons in the Cosmos", University of Chicago Press ISBN 0.226-72456-5

[3] i.e by the direct observation of atomic lines of unstable elements (Tc) and γ-rays from radio-active decay (^{26}Al).

[4] L.M. Bollinger et al., Nuc. Inst. and Meth. B**79** (1993) 753

[5] E. Burbidge et al. "B^{2}FH", Rev. Mod. Phys. **29** (1957) 547

[6] H. Schatz et al. astro-ph/0102418 23.Feb. 2001

[7] R.C. Wallace, S.E.Woosley, APJ Sup. **45** (1981) 389

[8] H. Schatz et al, Phys. Rep. **294** (1998) 167

[9] P. D. Kunz, Univ. of Colorado, unpublished.

[10] E. Gadioli et al, Z. Phys. A**310** (1983) 42

[11] E. Gadioli et al., J. Phys. G, **7** (1980) 1391

[12] A. Ferrero et al., Z. Phys. A**293** (1979) 123

[13] Funck+Langanke, better one for direct background

[14] H. Oberhummer, Kerne und Sterne, Johann Ambrosius Barth ISBN 3-335-00319-5

[15] J. Gómez del Campo et al, Phys. Rev. Lett. **86** (2001) 43

[16] for example T. Mayer-Kuckuck, Kernphysik, Teubner Studienbücher ISBN 3-519-43021-5

[17] C. Rolfs in H. Oberhummer (Ed.), Graduate Texts in Contemporary Physics, Springer (1991) p. 1-7, ISBN 3-540-54198-5

[18] T. Teichmann and E.P. Wigner Phys. Rev. **87** (1952) 123

[19] Abramowitz and Stegun (N.B.S. Handbook)

[20] J.M. Blatt and L.C. Biedenharn, Rev. Mod. Phys. **24** (1952) 258

[21] L.C. Biedenharn et al., Rev. Mod. Phys. **24** (1952) 249

[22] E.P. Wigner & L. Eisenbud, Phys. Rev. **72** (1947) 29

[23] A.M.Lane & R.G.Thomas , Rev. Mod. Phys. **30** (1958) 257

[24] R.O. Nelson et al., Nucl. Inst. Meth. Phys. Res. A**236** (1985) 128

[25] K.I. Hahn et al., Phys. Rev. C**54**, 1999(1996)

[26] H.L. Ravn, Nucl. Inst. and Meth., B**70** (1992) 107

[27] D. Darquennes *et al.*, Phys. Rev. C**42**, (1990) R804

[28] G. Münzenberg, H. Geissel and C. Schneidenberger, Proceedings of the 13th International Conference on Electromagnetic Isotope Separators and Techniques related to their Applications (EMIS-13), Bad Dürkheim, Germany, 23-27 September 1996, Nucl. Inst. and Meth B**126** (1997), and references therein

[29] R.C. Haight et al., Nucl. Inst. and Meth., **212** (1983) 245

[30] T. Yamaya et al., Nucl. Inst. and Meth., B**70** (1992) 374

[31] A.Ozawa et al., RIKEN-AF-NP-236, unpublished.

[32] J.J. Kolata et al., Phys. Rev. Lett. **81** (1998) 4580

[33] J.K.Bair, Phys. Rev. C**8**, (1973) 120.

[34] J.D.Anderson et al., Phys. Rev **177**, (1969) 1416

[35] W. Gruhle, Nucl. Phys A**186** (1972) 257

[36] S.T. Thronton, Nucl. Phys. A**137** (1969) 531

[37] C.J. Oliver et al., Nucl. Phys. A**127** (1969) 567

[38] J.F. Ziegler, J.P. Biersack "The stopping Power of Ions in Solids", Pergamon Press, New York, 1985 (ISBN 0-08 021603)

[39] R.C. Pardo and K.W. Shepard, unpublished

[40] W. Kutschera, et al., ANL Physics Division Annual Review, (1993) p.55

[41] John P. Greene (ANL) developed this technique.

[42] B. Harss et. al., Proceedings of the XVIII International Linear Accelerator Conference, Geneva, Swizerland, CERN 96-07 **2** (Nov. 15 1996) 496

[43] B. Harss et al., Phys. Rev. Lett. **82**, (1999) 3964

[44] K.E. Rehm et al, Phys. Rev. Lett. **81** (1998) 3341

[45] B.A. Brown and P.G. Hansen, Phys. Lett. B**381** (1996) 391

[46] B.A. Brown et al., Nucl. Phys. A**277** (1977) 77

[47] D.J. Hinde and M. Dasgupta, in Proceedings of the Tours Symposium on Nuclear Physics, Tours, France, 1997 (AIP Publishing New York)

[48] C.R. Morton et al., Phys. Rev. C**52** (1995) 243

[49] Ludwig (**L**arge **U**niversal **D**etector **W**ith **I**mmense **G**ranularity) was chosen as a name for the silicon detector setup, since one member of the collaboration (ER) had a strong urge to honor the famous king of his remote homelands. Ludwig II refers to the fact that a setup with one annular Si-Detector had existed at ANL previously or, depending, on whom you ask, that there are two identical annular Si-detectors, internally called to as LI and LII.

[50] B. Harss et al., ANL Physics Division Annual Review, (1997) p.12

[51] Ch. Schießl et al., Nucl. Inst. and Meth. **192** (1982) 291

[52] L.Meyer, Phys. Stat. Sol. **44** (1971) 253

[53] H. Schmidt-Boecking, Lecture Notes in Physics **83** (1978)

[54] Feldman & Cousins Phys. Rev. D**57** (1998) 3873

[55] R.A. Blue and W. Haeberli, Phys. Rev. **137** (1965) B284

[56] D.R. Tilley et al., Nucl. Phys. A**595** (1995) 1

[57] D.W. Bardayan et al., Phys. Rev. Lett. **83** (1999) 45
D.W. Bardayan et al., Phys. Rev. C**62** (2000) 055804

[58] H.T. Fortune and R. Sherr Phys. Rev. Lett. 84 (2000) 1635

[59] J.A. Weinmann and E. Silverstein, Phys. Rev. **111** (1958) 277